Universidad de Alcalá

PhD. Program in Electronics: Advanced Electronic Systems. Intelligent Systems

Inertial Pocket Navigation System for Pedestrians

PhD. Thesis Presented by

Estefanía Muñoz Díaz

2016

Universidad de Alcalá

PhD. Program in Electronics: Advanced Electronic Systems. Intelligent Systems

Inertial Pocket Navigation System for Pedestrians

PhD. Thesis Presented by

Estefanía Muñoz Díaz

Advisor

Dr. Juan Jesús García Domínguez

Alcalá de Henares, 2016

VERSION JANUARY 2018

A Lucía

. . . everything else gets reduced to essentials.

Acknowledgements

A todos los que la presente vieren y entendieren.

Inicio de las Leyes Orgánicas. Juan Carlos I

I would like to thank my advisor Dr. Juan Jesús García Domínguez for his trust and great encouragement.

This doctoral thesis has been carried out at the Institute of Communications and Navigation of the German Aerospace Center (DLR) in Munich. I am grateful to the colleagues that invested time discussing technical issues related to my thesis, particularly my colleagues of the Vehicular Applications group. Thanks to my master thesis students for constantly challenging me.

I specially thank Prof. Dr. Uwe-Carsten Fiebig for his support throughout this thesis and his helpful corrections.

Last but not least, I would like to thank Fabian for the endless technical discussions and constant motivation in both professional and private life. Without you this thesis would not have been possible.

Resumen

Hoy en día existe una gran demanda de sistemas de navegación personales integrados en servicios como gestión de desastres para personal de rescate. También se demandan sistemas de navegación personales como guía en grandes superficies, por ejemplo, hospitales, aeropuertos o centros comerciales. En esta tesis doctoral los escenarios bajo estudio son interiores y urbanos. La navegación se realiza por medio de sensores inerciales y magnéticos, idóneos por su amplia difusión, tamaño y peso reducido y porque no necesitan infraestructura. Se llevarán a cabo investigaciones para mejorar los algoritmos de navegación ya existentes y cubrir determinados aspectos aún no resueltos.

En primer lugar se ha llevado a cabo un extenso análisis sobre los beneficios de usar medidas magnéticas para compensar los errores sistemáticos de los sensores inerciales, así como su efecto en la estimación de la orientación. Para ello se han usado medidas de referencia con valores de error conocidos combinando diferentes distribuciones de campos magnéticos. Los resultados obtenidos quedan respaldados con medidas realizadas con sensores reales de medio coste. Se ha concluido que el uso de medidas magnéticas es beneficioso porque acota errores en la orientación. Sin embargo, los escenarios bajo estudio suelen presentar campos magnéticos perturbados, lo que provoca que el proceso de estimación de errores sea prohibitivamente largo.

En esta tesis doctoral se proponen algoritmos alternativos para el cálculo del desplazamiento horizontal del usuario, que han sido comparados con respecto a los ya existentes, ofreciendo los propuestos un mejor rendimiento. Además se incluye un innovador algoritmo para calcular el desplazamiento vertical del usuario, haciendo por primera vez posible obtener trayectorias en 3D usando solamente sensores inerciales no colocados en el zapato.

Por último se propone un novedoso algoritmo capaz de prevenir errores de posición provocados por errores de rumbo. El algoritmo está basado en puntos de referencia automáticamente detectados por medio de medidas inerciales. Los puntos de referencia elegidos para los escenarios cubiertos son escaleras y esquinas, que al revisitarse permiten calcular el error acumulado en la trayectoria. Este error es compensado consiguiendo así reducir el error de rumbo. Este algoritmo ha sido extensamente probado con medidas de referencia y medidas realizadas con sensores reales de medio coste. La compensación de este error se adapta a las características del sistema de navegación personal.

Abstract

There is nowadays a high demand of pedestrian navigation systems, which are integrated in safety-of-life services such as disaster management for rescue personnel or location-based services such as guidance in hospitals, airports or shopping malls. In this thesis, indoor and urban environments constitute the targeted scenarios and the navigation is performed with inertial and magnetic sensors due to their wide availability, light-weight and infrastructure-less nature. The research of this thesis aims at improving or covering specific gaps of pedestrian navigation areas to offer versatile pedestrian navigation systems for a wide range of applications.

First, the use of magnetic field measurements to compensate the error of the gyroscopes and their effect on the estimated orientation has been comprehensibly analyzed. Quasi-error-free measurements with known bias values have been used combined with different magnetic field distributions and the results have been endorsed with medium-cost sensors' measurements. It is concluded that the use of magnetic measurements is beneficial to estimate the bias of the gyroscopes, yielding to reduced orientation estimation errors. However, the targeted scenarios commonly present perturbed magnetic fields and the biases' estimation process becomes prohibitively slow.

Second, several algorithms have been proposed in this thesis that outperform the accuracy of the horizontal displacement estimation with respect to the state of the art. Additionally, an innovative vertical displacement estimation algorithm has been proposed and tested in real-world scenarios. This algorithm makes it possible for the first time to solve unaided 3D inertial navigation for non-shoe-mounted sensors.

Lastly, a novel drift estimation algorithm capable of preventing positioning errors caused by orientation errors is proposed. The computation of the drift error is based on landmarks seamlessly detected using solely inertial measurements. Landmarks defining the building or city layout have been chosen to be stairs and corners. By re-visiting these landmarks it is possible to compute the accumulated drift error, which is used to reduce the orientation error. The proposed algorithm has been extensively tested with quasi-error-free and medium-cost sensors' measurements. Two types of corrections, online and post-processed, are presented to adapt the pedestrian navigation system to the particular application.

Contents

List of Figures

List of Tables

List of Acronyms

DLR	German Aerospace Center.
FOG	fiber optic gyroscope.
GPS	Global Positioning System.
HRV	heart rate variability.
IAEA	International Atomic Energy Agency.
MEMS	micro-electromechanical sensors.
PDR	pedestrian dead-reckoning.
SLAM	Simultaneous Localization And Mapping.
UWB	ultra-wideband.
WLAN	wireless local area network.
ZUPT	zero-velocity update.

List of Symbols

$\boldsymbol{x}_{\mathrm{o}}$	State vector of the orientation filter
$\boldsymbol{x}_{\mathrm{p}}$	State vector of the position filter
t	Time
ϕ	Roll angle
θ	Pitch angle
ψ	Yaw angle
x	Position in the x-axis
y	Position in the y-axis
z	Position in the z-axis
$\boldsymbol{\alpha}$	Acceleration measurement vector
$\boldsymbol{\omega}$	Turn rate measurement vector
$\boldsymbol{\mu}$	Magnetic field measurement vector
s	Step length
ζ	Scaling parameter of the step length models
γ	Length of the leg of the pedestrian
v_{p}	Vertical displacement of the pelvis
α_{z}	Vertical acceleration
$\boldsymbol{b}$	Bias vector of the gyroscopes
$\boldsymbol{C}$	Direct cosine matrix
$\boldsymbol{A}$	Change in orientation during a time stamp
$\boldsymbol{I}$	Identity matrix
Δt	Elapsed time
$\boldsymbol{e}$	Error vector of the turn rate measurement
ν	White noise

τ	Correlation coefficient of the biases model
n	Noise coefficient of the biases model
β	Bias stability
f_{s}	Sampling frequency
g	Gravity acceleration
$\boldsymbol{H}$	Magnetic field vector
d	Declination angle
ω_{e}	Rotation of the Earth
λ	Latitude
Ψ	Scalar potential magnetic field
ξ	Scaling parameter of the magnetometer calibration
l	Translation parameter of the magnetometer calibration
$\boldsymbol{M}$	Rotation matrix of the magnetometer calibration
$\Delta\theta$	Pitch amplitude
a	Calibration parameter of the proposed step length model
b	Calibration parameter of the proposed step length model
f	Step frequency
v	Vertical displacement
ψ_B	Yaw angle measured before the corner
ψ_A	Yaw angle measured after the corner
q	Window length of the yaw buffer used for landmark detection
m	Window length of the separation between both yaw buffers
Δ^2	Squared Mahalanobis distance
$\boldsymbol{P}$	Uncertainty matrix of the position
δ	Deviation angle
ϵ	Drift
ϵ_{o}	Offline drift
η	Number of associations

General Notation Rules

Throughout the thesis, the following notation will be used:

- Vectors are represented in bold.
- Matrices are represented in capital letter.
- k is a superindex reserved for time stamp.
- j is a superindex accounting for number of steps.
- $(\cdot)^T$ and $(\cdot)^{-1}$ stand for matrix (or vector) transpose and inverse, respectively.
- $\hat{x}$ is an estimation of the parameter x.
- $\bar{x}$ is the measurement or pseudo-measurement of the parameter x.
- $x^{\mathrm{a}}_{\mathrm{b,c}}$ is the measurement x in the c frame with respect to the b frame expressed in a frame coordinates.
- i, e, n and b as indexes stand for inertial, Earth, local navigation and body frame, respectively.
- $\tilde{x}$ is the quasi-error-free measurement corresponding to the measurement x.
- H, U and D as subindexes stand for horizontal, upstairs and downstairs, respectively.
- $\|\boldsymbol{x}\|$ is the norm of vector $\boldsymbol{x}$.

Chapter 1

Introduction

If you can't explain it to a six year old,
you don't understand it yourself.

Albert Einstein

The term navigation stems from Latin and means "to sail, go by sea, steer a ship". In 1492 the Spanish monarchs funded Christopher Columbus's expedition to sail west to reach the Indies by crossing the Atlantic, which resulted in the discovery of America. The first circumnavigation of the Earth was completed with the Magellan-Elcano expedition. The fleet of seven galleons sailed from Sanlúcar de Barrameda in Southern Spain in 1519, crossed the Atlantic Ocean, continued across the Pacific, the Indian Ocean and along the coast of Africa. Only the galleon Victoria finally arrived in Spain in 1522, three years after the expedition's departure.

The navigation methods these explorers used have evolved throughout history and many new methods arose. One of the most important decisions involves choosing the best methods to use. Each method has advantages and disadvantages, whilst none is effective in all situations [1]. The methods of navigation can be divided into two: dead-reckoning and piloting.

Dead-reckoning is the process of determining one's current position projecting course and speed or elapsed distance from a known previous position. The course can be determined with a magnetic compass, which consists of a magnetized needle that rotates freely in a horizontal plane. The speed or the elapsed distance can be determined, among others, with the acceleration due to one's proper movement and the elapsed time. The accelerometer is a sensor that, attached to a body, measures the specific force acting on one's body either due to natural forces like the gravity or due to one's proper movement. On the one hand, the dead-reckoning method tends to accumulate errors that over time may be so significant that the determined position is no longer accurate enough. On the other hand, dead-reckoning constitutes a self-contained navigation method which does not rely on external objects.

Piloting is the process of determining one's position based on external objects. One position determination with this method is usually called a fix. There is a wide range of piloting navigation methods, being celestial navigation one of the ancients. The angle between a celestial object and the horizon can be used to determine one's position. If the chosen object is situated on the Earth, it is called a landmark, which can either be natural or manmade, e.g. Table Mountain near Cape Town or the Colossus of Rhodes. The position of the landmark is used to determine one's position. The chosen object can also emit any type of signal, e.g. acoustic or light signal, like a lighthouse. Electromagnetic signals are used by constellations of satellites, like the Global Positioning System (GPS), or devices located on the Earth, such as base stations or wireless local area network (WLAN) access points. Both, satellite and radio navigation, use electromagnetic signals to deduce one's position.

In practice, a navigation system should synthesize different methodologies into a single integrated system and never rely completely only on one method when others are also available. These methods must be chosen depending on each situation [1]. Dead-reckoning should be used either when no position fix is possible or to bridge the intervals between successful position fixes.

1.1 Pedestrian Navigation

There is nowadays a high demand of pedestrian navigation systems which are expected to work in challenging scenarios with a reasonable accuracy. Many of them are integrated in safety-of-life services such as disaster management for rescue personnel. In a daily basis, many firefighters are in trouble because they get disoriented in forest fires or large buildings on fire, among others. This situation makes it difficult to find the way out within a safe time frame resulting in serious consequences.

Pedestrian navigation systems, however, are not only restricted to the professional market. Their demand is widespread for all kind of location-based services such as guidance in airports, hospitals or shopping malls. Such navigation systems have particular requirements, since they are designed for daily use of every citizen: the operating instructions should be simple; the navigation system should be small-sized and light-weighted to carry it on comfortably; it should be inexpensive. A classical solution is to integrate the pedestrian navigation system in the smart phone taking the advantages of the multiple sensors embedded, such as satellite navigation receiver, inertial sensors, WLAN module, magnetometer, barometer and the proper communication module.

For this thesis, it has been decided to design a pedestrian navigation system that can be integrated in safety of life services and also be used for mass market applications, including auxiliary services like guidance for visually impaired people or medical applications. Depending on the purpose of the pedestrian navigation system, the sensors used will have

different quality, which has a direct impact on price and accuracy. For this thesis, it has been decided to use medium-cost sensors. The navigation system is designed, but not restricted, for the sensors to be located on the upper part of the leg. This is a common location for a smart phone placed in the front pocket of the trousers. Alternatively, the sensor can easily be embedded in the inner pants of the firefighters, protected from the high temperatures.

The targeted scenarios have been chosen given the fact that humans spend more than 90% of their time indoors [2]. The choice of suitable navigation methods is tightly coupled with the targeted scenarios. The main disadvantage of satellite navigation lies on the fact that in many environments the constructions or vegetation block satellite signals, as it is the case in urban canyons, forests or indoors. Radio navigation could be divided in opportunistic and dedicated. Dedicated methods are based on devices that must be previously installed in the operating area and allow the positioning via trilateration, e.g. Bluetooth beacons or ultra-wideband (UWB). Opportunistic methods make use of devices which are already installed, such as WLAN access points or mobile phone base stations. However, the emitted signal is not optimal because these devices have been usually designed for communication applications. In general, radio-based navigation including satellite navigation suffers from multipath propagation and signal blockage. Therefore, additional navigation methods should be used to overcome the intervals where a position fix might not be possible, e.g. underground or indoors.

Inertial sensors are composed of accelerometers and gyroscopes, which measure specific force and turn rate, respectively. The so-called inertial measurement unit contains three mutually orthogonal accelerometers and three mutually orthogonal gyroscopes. Therefore, the acceleration and turn rate measurements are triads. The dead-reckoning method based on inertial sensors has experienced a great growth over the last years. The microelectromechanical sensors (MEMS) are widely used due to their miniaturization and prize reduction. To derive the speed or the elapsed distance, only the acceleration due to the pedestrian movement has to be used. Therefore, it is necessary to subtract the acceleration due to gravity, which is done by knowing the orientation of the sensor. The change in orientation is measurable with gyroscopes.

Magnetometers, which are commonly embedded together with the inertial sensors, measure magnetic fields, e.g. the Earth's magnetic field. Usually, a magnetometer unit is formed by three mutually orthogonal magnetometers. Magnetometers have been used for centuries to determine the magnetic North. For the targeted scenarios, the Earth magnetic field is usually perturbed due to the proximity of ferromagnetic materials and electric currents. Nevertheless, even if the Earth magnetic field is perturbed, it can be used to enhance the orientation estimation.

Although many publications have been written about pedestrian inertial navigation systems, some issues are not yet solved. The accuracy of the estimated orientation is of

key importance to the positioning. With a poor gravity subtraction, the positioning error grows prohibitively. Even with medium-cost gyroscopes, the foot dynamics allow regular speed corrections that make it possible to obtain an acceptable 3D positioning using only MEMS inertial sensors. Therefore, a great part of the literature has been written for shoe-mounted pedestrian navigation systems. The complex dynamics of the upper part of the leg do not allow applying such corrections. The current algorithms for non-shoe-mounted inertial navigation systems lack accuracy on the horizontal displacement compared to the shoe-mounted systems and do not solve the displacement on the vertical direction.

The use of perturbed magnetic field measurements on the estimated orientation and particularly on the gyroscope systematic errors has not been properly addressed so far. As well as the accumulated orientation error over time, commonly called drift. The drift should be computed and used by the navigation system to prevent future positioning errors. The vast majority of algorithms of the literature do not compute the drift, but only perform positioning corrections when satellite or radio fixes are available. The lack of drift correction leads to large positioning errors when only dead-reckoning is applied.

1.2 Goal and Contributions of the Thesis

The goal of this thesis is to contribute to the research field of pedestrian inertial navigation, particularly for indoor and urban scenarios. Herein, it is assumed that the sensor is attached to the upper part of the leg of the pedestrian, since a smart phone or motion sensor can be easily carried in the front pocket of the trousers. On the one hand, state of the art algorithms for non-shoe-mounted navigation systems show poor accuracy in the horizontal displacement, and the vertical displacement is unsolved without using additional sensors. On the other hand, the yaw angle rapidly accumulates an error mainly caused by systematic errors of the gyroscope.

With these limitations in mind, this thesis addresses the following topics:

- Comprehensive analysis of the effect of different magnetic field distributions on the bias of the gyroscopes.
- Investigation of an algorithm to improve the accuracy of the horizontal displacement estimation.
- Investigation of an algorithm to estimate the vertical displacement of the pedestrian.
- Research alternative methods to compensate the remaining error on the yaw angle.

These four topics are waived together constituting a pedestrian navigation system, as shown in Figure 1.1. Each algorithm, i.e. orientation, displacement, drift and position estimator, is proposed and compared to the state of the art. Although some algorithms are fed with variables generated in the navigation system, each algorithm is self-contained

and can be used independently. Among the algorithms that form the pocket navigation system, only the displacement estimator is specific for the pocket location. The remaining algorithms are valid for other sensor locations.

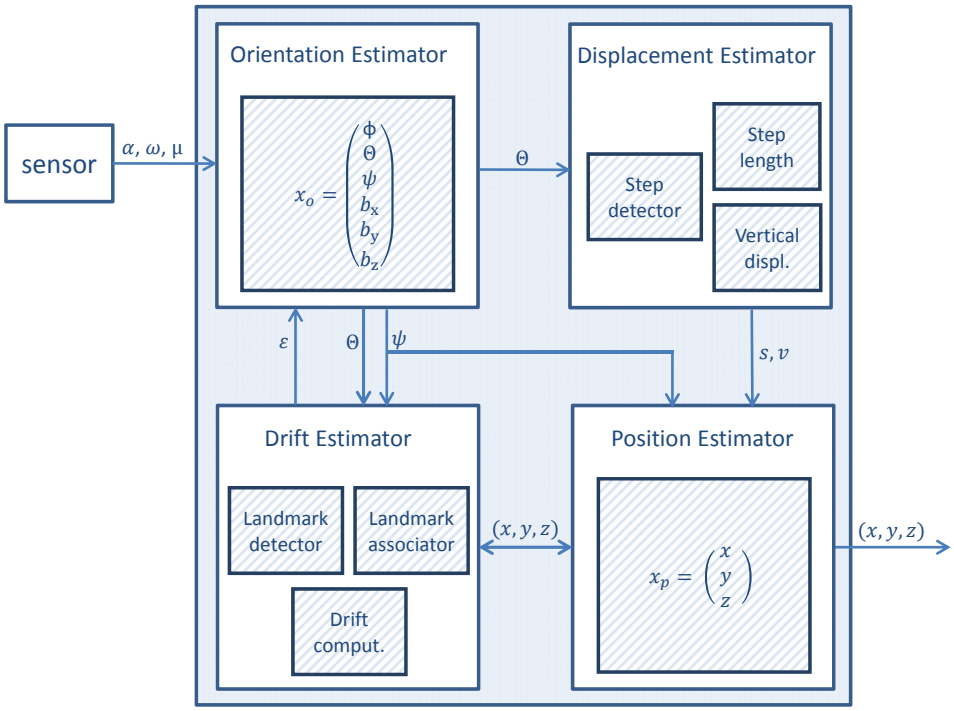

Figure 1.1: System overview of the pedestrian inertial navigation system presented in this thesis.

The orientation estimator is an algorithm that takes acceleration, turn rate and magnetic measurements from the sensor, as indicated in Figure 1.1. It consists of an unscented Kalman filter whose states are the three Euler angles describing the sensor orientation and the systematic errors of the three orthogonal gyroscopes, the biases. This thesis describes the filter in detail and then tests it with real measurements corresponding to very long walks of 39 min and 44 min duration. If magnetic measurements are not used, the yaw error grows rapidly. By using magnetic measurements, the bias of the z-axis gyroscope can be estimated and the yaw error growth is limited. To this end, the effect of different magnetic field distributions on the orientation and also on the biases of the gyroscope is analyzed in depth. For homogeneous magnetic fields at different locations on the Earth, it can be concluded that even for the less favorable location, the bias of the z-axis gyroscope can be estimated thanks to the movement of the leg while walking, but it requires more time to converge. This is also the case of the non-homogeneous magnetic fields, in which the poor estimation of the bias of the z-axis gyroscope leads to a great accumulated error on the yaw. Therefore, further solutions must be investigated to reduce this error, which is commonly called drift.

The displacement estimator is composed by three algorithms that provide the horizontal and vertical displacement of the pedestrian stepwise. These algorithms are the step detector, the step length estimator and the vertical displacement estimator. The pro-

posed step detector makes use of the orientation of the sensor provided by the orientation estimator. The performance of the detector is compared to the state of the art and it is found that it leads to less undetected steps and less false detections. Moreover, the proposed detector is able to work in 3D scenarios, where the state of the art algorithms face problems, i.e. on stairs. Unlike the state of the art step length estimators that make use mainly of raw acceleration measurements, the proposed algorithm makes use of the orientation of the sensor. The experiments compare the performance of the proposed algorithm with the literature under different situations, i.e. walking slowly in a museum, walking at a normal speed and walking fast. The proposed algorithm outperforms the currently used algorithms in the literature, because its optimal working zone is extended to different walking speeds. As previously mentioned, inertial pedestrian navigation for non-shoe-mounted sensor locations does not consider 3D scenarios. This thesis proposes a novel vertical displacement estimator that only uses the orientation of the sensor. The experiments in real-world environments highlight that the pedestrian can be located with a vertical accuracy of 1% of the covered height given that all steps are detected.

Since the yaw error is not completely compensated using magnetic measurements, landmarks are used in this thesis to compute the accumulated drift. The chosen landmarks are adapted to indoor and urban environments and are automatically detected by using solely orientation measurements. The drift error is then fed back to the orientation estimator for correcting the yaw angle and preventing further positioning errors. The experiments show that landmarks are seamless detected, since the pedestrian only needs to keep walking. This process is repeated during the walk so that slow changes of the drift can be tracked.

The position estimator consists of an unscented Kalman filter that computes the new pedestrian 3D position stepwise based on the yaw angle and the horizontal and vertical displacement measurements. If there is no position fix, the uncertainty on the position only grows with time. When a fix occurs, the filter performs a position update reducing its uncertainty. Depending on the application of the navigation system, the corrections derived from landmark associations can be applied online or offline. Both types of corrections are explained and evaluated in the experimental section.

1.3 Real-World Applications

The personal navigation system derived from the research carried out in this thesis has been successfully used for several applications with different requirements.

In the health area, the proposed navigation system has been used as enhancement of an allergy detection system based on the heart rate variability (HRV). The oral food challenge consists on allergy provocation tests where the patient has to take a little portion of food and wait a certain period of time for a possible allergic reaction. This procedure

is repeated over time, so that the complete test may last up to 4 h. Nowadays, these tests are performed in the hospital under the direct supervision of the medical stuff to visually identify the allergic reaction. Recently, an automatic allergy detection system based on HRV has been proposed [3]. Despite the many advantages of this system, HRV changes might also be caused by the physical activity of the patient. By enhancing the HRV-based allergy detection system with the pocket navigation system, it is possible to discard false allergic reaction alarms that have been caused by the physical activity of the patient rather than by a real allergic reaction. The pocket navigation system is able to identify walking from standing, sitting, walking upstairs and walking downstairs. Since the direct visual contact with the medical stuff is not necessary with the HRV-based allergy detection system, the comfort of the patient during the tests is improved by allowing the patient moving within the hospital. Additionally, thanks to the pocket navigation system, the patient can be located if a severe allergic reaction occurs [4].

In the safety-of-life area, the proposed pocket navigation system is being integrated with an inertial shoe-mounted navigation system in a personal light-weighted navigator designed for rescue personnel. In a daily basis, despite their professional training, many firefighters face problems because they get disoriented in forest fires or large buildings on fire, among others. The key requirement for this application is to provide an accurate current position. Additionally, for this application the complete generated trajectory plays an important role, because it helps identifying the explored and unexplored areas and can be of great help to find the way out by following back the trajectory to the initial position. Therefore, the pocket- and the shoe-mounted modules are fused in order to provide an enhanced trajectory with less accumulated drift over a longer period of time, compared to using only one module. The targeted scenarios favour the use of dead-reckoning navigators, since the positioning computed out of satellite pseudoranges or WLAN/UWB ranges among others, has to be bridged over long periods of time. Additionally, the pocket-mounted module allows solving the position not only walking, but also crawling, which is common for firefighters due to the smoke.

Another professional application is the case of the inspections of nuclear facilities, for the International Atomic Energy Agency (IAEA). The targeted scenarios for this application are nuclear power plants or nuclear waste repositories, i.e. indoors or underground. Thus, the use of inertial sensors, which are infrastructure less and light-weighted, is recommendable. The navigation system should be seamless to the user, in order for the inspector to pay attention to the visit. The sensors are mounted on the inspector in order to record inertial data during the visit. After the visit to the nuclear facility, the inspector elaborates a report for the IAEA. In this stage, the recorded inertial data is processed to generate the inspector's trajectory. The key requirement for this application is to provide the trajectory of the inspector that allows recognizing the visited areas and identify the non-visited areas of the nuclear facility. Attention should be paid on visiting all areas in order to verify the nuclear activities carried out there. The drift estimation

module proposed in this thesis has been used in combination of an existing shoe-mounted inertial navigation system in order to reduce the drift of the computed trajectory in a post-processing stage. Landmarks describing the layout of the nuclear facilities, such as corners, stairs, ramps and ladders, are automatically detected. Potential associations are proposed to the inspector to compensate the drift accumulated in the computed trajectory of the visit in a post-processing stage.

1.4 Background of the Thesis

This doctoral thesis has been carried out at the Institute of Communications and Navigation of the German Aerospace Center (DLR) in Munich. The research was funded by a DLR-DAAD Research Fellowship.

1.5 Structure of the Thesis

This thesis is divided into seven chapters. Chapter 2 reviews the state of the art regarding orientation estimation, step detection, step length and vertical displacement estimation and drift compensation algorithms.

Further on, the four blocks that comprise the pedestrian inertial navigation system are detailed in the following chapters. The orientation estimation filter and the corresponding experimental results are presented in Chapter 3. Chapter 4 explains the proposed step detector and the physical activities identification. Models for the step length and vertical displacement estimation are described in this chapter and finally all algorithms are validated with real measurements and compared against the state of the art algorithms. Chapter 5 discuses the drift estimation algorithm, the proposed landmarks as well as their detection, association and the subsequent drift computation. The theoretical approach is supported by experimental results. The position estimation filter and the feedback to the orientation estimation filter are described in Chapter 6. Both, online and offline corrections of the computed drift are evaluated with experimental results.

Finally, the conclusions of this thesis are drawn in Chapter 7 along with their impact on the state of the art. Additionally, an outlook with further investigation lines and a list of the publications derived from the research carried out in this thesis, are provided.

Chapter 2

State of the Art

Y así, del mucho leer y del poco dormir, se le secó el cerebro de manera que vino a perder el juicio.

Miguel de Cervantes, Don Quijote de la Mancha

Pedestrian navigation systems based on inertial sensors use pedestrian dead-reckoning (PDR) to sequentially deduce the user position. There are two types of PDR, the strapdown algorithm and the step-and-heading approach.

The computation of the position using the strapdown algorithm consists of the double integration over time of the measured acceleration. The accelerometer, however, is a sensor that measures the specific force. The measured specific force is the sum of the proper movement of the pedestrian and other accelerations such as the gravity, the centripetal force, the Euler force and the Coriolis force. The last three forces are disregarded for PDR, since the pedestrian does not significantly change its latitude and longitude within a time stamp. The gravity, however, should be cancelled before the strapdown mechanization is done in order to integrate only the acceleration due to the movement of the pedestrian.

Gyroscopes are sensors that measure turn rates, which are used to compute the orientation of the sensor. Knowing the orientation of the sensor it is possible to properly subtract the gravity acceleration, which has a known magnitude and orientation. Inaccuracies on the orientation estimation cause the gravity not being correctly cancelled. As a consequence, the accumulated error in the position of the pedestrian grows.

Therefore, the strapdown algorithm is so far only feasible for medium-cost MEMS in combination with corrections such as the zero-velocity update (ZUPT), that is able to significantly reduce the positioning error. Depending on the sensor location on the pedestrian body, different corrections can be applied. The ZUPT is only feasible for shoe-mounted sensors due to the foot dynamics while walking.

This thesis is based on the step-and-heading approach, which estimates sequentially the position of the pedestrian based on the previous position for each detected step, the

step length and the yaw angle of the pedestrian:

$$\begin{aligned} x^k &= x^{k-1} + s^k \cdot \cos(\psi^k), \\ y^k &= y^{k-1} + s^k \cdot \sin(\psi^k), \end{aligned} \tag{2.1}$$

where x and y represent the position in the x- and y-axis, s stands for the step length and ψ is the yaw angle of the pedestrian. The sequence of individual positions computed stepwise form the travelled trajectory. The algorithms derived from the research carried out in this thesis require the sensors to be located on the upper part of the leg of the pedestrian. The dynamics of the human body at this location do not allow performing ZUPT corrections, therefore the step-and-heading approach is more appropriate.

The step-and-heading approach, as Equation (2.1) reveals, consists of the estimation of the yaw angle and the estimation of the step length. The orientation can be defined by the Euler angles roll (ϕ), pitch (θ) and yaw (ψ). Even if Equation (2.1) only requires the yaw angle, the three orientation angles are of interest. Among others, the pitch angle can be used for the step length estimation algorithm as proposed in this thesis, although the literature algorithms commonly use acceleration or turn rate measurements to this end. There is a large amount of work in the literature in the area of PDR. In [5], a classification of different types of PDR and a comparative study between algorithms proposed in the state of the art can be found.

2.1 Orientation Estimation

One of the critical tasks in inertial pedestrian navigation is the estimation of the orientation of the inertial sensor. The orientation of the pedestrian and the orientation of the sensor are tightly coupled if the sensor is attached to the body of the pedestrian. There are different approaches in the literature to estimate the sensor orientation. These can be classified in deterministic and probabilistic approaches.

A deterministic approach, like Madgwick [6] and Mahony [7] suggest, assumes certainty in all aspects. However, it is appropriate to take into account the uncertainty in the initial conditions, the imperfect observations and the errors in the system models. In a probabilistic or stochastic approach, this uncertainty is taken into account. The great majority of research groups follow a probabilistic approach to estimate the sensor orientation [8–11].

Along with the orientation angles, it is convenient to estimate also the biases of the gyroscope [12, 13]. Biases are systematic errors that should be subtracted from the raw turn rate measurements. The biases for MEMS gyroscopes affect severely the orientation estimation if they are not compensated before integration over time of the turn rate measurements. The estimation of the orientation, specially the yaw angle, for inertial pedestrian navigation has been widely described and analyzed in the literature. How-

ever, the performance of the estimation of the gyroscope biases has not specifically been analyzed so far.

Acceleration and turn rate measurements are usually utilized to estimate the orientation. Other sensors such as magnetometers, which are commonly integrated together with the inertial sensors, allow enhancing the orientation estimation. Magnetometers measure magnetic fields, e.g. the Earth magnetic field, which can be modelled as a dipole. At any location, it can be represented by a three-dimensional vector. For centuries, the Earth magnetic field has been used for determining the direction of the magnetic North. The angle between the magnetic and the true North is called declination. Facing the magnetic North, the angle the field makes with the horizon is called inclination.

The values of intensity, inclination and declination change with time for the same location and are different for different locations on the Earth. As the direction and magnitude of the field are known, it is possible to partially determine the orientation of the sensor by measuring only the Earth magnetic field. The angle representing the rotation around the axis parallel to the magnetic field is not determined.

The magnetometer has historically been discarded for indoor navigation applications, since the Earth magnetic field is usually perturbed due to the proximity of ferromagnetic materials and electric currents. Therefore, it is difficult to find the magnetic North in indoor environments. However, an alternative way to extract valuable information for the orientation estimation in a magnetically perturbed environment has recently been proposed. This procedure makes use of the fact that the aforementioned distortion is highly modulated in space, but relatively constant in time [14].

During a walk under a magnetically perturbed environment, there are periods of constant or quasi-constant magnetic field. Although magnetic measurements corresponding to these periods are perturbed, they are all equally perturbed, thus the change in orientation of the magnetic vector is only due to the change of orientation of the pedestrian. This idea was proposed in [11] for a sensor held in the hand. A basic analysis of its performance can be found in [15]. In the cited article, the gyroscope biases estimation is analyzed with real measurements. However, the bias values are not known, therefore it is difficult to assess if the estimation converges to the correct value. The article concludes with the clear statement that the updates do not significantly decrease the estimated gyroscope error state variance. These updates are only helpful if low-cost gyroscopes and magnetometers are used.

A similar idea based on the same concept was also proposed in [9] for a shoe-mounted sensor. The analysis of its performance for the yaw angle is evaluated using synthetic signals. The experiment reveals that processing the synthetic signals with an unscented Kalman filter, the update decreases the error in the yaw angle after 100 s. However, neither the estimation of the biases of the gyroscope, nor the magnetometer calibration in order to correctly apply the update are covered. Additionally, the article claims that the

update can only be applied during the stance phase of the foot. It has been demonstrated, that the update requires a constant or quasi-constant magnetic field [11], which is possible in wider periods rather than only during the stance phases of the foot.

In this thesis, the usability of the magnetic field in the process of estimating the gyroscope biases for medium-cost MEMS sensors will be addressed (published in [16]). A variety of synthetic magnetic field measurements has been generated for this analysis. This allows replicating the conditions of the experiment and only changing the magnetic field to study its influence of the biases estimation process. Homogeneous and perturbed magnetic fields were simulated and also different locations on the Earth are included in the experiments. The influence of the calibration of the magnetometer prior to apply any magnetic correction is evaluated and an experiment recorded with medium-cost magnetic and inertial sensors is also analyzed. Lastly, the effect of the z-axis bias on the yaw angle is studied.

2.2 Step Detection

Particularly for the step-and-heading approach, a well-known algorithm to detect steps is to identify changes in the vertical displacement of the pelvis. This approach has been developed in [17] with the sensor attached to the belt. For other locations where the sensor is not close to the center of mass of the pedestrian like the upper part of the leg, or for locations which are decoupled from the pedestrian motion such as the hand or wrist, detecting changes in the vertical displacement of the pelvis does not offer optimal results.

Another step detector algorithm in the literature uses acceleration measurements. The simplest approach is finding peaks in the variance of acceleration in the z-axis of the navigation frame [18]. The peaks correspond to the step occurrences because they are generated by the vertical impact when the foot hits the floor. This approach requires pre- and postprocessing of the acceleration measurements and a threshold to avoid spurious detections from low amplitude peaks. A similar approach identifies peaks in the magnitude of the three-axis acceleration [19–22]. The detection of these peaks requires also the use of thresholds to avoid spurious detections. A common disadvantage of the approaches based on the acceleration is that the pattern of the acceleration measurements is greatly affected by the pedestrian walking speed. Therefore, the determination of the variable thresholds for reliable step detection is challenging.

In [23], a step detector based on the pitch angle of a sensor mounted on the waist is presented. The Fourier analysis of the fundamental frequency of the pitch is proposed to detect the pedestrian steps. In [24], a classification of different smart phone motion modes between symmetrical and asymmetrical is proposed. For the symmetrical modes such as texting and phoning, the step detector uses acceleration measurements. For the asymmetrical modes, such as swinging and front and back pocket of the trousers, the use

of the pitch angle is recommended. The zero-crossing of the pitch angle is proposed for the identification of steps. In [25], the zero-crossing of the pitch angle is also used to detect steps for a rigidly ankle mounted sensor.

In this thesis a step detector based on the pitch angle, which is optimized, but not restricted, for a sensor placed in the pocket of the trousers or attached at any point of the leg is presented (published in [26]). The maximum of the pitch angle is used to detect steps.

2.3 Step Length Estimation

Regarding the step length estimation, the main current approaches can be classified depending on the location of the sensor, as specified in the comparative studies [5, 27, 28].

If the sensor is attached to the body near the center of mass, a classic approach is to model the human body as an inverted pendulum. The major constraint of this biomechanical model is the assumption of a kneeless biped. The model needs a previous calibration to determine the scaling parameter ζ. Additionally, the length of the leg of the pedestrian, γ, is included in the model:

$$s = \zeta \cdot \sqrt{2 \cdot \gamma \cdot v_{\mathrm{p}} - {v_{\mathrm{p}}}^2}, \tag{2.2}$$

where s represents the estimated step length and v_{p} the vertical displacement of the pelvis for each step. This method has been applied in [29]. In [27], a more complex model based on two pendulums, which does not require previous calibration, is analyzed.

Another approach to estimate the step length makes use of the empirical relationship of the acceleration measured in the z-axis of the navigation frame and the step length [17, 19]. This relationship was proposed by Weinberg in [30] as

$$s = \zeta \cdot \sqrt[4]{\alpha_{\mathrm{z_{max}}} - \alpha_{\mathrm{z_{min}}}}, \tag{2.3}$$

where s represents the estimated step length for each step, ζ is a scaling parameter and $\alpha_{\mathrm{z_{max}}}$ and $\alpha_{\mathrm{z_{min}}}$ are the maximum and minimum values of the vertical acceleration for each step. The Weinberg approach requires a previous calibration to determine the scaling parameter ζ and the estimated step length offers similar results compared to the model of Equation (2.2).

If there are no restrictions on the sensor placement [21, 31–33], taking advantage of the relationship between step length, height of the user h, step frequency f and the calibration parameters $(\iota_1, \iota_2, \iota_3)$ different for each user, the step length can be estimated as:

$$s = h \cdot (\iota_1 \cdot f + \iota_2) + \iota_3. \tag{2.4}$$

In this thesis, a step length estimator based on the relationship between the pitch angle and the step length is presented (published in [26] and [34]). This estimator is optimized, but not restricted, for a sensor placed in the pocket of the trousers or attached at any point of the upper part of the leg.

2.4 Vertical Displacement Estimation

Regarding the vertical displacement estimation of the pedestrian for the step-and-heading approach, the barometer or altimeter are the most used sensors to complement inertial systems [35]. The barometer measures the atmospheric pressure. The altimeter is essentially the same instrument, but it matches the atmospheric pressure to the corresponding altitude. Both sensors, however, suffer from inherent dynamic influential factors such as temperature and environmental pressure.

The satellite based systems offer complete 3D positioning, thus, a satellite aided inertial step-and-heading approach could be a viable option. However, signal blockage and strong multipath in indoor environments drastically reduce the availability of satellite-based positioning systems.

Maps can help determining the z-axis position of the pedestrian making use of the floor number, which can be recognised if the building layout is different between floors. Additionally, 3D positioning is also possible with WLAN access points, or UWB if a database or map of their positions in the building is available. However, maps are not always available.

If the strapdown algorithm is used, the double integration over time of the z-axis acceleration yields the z-axis position of the pedestrian [36]. Future accurate sensors will allow the strapdown algorithm to be applied if the sensor is located in an arbitrary part of the body of the pedestrian. With medium-cost MEMS inertial sensors, the strapdown algorithm can only be applied if periodic corrections like ZUPT are possible and this, as previously mentioned, is only valid for shoe-mounted sensors.

Therefore, it can be concluded that the state of the art step-and-heading approach is able to offer 2D positioning. The z-axis position, or the pedestrian vertical displacement estimation, can only be offered by complementing inertial sensors with other sensors such as barometer or WLAN access points or with extra information such as maps. In this thesis, a vertical displacement estimator which provides the first unaided inertial step-and-heading navigation system solving 3D positioning is presented (published in [34]).

2.5 Drift Compensation

The well-known weak point of PDR navigation systems based on medium-cost MEMS inertial sensors is the positioning error that drastically increases with time. This error

has many possible causes such as errors in the step length or vertical displacement estimation, false step detections or orientation errors. Particularly the yaw angle error is the most harmful for the estimation of the position of the pedestrian, as Equation (2.1) shows. Drift is defined in this thesis as the remaining yaw angle error that causes a pedestrian positioning error after applying all possible corrections in the orientation estimation algorithm. The main consequence of the drift error is to gradually twist the computed trajectory making it unrecognizable. There are many methods in the literature to compensate the positioning error caused by the drift, mainly based on the fusion of the inertial measurements with other sources of information like WLAN/UWB ranges, satellite pseudoranges or maps, among others.

In this thesis, a novel algorithm is proposed that computes the drift value by automatically detecting landmarks while the pedestrian walks using solely inertial sensors (published in [37, 38]). The chosen landmarks are corners and stairs, because they are static, abundant and clearly identifiable within the targeted scenarios, i.e. indoors and urban. The proposed algorithms add a great value to the state of the art, since the drift is fed back to the orientation estimation algorithm in order to prevent further yaw angle errors. In the following, the literature regarding drift compensation algorithms is exposed.

Heuristic Drift Elimination Algorithms

Many heuristic drift elimination algorithms have been suggested in the literature for pedestrian indoor positioning. These algorithms assume that pedestrians walk on a straight line within the building in directions which are parallel to the outer walls of the building. If the navigation system detects that the pedestrian does not move on a straight line, these corrections are suspend [39]. After the heuristic drift elimination algorithm was first published, many authors in the literature have proposed similar ideas or improvements, such as coping with complex buildings including curved corridors or wide areas not restricted by corridors [40–42].

Additionally, the heuristic drift elimination has been suggested in combination with other yaw angle corrections such as zero angular rate updates and magnetic measurements [43, 44]. The combination with available maps has also been proposed to restrict the possible yaw angles by taking into account the walls of the buildings [45, 46]. The high non-linearities of the maps force the use of particle filters that weight the particles according to the similarity of their yaw angle with the direction of the walls. The main drawback of this approach is that the yaw angle corrections are usually not fed back to the navigation filter.

Landmark-Based Algorithms

In [47], a study has been carried out concluding that landmarks play an important role for pedestrian navigation, therefore, it is recommendable to develop methods to include landmarks information in pedestrian navigation systems.

One of the most intuitive ways of detecting landmarks within the trajectory described by the pedestrian is using visual information. This information derived from the chosen landmarks is tracked over time in order to use this motion to constrain the drift. In [48], a stereo vision camera is used to extract the optical information of the landmarks. The heuristic drift elimination algorithms can also be seen as landmark-based algorithms, since the manmade straight corridors can be interpreted as landmarks. The main difference is that the landmarks of the heuristic drift elimination algorithms do not need to be tracked over time.

In [49], an algorithm is presented that makes use of detected ramps in buildings for correcting the drift. In the article, shoe-mounted inertial sensors are used and the position of the ramps of the target building is previously known. Ramps are detected through the slope of the terrain and corrections of the position of the pedestrian are applied. However, this approach does not compute the drift value, therefore, although the position is corrected, the proposed approach does not bound the error of the yaw angle.

SLAM-Based Algorithms

A suitable solution to drift reduction is the use of the Simultaneous Localization And Mapping (SLAM) algorithm, which has been used for decades in robotics. The SLAM algorithm simultaneously generates a map of the desired landmarks and locates the user/robot within this map. These landmarks can be detected with any sensor, such as a laser scanner or a camera. The automatic vacuum cleaner, for example, generates a map of the room where the interesting landmarks, i.e. sofa, table, doors, are included and it locates itself within this map.

The SLAM algorithm has also be adapted to pedestrian navigation aiming at reducing the drift error. In order for the SLAM algorithm to successfully reduce the drift, a "loop closure" is necessary. That means, the pedestrian detects landmarks during the trajectory and, when part of the trajectory is re-visited, the landmark is again detected. The same landmark detected twice is an indicative of being again at the same position, therefore, corrections can be applied.

Commonly a particle filter is used that generates particles that move with different errors. When landmarks are re-visited, all particles are weighted depending on the landmarks position. Thus, particles that followed a trajectory with the current drift are high weighted, because they most likely correspond to the detected position. In [50], the 2D space is divided into a grid of uniform and adjacent hexagons, which can be considered

as landmarks. When the same hexagons are re-visited the aforementioned corrections are carried out. The same procedure is applied for 3D trajectories but dividing the volume into hexagonal prisms with eight faces [51]. This procedure can also be applied if the hexagons are identified by the magnetic field intensity [52]. The main drawback of these algorithms is the complexity and processing time to manage the numerous hexagons or hexagonal prisms.

In [53], the proposed landmarks are some location-related activities carried out by the pedestrian, such as sitting, lying or opening doors, among others. Based on the assumption that these activities are always performed at the same place, their repeated detection leads to the aforementioned corrections. The main drawback of the particle filter approach is that yaw angle corrections are usually not fed back to the navigation filter, thus further drift and positioning errors are not prevented.

Chapter 3

Orientation Estimation

When nothing goes right, go left.

To determine the orientation of the sensor, two coordinate frames need to be defined in advance: one coordinate frame attached to the sensor itself and one acting as the reference navigation frame. The body frame and sensor frame are considered equivalent from now on, because the sensor for the pocket navigation system is always attached to the body of the pedestrian. The body frame is composed of three mutually orthogonal axes: x, y and z. The navigation frame is in this thesis the East-North-Up coordinate system. The Easting and the Northern axes point towards East and North direction, respectively. The Up-axis points upwards opposed to the gravity acceleration that points towards the center of the Earth. The origin of this coordinate system is located on the surface of the Earth. Figure 3.1 depicts both coordinate systems and the sensor (body), represented with the blue box.

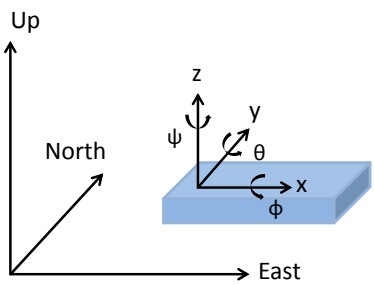

Figure 3.1: Representation of the body frame and the navigation frame. The sensor (body) is depicted as the blue box. Rotations around the body frame axes are represented as ϕ, θ and ψ.

The orientation of the body is defined by the three ordered rotations that align the body frame with the navigation frame, as shown in Figure 3.1. These rotations are represented through the Euler angles roll, pitch and yaw. The first rotation around the x-axis of the body frame defines the roll angle ϕ. The second rotation, the pitch angle θ, is performed around the y-axis of the body frame and aligns the z-axis with the Up-axis of the navigation frame. Last, the rotation needed to align the x- and y-axis of the body

frame with the East- and North-axis of the navigation frame, is defined by the yaw angle ψ.

The orientation estimation algorithm aims at fusing the information of gyroscopes, accelerometers and magnetometers, in an optimal way to obtain the orientation of the body. The Kalman filter is suited for modelling continuous variables whose model equations are linear and model and measurements noise are Gaussian [54]. Taking into account the non-linearities of the equations involved in the orientation computation, it is convenient to use an extended Kalman filter [11] or an unscented Kalman filter [8,9]. However, there is also literature that solves the orientation computation with a linear Kalman filter [10].

Both, the full state and the error state Kalman filter have similar performance, as shown in [55]. In this thesis a full state unscented Kalman filter is chosen, whose state vector $\boldsymbol{x}_{\mathrm{o}}^{\boldsymbol{k}}$ is composed of the orientation angles and the biases $\boldsymbol{b}^{\boldsymbol{k}}$ of the gyroscopes:

$$\boldsymbol{x}_{\mathrm{o}}^{\boldsymbol{k}} = [\phi^k, \theta^k, \psi^k, b_{\mathrm{x}}^k, b_{\mathrm{y}}^k, b_{\mathrm{z}}^k]^T. \tag{3.1}$$

The Kalman filter combines a prediction stage and an update stage. The prediction stage implements the system model, which represents how the system states evolve over time. The update stage incorporates measurements that relate to the system states. Usually the prediction stage is based on the integration over time of the turn rate measurements. The update stage typically incorporates the acceleration and magnetic measurements in order to reduce the error due to the integration over time of the turn rate measurements that contain biases and noise, as shown in Figure 3.2. The diagram shows

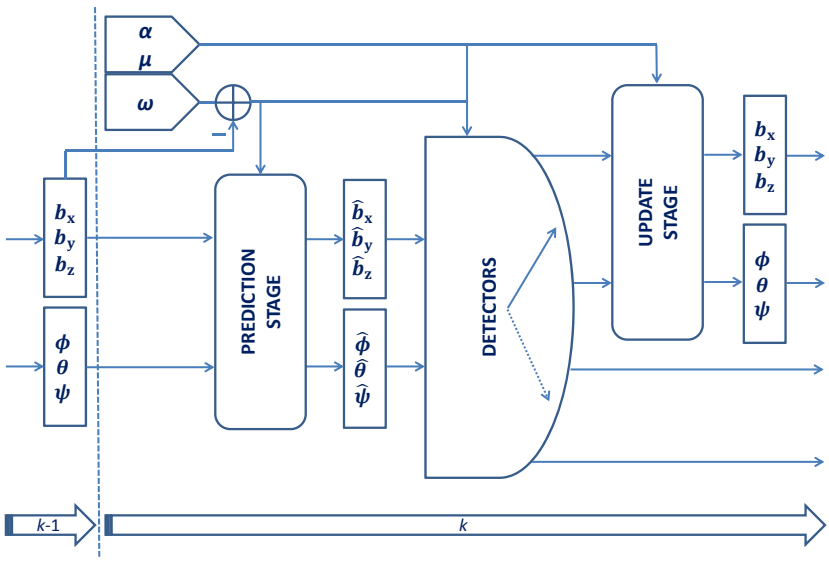

Figure 3.2: Flow diagram of the Kalman filter for de orientation estimation used in this thesis, where $\boldsymbol{\alpha}$, $\boldsymbol{\mu}$ and $\boldsymbol{\omega}$ represent the accelerometer, magnetometer and gyroscope measurements, respectively.

the computation taken for the time stamp k. The variables $\boldsymbol{\alpha}$, $\boldsymbol{\mu}$ and $\boldsymbol{\omega}$ represent the measurements of the accelerometer, magnetometer and gyroscope, respectively. After the prediction stage, the state vector is represented as $\hat{\boldsymbol{x}}_{\mathrm{o}}^{\boldsymbol{k}}$. Next, some characteristics of

the measurements are checked by the detectors, whose goal is to determine whether the updates can be applied or not. If the update stage takes place, the state vector is updated with the measurement vector $\boldsymbol{z}_{\mathrm{o}}^{\boldsymbol{k}}$, and the kth iteration finishes. If no update takes place, $\boldsymbol{x}_{\mathrm{o}}^{\boldsymbol{k}} = \hat{\boldsymbol{x}}_{\mathrm{o}}^{\boldsymbol{k}}$ and the kth iteration finishes.

3.1 Prediction Stage

The gyroscope measures in body frame the turn rate of the body with respect to the inertial frame, $\boldsymbol{\omega}_{\mathrm{ib}}^{\mathrm{b}}$. The turn rate measurement is then composed of:

$$\boldsymbol{\omega}_{\mathrm{ib}}^{\mathrm{b}} = \boldsymbol{\omega}_{\mathrm{nb}}^{\mathrm{b}} + \underbrace{\boldsymbol{\omega}_{\mathrm{en}}^{\mathrm{b}} + \boldsymbol{\omega}_{\mathrm{ie}}^{\mathrm{b}}}_{\omega_{\mathrm{in}}^{\mathrm{b}}}. \tag{3.2}$$

The term $\boldsymbol{\omega}_{\mathrm{nb}}^{\mathrm{b}}$ is the turn rate of the body measured in body frame with respect to the navigation frame. The term $\boldsymbol{\omega}_{\mathrm{en}}^{\mathrm{b}}$ is the transport rate, which represents the turn rate of the navigation frame with respect to the Earth-fixed frame. The term $\boldsymbol{\omega}_{\mathrm{ie}}^{\mathrm{b}}$ represents the turn rate of the Earth with respect to the inertial frame. Last, the term $(\boldsymbol{\omega}_{\mathrm{en}}^{\mathrm{b}} + \boldsymbol{\omega}_{\mathrm{ie}}^{\mathrm{b}})$ equivalent to $\boldsymbol{\omega}_{\mathrm{in}}^{\mathrm{b}}$, represents the rotation of the navigation frame with respect to the inertial frame.

The orientation of the body is given by the term $\boldsymbol{\omega}_{\mathrm{nb}}^{\mathrm{b}}$. However, the gyroscope measures $\boldsymbol{\omega}_{\mathrm{ib}}^{\mathrm{b}}$, thus the term $\boldsymbol{\omega}_{\mathrm{in}}^{\mathrm{b}}$ must be compensated. Particularly for pedestrian navigation, the transport rate is negligible, because the travelled distances are not large enough to significantly change its latitude and longitude within a time stamp. The Earth rotation is measured though. The noise of the medium-cost MEMS gyroscopes is greater than the Earth rotation, which is approximately $15\,^{\circ}\,\mathrm{h}^{-1}$, which provokes that the Earth rotation term is masked. Therefore, this term is usually not compensated, assuming that $\boldsymbol{\omega}_{\mathrm{nb}}^{\mathrm{b}} \approx \boldsymbol{\omega}_{\mathrm{ib}}^{\mathrm{b}}$.

In this thesis, for practical reasons, the term $\boldsymbol{\omega}$ will be used to shorten the term $\boldsymbol{\omega}_{\mathrm{ib}}^{\mathrm{b}}$. To estimate the orientation of the body at each time stamp k, first the biases have to be subtracted from the angular rate $\boldsymbol{\omega}^{\boldsymbol{k}} = [\omega_{\mathrm{x}}^{k}, \omega_{\mathrm{y}}^{k}, \omega_{\mathrm{z}}^{k}]^{T}$. Then, the corrected turn rate measurements are integrated over time.

The direction cosine matrix $\boldsymbol{C}^{\boldsymbol{k}}$ is a 3×3 matrix in which each column is a unit vector along the body axes specified in terms of the navigation axes. That means, the matrix $\boldsymbol{C}^{\boldsymbol{k}}$ represents the rotation of the body frame with respect to the navigation frame at the time k (see Figure 3.1). From this rotation the orientation of the body is deduced.

The orientation at the time k is the orientation at the time $k-1$ modified by the rotation that took place within the last δt seconds, represented in a matrix form as $\boldsymbol{A}^{\boldsymbol{k}}$:

$$\boldsymbol{C}^{\boldsymbol{k}} = \boldsymbol{C}^{\boldsymbol{k-1}} \cdot \boldsymbol{A}^{\boldsymbol{k}}, \tag{3.3}$$

being $\boldsymbol{A}^{\boldsymbol{k}}$

$$\boldsymbol{A}^{\boldsymbol{k}} = \boldsymbol{I} + \frac{\sin(\boldsymbol{\sigma})}{\boldsymbol{\sigma}} \cdot \boldsymbol{B}^{\boldsymbol{k}} + \frac{1-\cos(\boldsymbol{\sigma})}{\boldsymbol{\sigma}^2} \cdot \boldsymbol{B}^{\boldsymbol{k}2}, \tag{3.4}$$

where $\boldsymbol{\sigma} = |\boldsymbol{\omega}^{\boldsymbol{k}}\delta t|$ and

$$\boldsymbol{B}^{\boldsymbol{k}} = \begin{pmatrix} 0 & -\omega_{\mathrm{z}}^{k}\delta t & \omega_{\mathrm{y}}^{k}\delta t \\ \omega_{\mathrm{z}}^{k}\delta t & 0 & -\omega_{\mathrm{x}}^{k}\delta t \\ -\omega_{\mathrm{y}}^{k}\delta t & \omega_{\mathrm{x}}^{k}\delta t & 0 \end{pmatrix}. \tag{3.5}$$

In order to tackle the estimation of the biases of the gyroscope, a noise model is presented in the following. The biases are predicted using the presented model. The turn rate measurements $\boldsymbol{\omega}^{\boldsymbol{k}}$ can be represented as

$$\boldsymbol{\omega}^{\boldsymbol{k}} = \tilde{\boldsymbol{\omega}}^{\boldsymbol{k}} + \boldsymbol{e}^{\boldsymbol{k}}, \tag{3.6}$$

being $\tilde{\boldsymbol{\omega}}^{\boldsymbol{k}}$ the error free turn rate and $\boldsymbol{e}^{\boldsymbol{k}}$ the measurement error. This error will be analyzed with the Allan deviation, which is a well known method to analyze the random noise processes of inertial sensors. In a nutshell, the Allan deviation analysis shows noise deviation over different length in time of averaged data in a double logarithmic chart. At first, a sequence of data, e.g. of several hours or days, is recorded in a static environment, in terms of signal and temperature, in order to observe the long- and the short-term noise processes. This data is divided into several subsequences of the same length and the average is computed for each subsequence. Afterwards the Allan deviation is calculated from all averaged values of the subsequences which have the same length. For detailed formulas, see [56]. The subsequence size varies from one sample to about 10% of the total sequence length, in order to get statistical significance. The subsequences are directly related to the time by the sampling frequency.

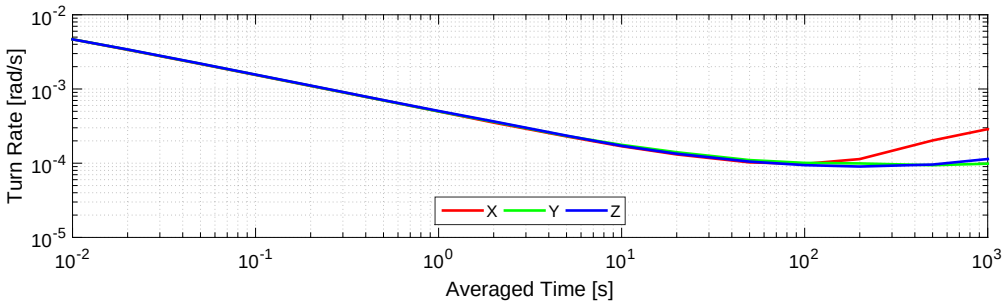

Figure 3.3: Allan deviation analysis of the gyroscopes of the medium-cost MEMS MTw. The different colors represent the three axes of the gyroscope.

Figure 3.3 shows the Allan deviation of the MTw gyroscopes that will be used in this thesis. The figure shows a decreasing trend on the left side of the plot, where the Gaussian white noise is dominant. The Allan deviation of random white noise is reduced by averaging over ever-enlarged sequences. In the right side of the plot, the Allan deviation

shows a change in the trend. In this region the biases, i.e. the slow changing errors, becomes dominant. The bias stability, $\boldsymbol{\beta}$, is located at the minimum of each curve. Therefore, the error of the measurement, $\boldsymbol{e^k}$, can be decomposed in two errors

$$\boldsymbol{e^k} = \boldsymbol{b^k} + \boldsymbol{\nu}, \tag{3.7}$$

where $\boldsymbol{b^k}$ is the bias systematic error and $\boldsymbol{\nu}$ is the sensor noise that can be modelled as Gaussian white noise whose variance is ${\boldsymbol{\sigma_\nu}}^2$.

To determine the biases error an auto-regressive model of order one (AR1) will be used, as it is a suitable model for a random walk process [57]. The AR1 model is defined as

$$\boldsymbol{\hat{b}^k} = \boldsymbol{c} \cdot \boldsymbol{b^{k-1}} + \boldsymbol{n}. \tag{3.8}$$

The biases follow an exponentially correlated noise term defined in the AR1 model as the constant $\boldsymbol{c}$, which is equal to the term $e^{-\frac{1}{\tau}}$, where $\boldsymbol{\tau}$ is the correlation coefficient for each axis and $\boldsymbol{n}$ can be modelled as Gaussian white noise with variance ${\boldsymbol{\sigma_n}}^2$. The variance of the noise $\boldsymbol{n}$ is defined as

$${\boldsymbol{\sigma_n}}^2 = {\boldsymbol{\sigma}_{\text{bias}}}^2 \cdot \left(1 - e^{-\frac{2}{\tau}}\right), \tag{3.9}$$

where ${\boldsymbol{\sigma}_{\text{bias}}}^2$ is the variance of the bias noise.

The sensor error parameters $\boldsymbol{\sigma_n}$, $\boldsymbol{\sigma}_{\text{bias}}$ and $\boldsymbol{\tau}$ can be identified from the Allan deviation plot for each axis. The $\boldsymbol{n}$ value can be directly extracted by intersecting the curves at 1 s. The correlation coefficient $\boldsymbol{\tau}$ is:

$$\boldsymbol{\tau} = \boldsymbol{t_\beta} \cdot f_{\text{s}}, \tag{3.10}$$

being f_{s} the sampling frequency. Lastly, the standard deviation of the bias noise is

$$\boldsymbol{\sigma}_{\text{bias}} = \frac{\boldsymbol{\beta}}{\sqrt{\boldsymbol{\tau}}}. \tag{3.11}$$

Therefore, the lower the β value and the greater the t_β are, the more stable are the biases of the gyroscope.

3.2 Detectors

Accelerometer and magnetic field measurements can be used to extract the partial orientation of the body. However, these measurements should not be constantly used to that end, certain constraints must be fulfilled. Therefore, two detectors that identify periods within the accelerometer and/or the magnetic field measurements can be used to enhance the orientation estimation, have been implemented in this thesis [58].

3.2.1 Zero Acceleration Detector

An accelerometer is capable of measuring a specific force, whose units are $\mathrm{m\,s^{-2}}$. Thus, the sensor measures accelerations like the gravity or accelerations provoked by its proper movement. In order to correctly use the acceleration measurements to estimate the orientation, only the gravity acceleration has to be measured. The *zero acceleration detector* identifies during the walk periods of zero or quasi-zero acceleration due to proper movement of the body. Taking the advantage that the direction and magnitude of the gravity field in the navigation frame are known, it is possible to determine the partial orientation of the body by only measuring the gravity.

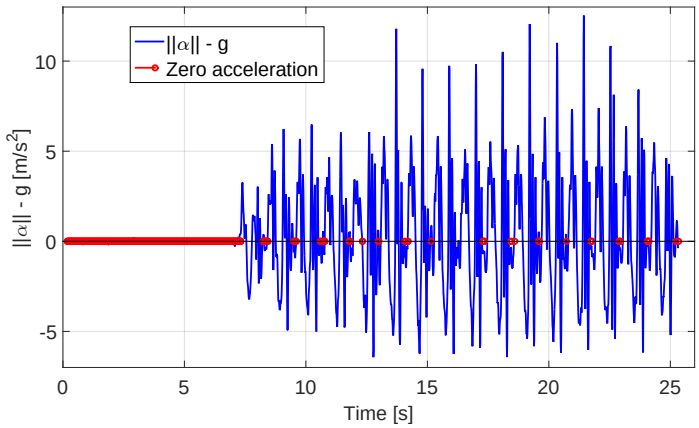

Figure 3.4: The blue curve represents the norm of the three-axis accelerometer measurements recorded during a short walk with the sensor placed in the front pocket of the trousers of the pedestrian. The red dots represent periods of zero or quasi-zero acceleration identified by the *zero acceleration detector*.

Figure 3.4 shows in blue the norm of the three-axis accelerometer measurements, $||\boldsymbol{\alpha}||$, recorded during a short walk with the sensor placed in the front pocket of the trousers of the pedestrian. The gravity acceleration, g, has been cancelled. The first 8 s the pedestrian was standing still, therefore only the gravity is measured. The red dots represent periods of zero or quasi-zero acceleration identified by the *zero acceleration detector*. As shown in the figure, during the walk short periods of zero or quasi-zero acceleration are found that correspond to the moments when the leg carrying the sensor is perpendicular to the floor surface. These periods are shorter or longer depending on the pedestrian walking speed, tending to disappear if the pedestrian runs.

3.2.2 Magnetic Distortions Detector

Magnetometers measure magnetic fields, e.g. the Earth magnetic field, which can be modelled as a dipole. At any location, the magnetic field can be represented by a three-dimensional vector. The angle between the magnetic and the true North is called declination. Facing the magnetic North, the angle the field makes with the horizon is called inclination. The values of intensity, inclination and declination change with time for the

same location and are different for different locations on the Earth. Taking the advantage that the direction and magnitude of the field in the navigation frame are known, by measuring only the Earth magnetic field it is possible to determine the partial orientation of the body. The angle representing the rotation around the axis parallel to the magnetic field is not determined.

The magnetometer has historically been discarded for indoor navigation applications, since the Earth magnetic field is usually perturbed due to the proximity of ferromagnetic materials and electric currents, common in indoor and urban environments. Therefore, the *magnetic distortions detector* identifies during the walk the periods of constant or quasi-constant magnetic field.

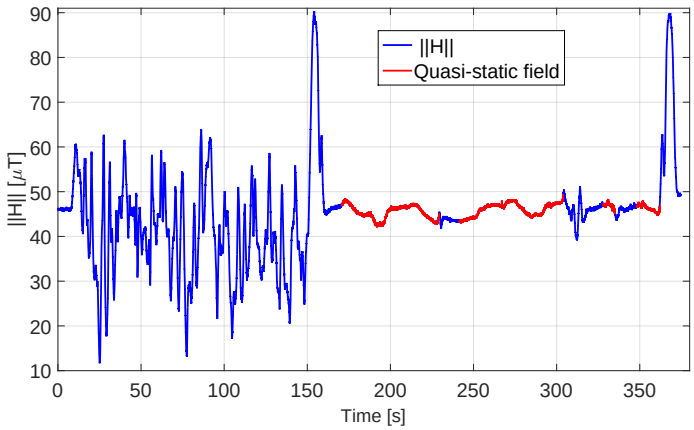

Figure 3.5: The blue curve represents the norm of the three-axis magnetic field measurements recorded during a short walk with the sensor placed in the front pocket of the trousers of the pedestrian. In red, periods of quasi-constant magnetic field identified by the *magnetic distortions detector* are marked.

Figure 3.5 shows in blue the norm of the three-axis magnetic field measurements, $||\boldsymbol{H}||$, recorded during a short walk with the sensor placed in the pocket of the trousers of the pedestrian. The red curve represents periods of constant or quasi-constant magnetic field identified by the *magnetic distortions detector*. The first 150 s the pedestrian was walking indoors, in a building office. At second 160 the pedestrian went out through an automatic door and was walking outdoors until second 370 for walking back indoors through the same automatic door. At second 320 the pedestrian walked approximately at 1 m distance from a parked car. As the figure shows, it is less likely that the *magnetic distortions detector* is activated indoors, unless the pedestrian is standing still. Additionally, the detector is not continuously activated outdoors, because some ferromagnetic objects placed in the vicinity might distort the measured magnetic field. The *magnetic distortions detector* not only checks the magnitude of the measured magnetic field, but also its orientation and it is activated only if both parameters are constant or quasi-constant.

3.3 Update Stage

There are algorithms in the literature that only use acceleration and magnetic field measurements to compute the orientation [59, 60], without integrating turn rate measurements. Acceleration and magnetic field measurements will be incorporated in this thesis as updates in the orientation estimation algorithm. These updates are implemented to improve the orientation estimation. Usually the updates are signals directly measured by the sensors, but also pseudo-measurements can act as updates. The term pseudo-measurement refers to non-directly measured but computed signals. The measurements and pseudo-measurements will be notated with a bar symbol $\bar{\cdot}$.

The detectors detailed in the previous section are in charge of activating these updates. If several updates $\boldsymbol{z}_{\mathrm{o}_i}^{\boldsymbol{k}}$ for $i = \{1, 2, ...\}$ are simultaneously activated, they are applied one after the other. In the case that none of the updates is activated, $\boldsymbol{x}_{\mathrm{o}}^{\boldsymbol{k}} = \hat{\boldsymbol{x}}_{\mathrm{o}}^{\boldsymbol{k}}$ and the kth iteration finishes.

3.3.1 Absolute Gravity Update

During the walk, there are periods in which the acceleration due to the movement of the body is zero or quasi-zero. The *zero acceleration detector* is used to identify these periods. During these periods only the gravity acceleration is measured. In such case, the orientation angles roll and pitch can be extracted at the time k as follows:

$$\bar{\phi}^k = \arctan\left(\frac{\alpha_{\mathrm{y}}^k}{\alpha_{\mathrm{z}}^k}\right) \tag{3.12}$$

and

$$\bar{\theta}^k = \arctan\left(\frac{-\alpha_{\mathrm{x}}^k}{\sqrt{\alpha_{\mathrm{y}}^{k\,2} + \alpha_{\mathrm{z}}^{k\,2}}}\right). \tag{3.13}$$

The measurement vector $\boldsymbol{z}_{\mathrm{o}}^{\boldsymbol{k}}$ of the Kalman filter at the time k can be written as:

$$\boldsymbol{z}_{\mathrm{o}}^{\boldsymbol{k}} = [\bar{\phi}^k, \bar{\theta}^k]^T. \tag{3.14}$$

3.3.2 Differential Gravity Update

Likewise, within the periods of zero or quasi-zero acceleration, the acceleration at the current time can be computed applying the rotation of the last δt seconds, $\boldsymbol{A}^{\boldsymbol{k}}$, to the acceleration measured at the previous time $\boldsymbol{\alpha}^{\boldsymbol{k-1}}$ as follows:

$$\bar{\boldsymbol{\alpha}}^{\boldsymbol{k}} = \boldsymbol{A}^{\boldsymbol{k}} \cdot \boldsymbol{\alpha}^{\boldsymbol{k-1}}. \tag{3.15}$$

The *zero acceleration detector* is used to identify these periods. The pseudo-measurement $\bar{\boldsymbol{\alpha}}^{\boldsymbol{k}}$ is used as update. This update has been proposed in [61]. The measurement vector

$\boldsymbol{z}_{\mathrm{o}}^{\boldsymbol{k}}$ of the Kalman filter at the time k can be written as:

$$\boldsymbol{z}_{\mathrm{o}}^{\boldsymbol{k}} = [\bar{\alpha}_{\mathrm{x}}^{k}, \bar{\alpha}_{\mathrm{y}}^{k}, \bar{\alpha}_{\mathrm{z}}^{k}]^{T}. \tag{3.16}$$

3.3.3 Absolute Magnetic Field Update

During the walk there are periods in which the measured magnetic field is constant or quasi-constant. The *magnetic distortions detector* is used to identify these periods. At the beginning of the quasi-constant magnetic field period, the measured magnetic field is projected onto the navigation frame and chosen as reference $\bar{\boldsymbol{\mu}}_{\mathrm{r}}$. It is assumed that, during quasi-constant magnetic field periods, the measured magnetic field does not change. Therefore, the reference magnetic field is used as pseudo-measurement for the update. This update has been proposed in [11] and further analyzed in [15]. The measurement vector $\boldsymbol{z}_{\mathrm{o}}^{\boldsymbol{k}}$ of the Kalman filter at the time k can be written as:

$$\boldsymbol{z}_{\mathrm{o}}^{\boldsymbol{k}} = [\bar{\mu}_{\mathrm{r_x}}, \bar{\mu}_{\mathrm{r_y}}, \bar{\mu}_{\mathrm{r_z}}]^{T}. \tag{3.17}$$

3.3.4 Differential Magnetic Field Update

Likewise, within these periods of constant or quasi-constant magnetic field, the magnetic field at the current time can be computed applying the rotation of the last δt seconds, $\boldsymbol{A}^{\boldsymbol{k}}$, to the magnetic field measured at the previous time $\boldsymbol{\mu}^{\boldsymbol{k-1}}$ as follows:

$$\bar{\boldsymbol{\mu}}^{\boldsymbol{k}} = \boldsymbol{A}^{\boldsymbol{k}} \cdot \boldsymbol{\mu}^{\boldsymbol{k-1}}. \tag{3.18}$$

The *magnetic distortions detector* is used to identify these periods. The pseudo-measurement $\bar{\boldsymbol{\mu}}^{\boldsymbol{k}}$ is used as update. This update has been proposed in [9] and [11]. The measurement vector $\boldsymbol{z}_{\mathrm{o}}^{\boldsymbol{k}}$ of the Kalman filter at the time k can be written as:

$$\boldsymbol{z}_{\mathrm{o}}^{\boldsymbol{k}} = [\bar{\mu}_{\mathrm{x}}^{k}, \bar{\mu}_{\mathrm{y}}^{k}, \bar{\mu}_{\mathrm{z}}^{k}]^{T}. \tag{3.19}$$

3.3.5 Absolute Compass Update

If the measured magnetic field is homogeneous, the yaw angle can be computed at each time k as follows:

$$\bar{\psi}^{k} = \arctan\left(\frac{-\mu_{\mathrm{h_x}}^{k}}{\mu_{\mathrm{h_y}}^{k}}\right) + d, \tag{3.20}$$

being $\boldsymbol{\mu}_{\mathrm{h}_{\boldsymbol{i}}}^{\boldsymbol{k}}$ where $i = \{\mathrm{x,y}\}$ is the magnetic field intensity at the time k for the i-axis projected onto the horizontal plane. The declination angle, which is known for every location on the Earth, is represented by d. The measurement z_{o}^{k} of the Kalman filter at the time k can be written as:

$$z_{\mathrm{o}}^{k} = \bar{\psi}^{k}. \tag{3.21}$$

Since indoor and urban environments do not usually present homogeneous magnetic fields due to ferromagnetic materials or electric currents, an alternative way to extract information from a perturbed magnetic environment has recently been proposed. This procedure makes use of the fact that the magnetic distortions are highly modulated in space, but relatively constant in time to create a magnetic signature [14].

3.3.6 Zero Angular Rate Update

Within the periods where the sensor is not rotating, the turn rate measurements can be assumed to be zero. This assumption implies that any turn rate measured during these periods is due to errors, e.g. biases. This update has been proposed in [62]. The measurement vector $\boldsymbol{z}_{\mathrm{o}}^{\boldsymbol{k}}$ of the Kalman filter at the time k can be written as:

$$\boldsymbol{z}_{\mathrm{o}}^{\boldsymbol{k}} = [0, 0, 0]^T. \tag{3.22}$$

3.4 Experimental Results

This section offers a detailed analysis of the proposed orientation estimation filter for a pedestrian pocket navigation system. The evaluation of the estimation of the Euler angles will be strongly related to the estimation of the biases of the gyroscope. This perspective has rarely been covered by the literature which is more likely to be focused only on the estimation of the yaw angle. The experiments have been derived with quasi-error-free measurements in order to have controlled errors and medium-cost MEMS inertial sensors to endorse the obtained results.

3.4.1 Euler Angles Reference System

The reference chosen for this chapter is a fiber optic gyroscope (FOG). In order to assess that the FOG measurements can be considered quasi-error-free, 14 h of static turn rate measurements have been recorded to compute the Allan deviation shown in Figure 3.6. The continuous lines depict the noise analysis of the FOG and the dashed lines depict the noise analysis of the gyroscopes of the medium-cost MTw MEMS gyroscopes from Xsens (see [63]). The colors represent the mutually orthogonal gyroscopes in the axes x, y and z.

The noise analysis of both sensors shows a decreasing trend on the left side of the plot, where the white noise is dominant. This value can be directly extracted by intersecting the curves at 1 s. The FOG white noise is two orders of magnitude lower than the medium-cost MEMS gyroscopes white noise. On the right side of the plot, the Allan deviation shows a change in the trend. In this region the biases, i.e., the slow changing errors, become dominant. The bias stability, β, is located at the minimum.

Thus, the lower the β value and the greater the t_β are, the more stable are the biases of the gyroscopes. The β value is two orders of magnitude smaller for the FOG than for a medium-cost MEMS gyroscopes and t_β one order of magnitude greater for the FOG than for the medium-cost MEMS gyroscopes [64]. Consequently, the FOG biases are considerably more stable than the medium-cost MEMS gyroscopes biases.

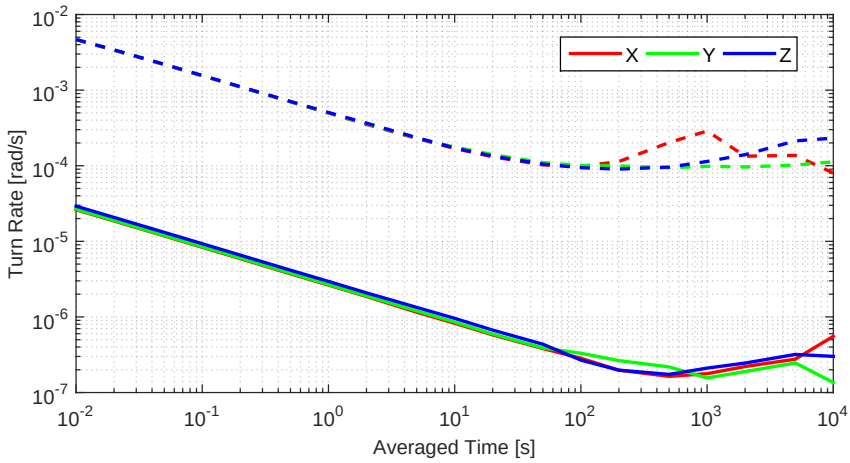

Figure 3.6: Allan deviation analysis of the FOG and the gyroscopes of the MEMS MTw in continuous and dashed line, respectively.

In order to evaluate the magnitude of the FOG biases and their effect on the orientation angles, the integration of 1 h of turn rate FOG measurements after correcting the Earth rotation has been computed (see Figure 3.7). The orientation angles, which should be constant because the FOG was static, have been calculated without subtracting the biases estimation or applying updates.

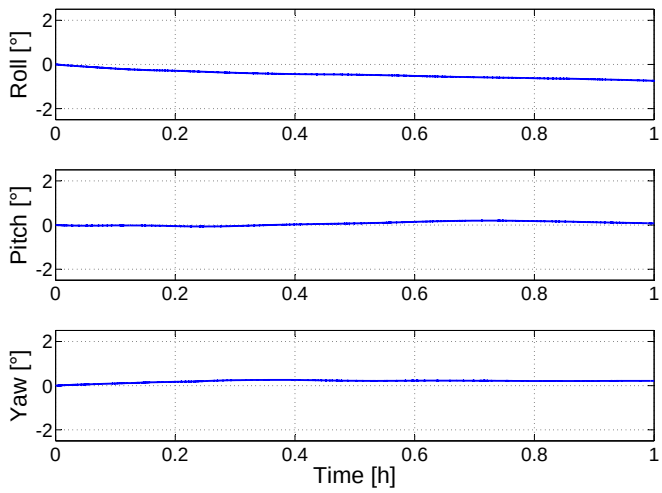

Figure 3.7: Integration 1 h of FOG turn rate measurements recorded for the Allan deviation analysis.

The FOG does not measure the transport rate since the aforementioned measurements were static, however it measures the rotation of the Earth, ω_e, which has a value of $7.29 \times 10^{-5}\,\mathrm{rad\,s^{-1}}$, approximately $15\,^\circ\,\mathrm{h}^{-1}$. Before integrating over time the turn rate

measurements to compute the orientation, the Earth rotation has to be compensated as follows:

$$\boldsymbol{\omega}_{\mathrm{nb}}^{\mathrm{b}} = \boldsymbol{\omega}_{\mathrm{ib}}^{\mathrm{b}} - \boldsymbol{C}_{\mathrm{n}}^{\mathrm{b}} \cdot \boldsymbol{\omega}_{\mathrm{in}}^{\mathrm{n}}, \tag{3.23}$$

being $\boldsymbol{C}_{\mathrm{n}}^{\mathrm{b}}$ the transformation matrix from the navigation frame to the body frame and

$$\boldsymbol{\omega}_{\mathrm{in}}^{\mathrm{n}} = \omega_{\mathrm{e}} \cdot [0, \cos(\lambda), \sin(\lambda)]^T, \tag{3.24}$$

where λ is the latitude.

As visible in Figure 3.7, the computed orientation angles are not equal to zero. The error, however, does not exceed 1° over 1 h in any angle. The slight error is due to the white noise and biases of the FOG which have not been compensated. A MEMS gyroscopes biases value of $0.1\,^{\circ}\,\mathrm{s}^{-1}$ yields to 360° over 1 h. Since the FOG biases are orders of magnitude smaller and more stable than the medium-cost MEMS gyroscopes biases and the experiments last less than 1 h, the error due to FOG biases will be considered negligible and the FOG turn rate measurements as quasi-error-free.

3.4.2 Euler Angles Evaluation

The IMU DSP-1750 from KVH, which contains the previously analyzed FOG and also MEMS accelerometers, is attached to the upper front part of the leg (see Figure 3.8(a)) as if it were introduced in the pocket.

(a) (b)

Figure 3.8: (**a**) The inertial data for the experiments analyzed in this section has been recorded with the IMU DSP-1750 attached to a wooden surface which is fastened to the leg, as if the sensor were introduced in the pocket. (**b**) Scenario of the experiments detailed in this section.

Figure 3.9(a) shows the satellite image overlay of the trajectory depicted in red. The scenario of the walk is shown in Figure 3.8(b). The duration of the walk is 39 min and it consists of a three round trip trajectory of 600 m on each direction, thus 3 km in total approximately. The medium-cost MEMS inertial sensor MTw from Xsens has been attached to the flat surface of the IMU DSP-1750 shown in Figure 3.8(a) in order to record acceleration and turn rate measurements with MEMS sensors and the IMU DSP-1750

simultaneously.

Figure 3.9: Satellite image overlay of the scenario where the experiment has been carried out. The red curve represents the computed trajectory of 39 min over 3 km using the IMU DSP-1750 measurements.

To obtain the trajectory of Figure 3.9, the orientation has been computed integrating the FOG turn rate measurements without subtracting the biases estimation or applying updates. Therefore, the FOG white noise and biases cause an error in the orientation, as previously explained. The Earth rotation has been compensated. Regarding the position computation, the algorithms described in [34] have been used for the step detection and step length computation.

The orientation angles for the medium-cost MTw inertial measurements have been estimated using the orientation estimation filter proposed in this thesis. The *Absolute Gravity Update* has been applied during periods of zero or quasi-zero acceleration.

Figure 3.10 shows the error curves of the Euler angles estimated with the MEMS sensor MTw, assuming as reference the FOG quasi-error-free turn rate measurements. It is remarkable that roll and pitch errors are limited and oscillate around 0°. These errors are stable after a long operation time, such as 39 min. However, the error of the yaw angle is constantly increasing. The growing rate is more pronounced until minute 15 and then the slope decreases. This behaviour is due to the bias of the z-axis of the gyroscope. Since the *Absolute Gravity Update* does not offer information of the yaw angle, its error curve grows with time, unlike the roll and pitch angle error curves.

The change of slope in Figure 3.10(c) corresponds to the estimation of the bias of the z-axis. The initial bias value is set to zero and then the estimation process starts. From minute 15 on, the estimation of the bias of the z-axis becomes more accurate, however still enough mistaken to accumulate an error of more than 50° in 25 min. These results yield to the conclusion that the *Absolute Gravity Update* is able to keep limited the error in roll and pitch angles, however it has no positive effect on the yaw angle. Therefore, the error in the yaw angle grows with time because it is not observable through the gravity field. In order to decrease the error of the yaw angle, the z-axis bias of the gyroscope should be correctly estimated. This is possible through the *Differential Magnetic Field Update*, among others.

Obtaining a precise analysis of the estimation of the biases is difficult, because their value is not accurately known for MEMS sensors. Therefore, in this thesis the FOG quasi-error-free turn rate measurements are used to artificially add known and controlled biases values in order to emulate MEMS sensors. In addition, a complete evaluation of the usability of the magnetic field for the gyroscope biases estimation through the

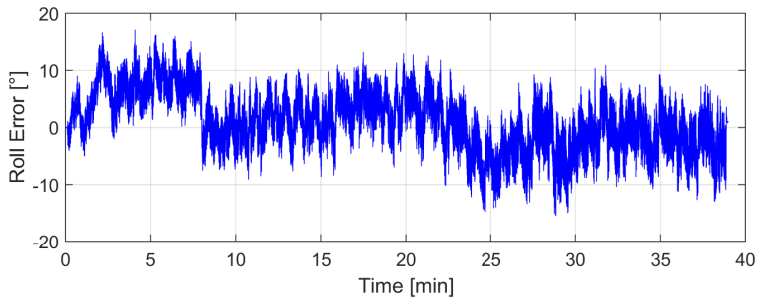

(a) Roll

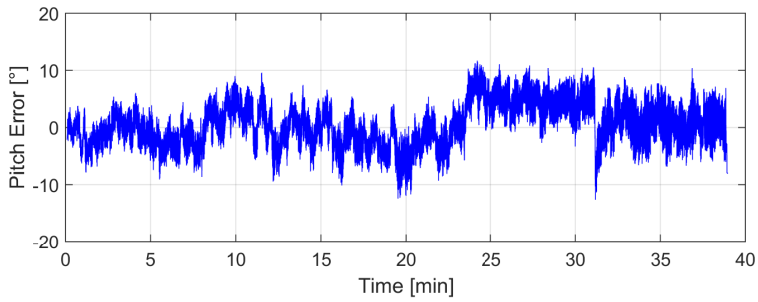

(b) Pitch

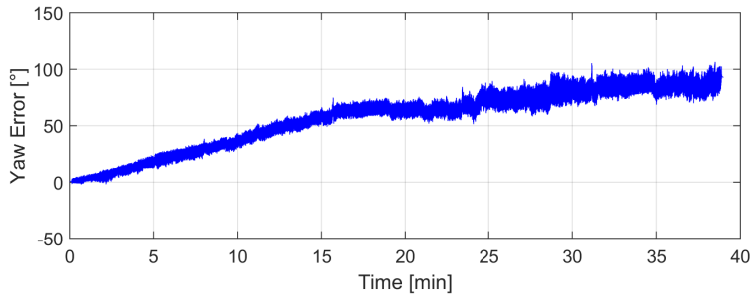

(c) Yaw

Figure 3.10: Curves representing the Euler angles estimated with the MEMS sensor MTw subtracted to the Euler angles estimated with the FOG quasi-error-free turn rate measurements.

Differential Magnetic Field Update will be driven. The goal of this evaluation is to analyze the estimation of the biases under different magnetic field distributions, keeping the rest of the conditions invariant. The obtained results are then assessed by real MEMS inertial sensor measurements.

3.4.3 Gyroscopes' Bias Reference System

In order to evaluate if the biases are correctly estimated, it is necessary to know in advance their exact value. Artificial noise will be added to the quasi-error-free turn rate measurements in order to emulate similar quality measurements as if they were recorded with MEMS sensors.

The IMU DSP-1750, which embeds the FOG and MEMS accelerometers (see Figure 3.11) will be used to that end. The acceleration measurements, $\boldsymbol{\alpha}$, contain noise

and biases characteristic from the MEMS. The turn rate measurements of the FOG, $\tilde{\boldsymbol{\omega}}$, are considered quasi-error-free. These quasi-error-free turn rate measurements are used to generate different magnetic field measurements, $\boldsymbol{\mu}$, as indicated in the diagram of Figure 3.11. Therefore, a single real walk recorded with the IMU DSP-1750 is combined with a variety of magnetic field distributions. Magnetic field distributions corresponding to different locations on the Earth have been generated with homogeneous magnetic fields, $\boldsymbol{H}_{\infty}$, such as North Pole, Munich (Germany) and the Equator, and also perturbed magnetic fields, $\boldsymbol{H}_{\pi}$.

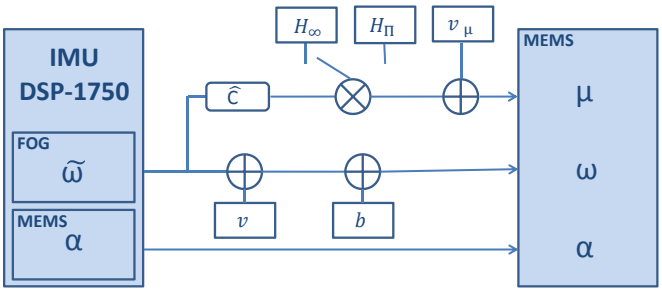

Figure 3.11: Flow diagram of the processing of the measurements recorded with the IMU DSP-1750 to generate different magnetic field distributions and to add noise to the quasi-error-free turn rate measurements, where $\boldsymbol{\alpha}$, $\boldsymbol{\mu}$ and $\boldsymbol{\omega}$ represent the accelerometer, magnetometer and gyroscope measurements, respectively.

The acceleration measurements are not modified, because the accelerometers integrated in the IMU DSP-1750 are MEMS sensors. In order to emulate MEMS gyroscopes measurements, $\boldsymbol{\omega}$, white Gaussian noise $\boldsymbol{v}$ and biases $\boldsymbol{b}$ are added to the quasi-error-free turn rate measurements $\tilde{\boldsymbol{\omega}}$, as follows:

$$\boldsymbol{\omega} = \tilde{\boldsymbol{\omega}} + \boldsymbol{v} + \boldsymbol{b}. \tag{3.25}$$

The noise and bias values have been chosen based on the values of the medium-cost MEMS MTw and will be detailed in the next section.

To generate magnetic measurements $\boldsymbol{\mu}$ the orientation of the sensor $\hat{\boldsymbol{C}}$ is computed from the quasi-error-free turn rate measurements and multiplied by the magnetic field $\boldsymbol{H}$. Finally white Gaussian noise $\boldsymbol{v}_{\mu}$ is added as follows:

$$\boldsymbol{\mu} = \hat{\boldsymbol{C}}^{T} \cdot \boldsymbol{H} + \boldsymbol{v}_{\mu}, \tag{3.26}$$

where $\boldsymbol{H}$ is either the homogeneous magnetic field $\boldsymbol{H}_{\infty}$ or the perturbed magnetic field $\boldsymbol{H}_{\pi}$. The $\boldsymbol{v}_{\mu}$ value is chosen based on the noise of the magnetometer integrated in the medium-cost MEMS MTw and will be detailed in the next section.

Different locations on the Earth have been chosen due to their different magnetic field distributions. The homogeneous magnetic field values, $\boldsymbol{H}_{\infty}$, have been rounded compared to the real values: for example, the Munich Earth Observatory has reported an average intensity of 48 µT, an inclination angle of 64.23° and a declination angle of 2.57° for

April 2015 [65]. Table 3.1 shows all the homogeneous magnetic fields, $\boldsymbol{H_\infty}$, expressed in East-North-Up coordinates and measured in µT.

Table 3.1: Reference Magnetic Fields, $\boldsymbol{H_\infty}$, Measured in µT

North Pole	Equator	Munich
$65 \cdot [0, 0, -1]^T$	$25 \cdot [0, 1, 0]^T$	$48 \cdot [0, \cos(64°), -\sin(64°)]^T$

In order to generate the perturbed magnetic field, $\boldsymbol{H_\pi}$, the equations of a homogeneous field perturbed by one single ferromagnetic object are analytically computed. Then, a template of several objects is created. More realistic scenarios are so complicated that solutions to Maxwell's equations cannot be obtained analytically. Solving these fields is possible numerically. However, for simplicity, the analytical solutions obtained in idealized scenarios are used.

An infinite length iron cylinder along the Up-axis with relative permeability $\mu_\mathrm{r} = 200$ has been chosen. Due to this geometry, the infinite cylinder will not influence the resulting perturbed magnetic field in the Up-axis. For this reason, the perturbed magnetic field is generated from a homogeneous magnetic field which does not have Up-component, e.g. the Equator, as shown in Table 3.1. The inner magnetic field of the object is not considered, since the pedestrian cannot step into the cylinder.

The magnetic field can be derived from the Maxwell's equations, which are four partial differential equations that describe how electric and magnetic fields are generated and altered by each other and by charges and currents. If the magnetic field is static, the time derivatives are zero and the system of equations decouples. The magnetic strength vector field can be expressed as the gradient of a scalar potential field, Ψ:

$$\boldsymbol{H} = -\nabla\Psi. \tag{3.27}$$

Since the influence of the ferromagnetic object on the homogeneous magnetic field decays with increasing distance, the solution of the boundary value, $-\nabla\Psi$, at infinite distance converges to the homogeneous magnetic field $\boldsymbol{H_\infty}$, in this case the Equator.

$$\lim_{r\to\infty} -\nabla\Psi = \boldsymbol{H_\infty}. \tag{3.28}$$

The desired magnetic field must fulfill the boundary condition of Equation (3.27), therefore the solution yields [66]

$$\begin{aligned} -\nabla\Psi = ||\boldsymbol{H_\infty}|| \cdot \frac{\mu_\mathrm{r} - 1}{\mu_\mathrm{r} + 1} \cdot \frac{r_\mathrm{c}}{r} \cdot \sin(2\rho) \cdot u_\mathrm{E} + \\ ||\boldsymbol{H_\infty}|| \cdot \left(1 + \frac{\mu_\mathrm{r} - 1}{\mu_\mathrm{r} + 1} \cdot \frac{r_\mathrm{c}}{r} \cdot \cos(2\rho)\right) \cdot u_\mathrm{N}, \end{aligned} \tag{3.29}$$

being $u_\mathrm{E}, u_\mathrm{N}$ the unity vectors in East and North direction respectively, r_c the radius of

the cylinder, μ_r the relative permeability of the material of the cylinder,

$$r = \sqrt{x^2 + y^2} \tag{3.30}$$

and

$$\rho = \arctan\left(\frac{x}{y}\right). \tag{3.31}$$

Using Equation (3.29) and the reference magnetic field of the Equator, two different magnetic field distributions have been generated: one perturbed by a cylinder of $r_\mathrm{c} = 30\,\mathrm{cm}$ and another perturbed by a cylinder of $r_\mathrm{c} = 2\,\mathrm{m}$. The magnetic field template shown in Figure 3.12 has been then composed by four small cylinders representing streetlights and one large cylinder representing a parked car.

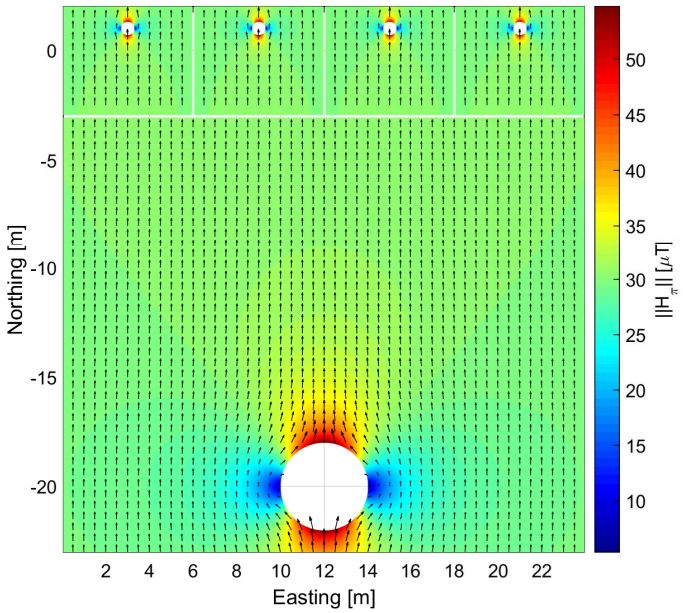

Figure 3.12: Generated magnetic field $\boldsymbol{H_\pi}$ for a perturbed environment representing four streetlights and a parked car. The color represents the magnetic field intensity, measured in µT, and the arrows represent the orientation.

As previously specified, the magnetic field template of Figure 3.12 is not considering the influence of all cylinders simultaneously. Since the influence of the ferromagnetic object on the homogeneous magnetic field decays with increasing distance, a safe distance to patch different fields has been considered. However, in order to ensure that the *Differential Magnetic Field Update* is correctly applied, the update will be deactivated if the pedestrian walks over the transition of two patches. The transitions have been marked with a white line in the figure.

3.4.4 Gyroscopes' Bias Evaluation

In this section the results of the experiments that aim to evaluate the effectiveness of using magnetic field measurements to estimate the biases of medium-cost MEMS gyroscopes will

be summarized. In order to properly observe the estimation process of the biases, the quasi-error-free turn rate measurements with added noise and constant biases are used. This is detailed in the first part of the experiments.

The results of the first part of the experiments will be endorsed using measurements recorded with the MEMS MTw sensor. On the one hand, for the second part of the experiments the biases inherent to MEMS sensors are unknown. On the other hand, the results using real biases should be consistent to the first experiments where a constant bias model has been assumed.

3.4.4.1 Evaluation with Quasi-Error-Free Measurements

For this section, the measurements of the IMU DSP-1750 corresponding to the walk previously described and shown in Figure 3.9 will be used. The values of the white noise and biases have been added to the recorded FOG turn rate reference measurements and to the generated magnetic field measurements are summarized in Table 3.2.

Table 3.2: Values of Noise and Biases

	$\boldsymbol{\nu}$ [$^\circ\,\mathrm{s}^{-1}$]	$\boldsymbol{b}$ [$^\circ\,\mathrm{s}^{-1}$]	$\boldsymbol{\nu_\mu}$ [µT]
x-axis		-0.1	
y-axis	0.1	0.1	0.015
z-axis		-0.1	

Figure 3.13 shows the estimated trajectory of the walk in red and the infinite cylinders used to generate magnetic measurements in a perturbed environment, $\boldsymbol{H_\pi}$. The green points represent the streetlights and the blue points represent the parked cars. This is the result of the magnetic template of Figure 3.12 composed of four streetlights in the upper part and one parked car in the lower part replicated in the Easting direction to cover the complete trajectory.

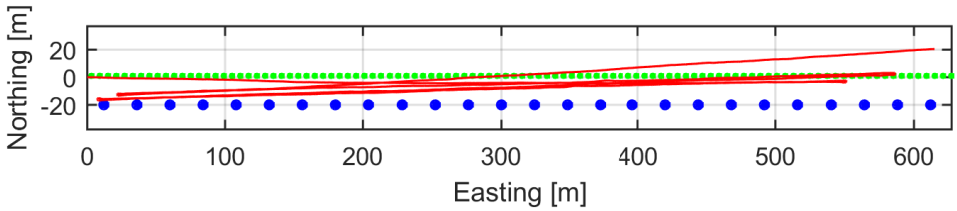

Figure 3.13: This figure shows in red the estimated trajectory of the walk, the blue points represent parked cars and the green points represent streetlights. The figure shows the magnetic template shown in Figure 3.12 composed of four streetlights in the upper part and one parked car in the lower part replicated in the East-axis in order to cover the complete trajectory.

The following experiments are divided into three sections which address the biases estimation without using the magnetic field, the biases estimation under homogeneous magnetic fields emulating different locations on the Earth and the estimation of the biases under perturbed magnetic fields. Additionally, the effects of the calibration of the

magnetometer are analyzed. The configuration parameters of the orientation estimation filter will remain fixed for all experiments in this section.

Biases Estimation without Using Magnetic Field Measurements The following analysis aims at evaluating the isolated effect of the *Absolute Gravity Update*, since it will be applied in all experiments from now on. It is expected that this update modifies directly the estimations of roll and pitch angles, (see Equations (3.14) and (3.13)). The yaw angle, however, is not observable through this update because it defines the rotation around the Up-axis, which is parallel to the gravity field. The x- and y-axis biases of the gyroscope are also modified, since they are directly related to the angle computation.

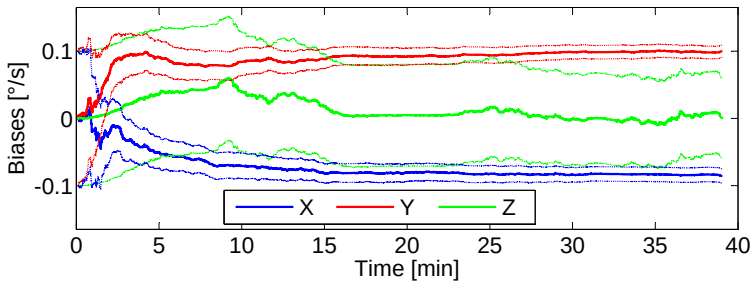

Figure 3.14: Biases estimation over time . The blue curve represents the biases estimation of the x-axis and the red and green the biases estimation of the y- and z-axis respectively using the *Absolute Gravity Update*. The true values are summarized in Table 3.2. The dotted curves represent the uncertainty.

Figure 3.14 shows the estimation of the biases for the three axes of the gyroscope using only the *Absolute Gravity Update*. The figure clearly shows that the bias of the y-axis is correctly estimated through the *Absolute Gravity Update*. Even though the x-axis bias is estimated in the correct direction, the final value does not reach $-0.1\,^{\circ}\,\mathrm{s}^{-1}$ in 39 min, as Table 3.2 indicates. A possible cause is the fact that the *Absolute Gravity Update* is only applied during the periods of zero or quasi-zero acceleration due to the movement of the sensor. These periods are longer or shorter depending on the walking speed of the pedestrian, tending to disappear if the pedestrian runs. For this experiment, the pedestrian travelled 3 km in 39 min. A walking speed of $4.6\,\mathrm{km\,h}^{-1}$ is considered medium-high. Additionally, it has to be considered that the acceleration measurements contain biases that have neither been estimated nor compensated. The *Absolute Gravity Update* implies a reduction of the uncertainty of the biases of the x- and y-axis, as the dotted blue and red curves respectively show.

As a consequence of the poor estimation of the bias in the z-axis, the yaw angle accumulates more drift than roll and pitch, as discussed in [58]. The yaw angle, however, is the most significant orientation angle for pedestrian dead-reckoning, since it represents the heading of the pedestrian. Therefore, further updates are needed in order to correctly estimate the z-axis bias.

Biases Estimation Using Magnetic Measurements from Homogeneous Field The objective of this analysis is evaluating the influence of the magnetic field distribution for homogeneous fields in the biases estimation process. To that end, magnetic field measurements corresponding to different locations on the Earth, i.e. North Pole, Equator and Munich (Germany), have been generated for the trajectory described in the previous experiment.

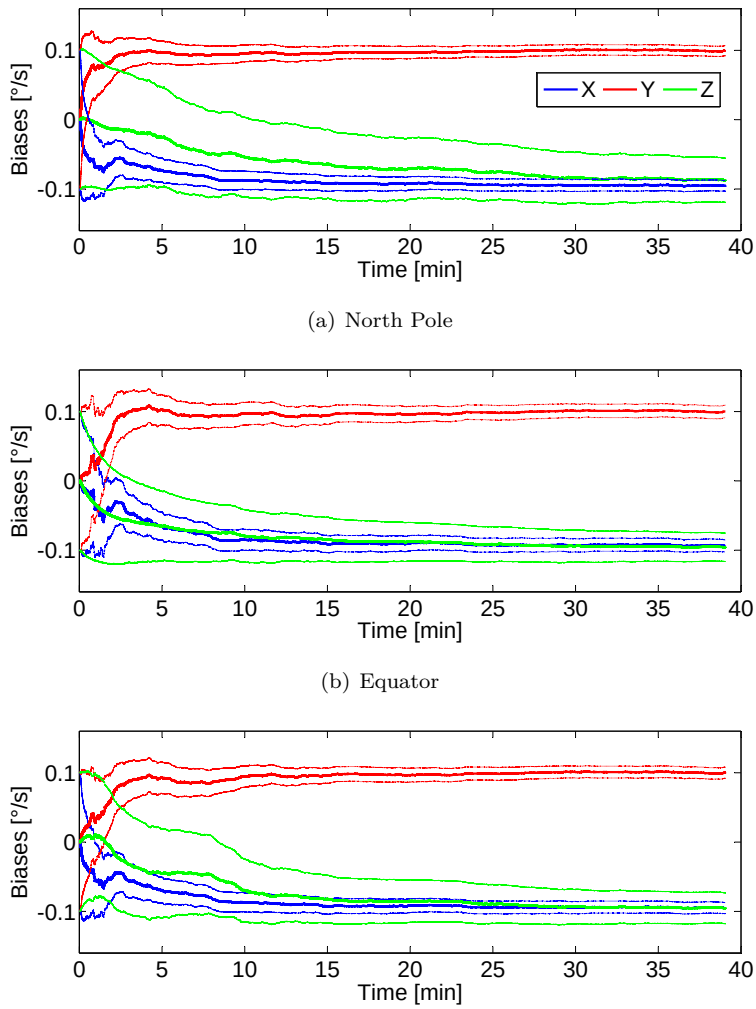

(a) North Pole

(b) Equator

(c) Munich

Figure 3.15: Biases estimation over time considering $\boldsymbol{H}_{\infty}$ of (a) North Pole (b) Equator and (c) Munich. The blue curve represents the biases estimation of the x-axis and the red and green the biases estimation of the y- and z- axis respectively using the *Absolute Gravity Update* and *Differential Magnetic Field Update*. The true values are summarized in Table 3.2. The dotted curves represent the uncertainty.

As Figure 3.15 shows, in all cases the biases tend to the correct value specified in Table 3.2, however, slightly differences can be observed depending on the location of the pedestrian on the Earth. Figure 3.15(a) represents the biases estimation if the red trajectory of Figure 3.13 was located in the North Pole. The magnetic field is distributed only in the Up-axis, which is ideal to observe rotations around the x- and y-axis, however it is rotation invariant for the z-axis. The blue and red curves show a faster estimation process compared with the estimation that uses only the *Absolute Gravity Update*, shown in Figure 3.14. Therefore, the *Differential Magnetic Field Update* also benefits the x- and

y-biases estimation.

Theoretically, the distribution of the North Pole magnetic field does not improve the estimation of the z-axis bias, because rotations around the axis parallel to the Up-axis are not observable. However, as Figure 3.15(a) shows, the bias of the z-axis tends to the correct value, compared with Figure 3.14 where no magnetic information is used. The observation of the z-axis bias is possible thanks to the cyclic movement of the leg of the walking pedestrian, which makes the z-axis of the sensor not being constantly aligned with the Up-axis. Even if the estimation of the z-axis bias takes more time to converge than the other axes, these intermittent periods of no alignment caused by the movement of the leg favour the z-bias observation. In this case, it takes 29 min to reach the value $-0.08\,^{\circ}\,\mathrm{s}^{-1}$.

The *Absolute Gravity Update* alone is not able to aid the z-bias estimation (Figure 3.14) because the periods of zero acceleration while the pedestrian is walking coincide with the leg of the pedestrian completely vertical. Therefore, the sensor z-axis within that periods is always aligned with the Up-axis when the update is activated.

The distribution of the magnetic field of the Equator does not allow observing rotations around the North-axis. However, the y-axis bias estimation is solved using only the *Absolute Gravity Update*, as shown in Figure 3.14. The Equator magnetic field allows observing rotations around the x- and z-axis. The result of Figure 3.15(b) assesses that the bias of the z-axis has more chances to be observed than in the North Pole, as expected. In fact, it takes 10 min to reach the value $-0.08\,^{\circ}\,\mathrm{s}^{-1}$.

Figure 3.15(c) shows the biases estimation for the magnetic field distribution of Munich, which has an inclination angle of 64° resulting in North and Up magnetic field components. As it can be observed, the estimation process of the biases is a mixture of North Pole and Equator. It takes 15 min for the z-bias estimation to reach the value $-0.08\,^{\circ}\,\mathrm{s}^{-1}$.

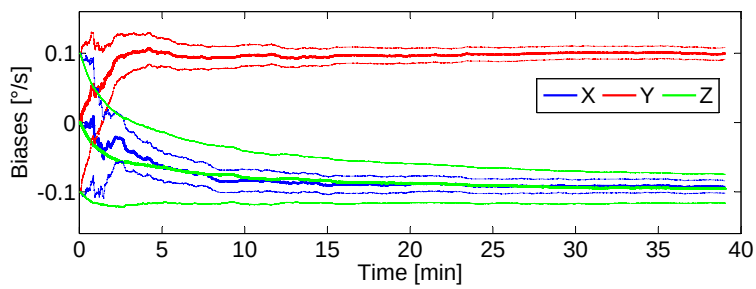

Figure 3.16: Biases estimation over time considering $\boldsymbol{H}_{\infty}$ of Equator (Table 3.1). The orientation of the trajectory of the walk is North-South, instead of the orientation used for previous experiments East-West. The dotted curves represent the uncertainty.

Figure 3.16 shows the estimation process of the biases for the homogeneous magnetic field of the Equator (see Table 3.1). The orientation of the trajectory of the walk has been modified to North-South, instead of the one shown in Figure 3.13, which is East-West oriented. This change has been performed in order to evaluate the influence of the

direction of movement for a predetermined magnetic field distribution. Comparing this figure with Figure 3.15(b), a slightly faster convergence of the y-axis bias can be observed if the trajectory is North-South oriented. This can be explained because rotations around the y-axis are easily observable when walking transversally to the magnetic field rather than walking in parallel. Changes in x- and z-biases are not significant.

Biases Estimation Using Magnetic Measurements from Perturbed Field The following analysis aims at evaluating the influence of magnetic perturbations in the biases estimation process. The homogeneous magnetic field, $\boldsymbol{H}_{\infty}$, of the Equator has been perturbed by series of ferromagnetic objects spread along the trajectory of the walk. The magnetic template shown in Figure 3.12 consisting of four streetlights in the upper part and one parked car in the lower part has been replicated in the East-axis to cover the complete trajectory, as shown in Figure 3.13.

Figure 3.17(a) shows the norm of the magnetic field measured over time during the experiment. If the magnetic field was homogeneous, its norm would be constant and equal to the field strength at the Equator, 25 µT.

Perturbations seen in Figure 3.17(a) are due to streetlights, mostly seen at 24 min and 35 min, and cars, mostly seen at 16 min and 32 min. The magnitude of the perturbations is not constant along the walk because the round trip estimated trajectory does not overlap due to positioning errors, as shown in Figure 3.13. Thus, the magnitude of the perturbations depends on the proximity of the pedestrian to the ferromagnetic object. Perturbations at 16 min correspond to the left ending part of the trajectory shown in Figure 3.13 that lies closer to the line of cars (blue points). The perturbations at 32 min correspond to the left ending part of the trajectory of Figure 3.13 situated in the middle of the previous one and the initial one. Notable perturbations due to streetlights (green points) are caused by the pedestrian walking not parallel to the line of streetlights, but crossing it, as shown in Figure 3.13.

Figure 3.14 shows that, without using the magnetic field, the bias of the z-axis cannot be estimated and Figure 3.17(b) shows that the use of the *Differential Magnetic Field Update* is beneficial to estimate the z-axis bias in perturbed magnetic fields, since the estimation tends to the correct value (see Table 3.1). However, if severe perturbations are used by this update, the z-axis bias estimation varies strongly to adapt the orientation estimation to the magnetic field distribution, as shown at 16 min, 24 min and 35 min, affecting also the x- and y-axis biases estimation.

Figure 3.17(c) shows the biases estimation by using the *Differential Magnetic Field Update* only when the *magnetic disturbances detector* activates it. The red curve of Figure 3.17(a) shows the periods where the update is activated. This analysis assesses that it is convenient to use a *magnetic disturbances detector*, that results in a smoother z-axis bias estimation. However, the biases estimation describes an oscillation that does not

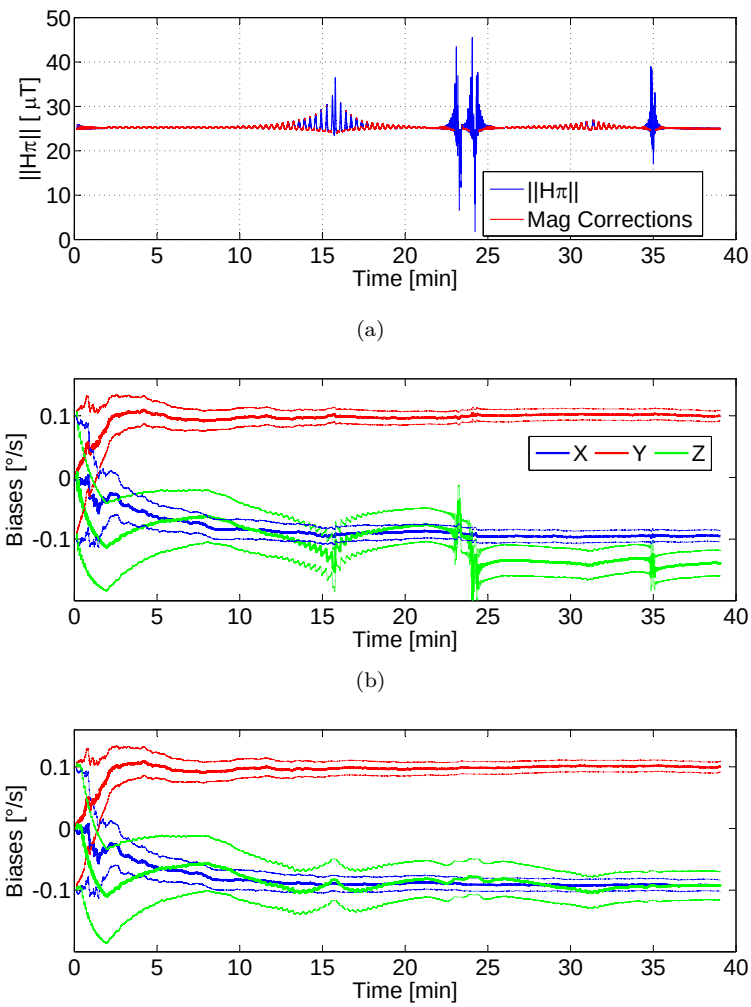

Figure 3.17: Biases estimation over time considering the perturbed magnetic field $\boldsymbol{H_\pi}$. (a) shows in blue the norm of the magnetic field and in red the periods where the *Differential Magnetic Field Update* is applied, (b) depicts the biases estimation using the *Absolute Gravity Update* and *Differential Magnetic Field Update* continuously and (c) shows the biases estimation using the *Absolute Gravity Update* and *Differential Magnetic Field Update* only when the *magnetic disturbances detector* activates it.

correspond to the artificially introduced value, which is constant. A possible solution is using a more restrictive *magnetic disturbances detector*. If the detector is more restrictive, the *Differential Magnetic Field Update* is applied less time, therefore, the estimation is smoother, but it needs more time to converge to the true bias value.

Effect of the Calibration of the Magnetometer The calibration of the magnetometer is of crucial importance in order to correct instrumentation errors and magnetic deviations, i.e. soft and hard iron effects due to the host platform [67]. The *Differential Magnetic Field Update* requires all magnetic measurements to be previously calibrated. In this analysis, the effect on the biases estimation of applying the *Differential Magnetic Field Update* without having calibrated the magnetometer will be shown.

In order to calibrate the magnetometer, the sensor has to be manually moved describing

random paths covering all directions. The recorded raw magnetic field measurements form a shifted ellipsoid if the data is not calibrated. A least-squares algorithm is used to find the rotation ($\boldsymbol{M}$), translation ($\boldsymbol{l}$) and scaling factor ($\boldsymbol{\xi}$) to bring the ellipsoid to a sphere with radius equal to 1 centered in the origin. The center of the sphere represents the biases of the three-axis magnetometer. The radius of the sphere is used to normalize the uncalibrated magnetic measurements to the local magnetic field intensity. The calibration process should take place in a disturbances-free environment, i.e. under a homogeneous magnetic field.

For this experiment, the homogeneous magnetic field of the city of Munich (see Table 3.1) is used. Calibration parameters are artificially introduced that make the generated magnetic measurements being uncalibrated, as they are expected to be if measured directly with a magnetometer. Table 3.3 summarizes the introduced calibration parameters:

Table 3.3: Calibration Parameters for the Generated Magnetic Measurements

$\boldsymbol{\xi}$	$\boldsymbol{l}$	$\boldsymbol{M}$
0.9472	$\begin{pmatrix} -0.0860 \\ -0.0871 \\ -0.1537 \end{pmatrix}$	$\begin{pmatrix} 0.9958 & 0.0017 & -0.0006 \\ 0.0017 & 0.9992 & -0.007 \\ -0.0006 & -0.0007 & 1.0050 \end{pmatrix}$

Figure 3.18(a) shows the norm of the homogeneous magnetic field of the city of Munich as directly obtained with the quasi-error-free turn rate measurements of the walk shown in Figure 3.13. As expected, the magnetic measurements are calibrated, since the norm of the magnetic field is constant during the complete trajectory. The blue curve shows the norm of the homogeneous magnetic field of Munich during the walk and the red curve shows the periods where the *Differential Magnetic Field Update* is activated by the *magnetic disturbances detector*. As the figure shows, the blue curve is completely overlapped by the red curve, thus the correction is continuously applied.

Figure 3.18(b) shows the same data, but applying the calibration parameters summarized in Table 3.3 in order to uncalibrate the generated magnetic field measurements. Figures 3.18(a) and (b) have the same span on the y-axis. The blue curve represents the norm of the three-axis magnetic field and the red curve represents the periods where the *Differential Magnetic Field Update* is applied. The magnitude of the distortions shown in the uncalibrated measurements is small compared with the magnitude of the distortions caused by ferromagnetic objects or electric currents (see Figure 3.17(a)), therefore the *magnetic disturbances detector* allows magnetic corrections to be continuously applied, so the blue curve is completely overlapped by the red curve.

Figure 3.18(c) shows the biases estimation process over time using uncalibrated magnetic field measurements whose norm is represented in Figure 3.18(b). The estimation of x- and y-biases is not significantly modified between using calibrated and uncalibrated magnetic field measurements. Their estimated values coincide with the artificially introduced

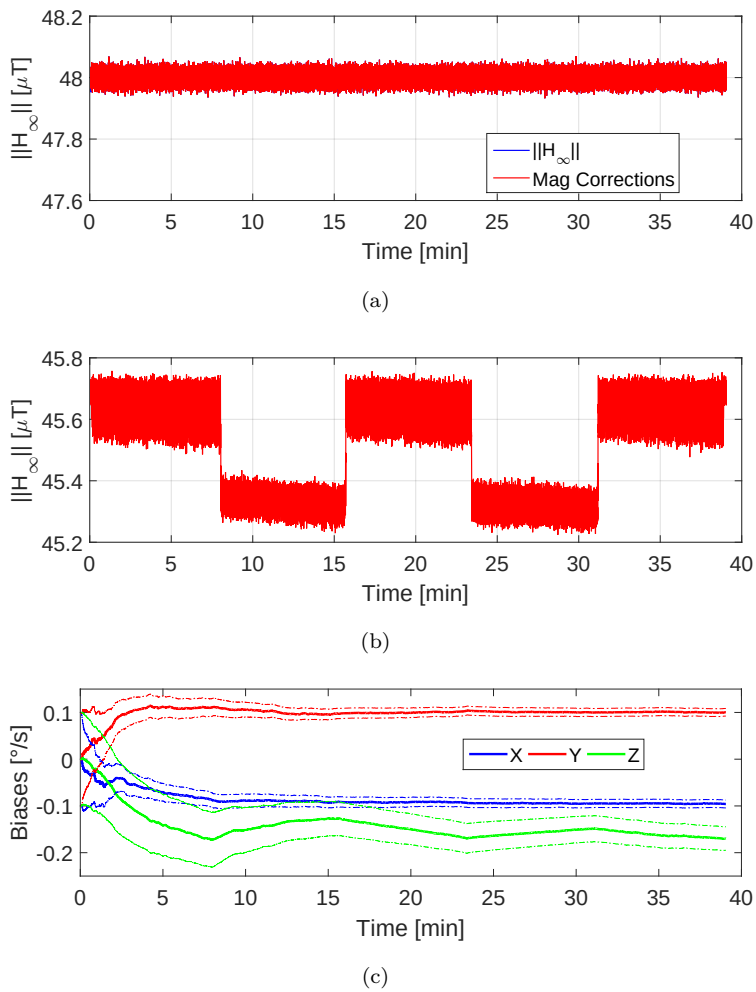

Figure 3.18: Biases estimation over time considering the homogeneous magnetic field $\boldsymbol{H_\infty}$ of the city of Munich. (a) shows in blue the norm of the magnetic field and in red the periods where the *Differential Magnetic Field Update* is applied, (b) shows the same data, but being uncalibrated by applying the parameters summarized in Table 3.3 and (c) depicts the biases estimation using uncalibrated magnetic field measurements and the *Absolute Gravity Update* and *Differential Magnetic Field Update* when the *magnetic disturbances detector* activates it.

values summarized in Table 3.2. However, the z-bias estimation is highly modified from the one obtained using calibrated magnetic field measurements shown in Figure 3.15(c). Although the experiment has been recorded under a homogeneous magnetic field, the fact of using uncalibrated magnetic measurements damages enormously the z-bias estimation process, as clearly seen in the figure. The estimated z-bias value oscillates around $-0.17\,^\circ\,\mathrm{s}^{-1}$, when the artificially introduced value corresponds to a constant value of $-0.1\,^\circ\,\mathrm{s}^{-1}$.

3.4.4.2 Evaluation with Medium-Cost MEMS Measurements

While the previous experiments used generated magnetic field measurements from reference turn rate measurements recorded with the IMU DSP-1750, the real Earth magnetic field will be measured in the following experiment with the aim of endorsing the previous

results. To that end, a new walk has been recorded in the city of Munich with the magnetic and inertial medium-cost MEMS sensor MTw. The trajectory corresponding to the walk is highlighted in yellow in Figure 3.19 and consists of a round trip trajectory of 290 m section length repeated 12 times resulting in a 3.5 km trajectory covered in approximately 44 min. The yellow pin represents the initial and final point of the walk.

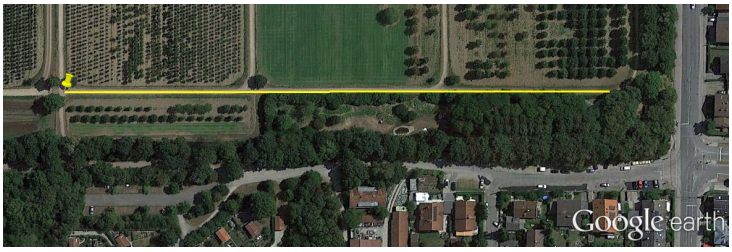

Figure 3.19: Disturbances-free scenario where the experiment of this section has been recorded. The initial and final point is highlighted with the yellow pin and the round trip trajectory is marked in yellow. The total length of the walk is 3.5 km over an elapsed time of 44 min.

The experiment has been recorded in a disturbances-free environment and the magnetometers have been previously calibrated in the same environment before starting the walk. Figure 3.20 shows the recorded cloud of points formed by the uncalibrated raw measurements and the resulting sphere fitted through least-squares that derived the calibration parameters summarized in Table 3.4.

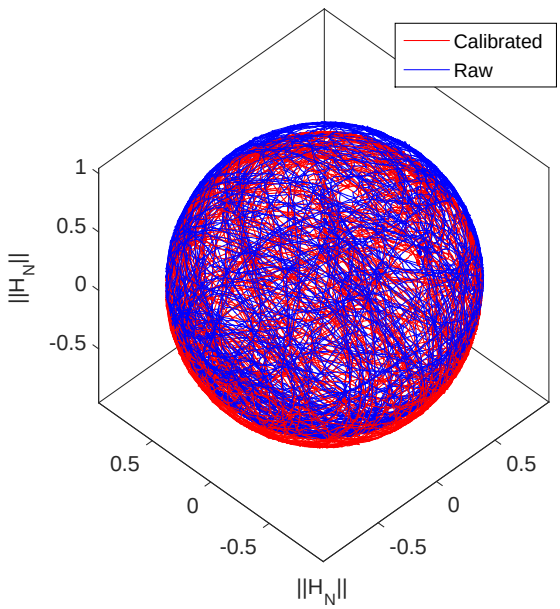

Figure 3.20: The blue points represent the raw uncalibrated data recorded in a disturbances-free environment with the sensor describing random paths covering all directions. The red points represent the least-squares fitted sphere that yields to the calibration parameters summarized in Table 3.4.

Figure 3.21 shows the norm of the magnetic field measurements recorded with the magnetometer embedded in the MTw sensor. The red curve in Figure 3.21(a) shows the norm of the raw uncalibrated magnetic field measurements and the red curve of Figure 3.21(b) shows the norm of the magnetic field measurements by previously applying the calibra-

Table 3.4: Calibration Parameters for the Xsens Magnetometer Sensor

ξ	l	M
0.9539	$\begin{pmatrix} 0.0031 \\ 0.0092 \\ -0.0881 \end{pmatrix}$	$\begin{pmatrix} 0.9941 & 0.0016 & -0.0015 \\ 0.0016 & 1.0029 & -0.0018 \\ -0.0015 & -0.0018 & 1.0030 \end{pmatrix}$

tion with the parameters summarized in Table 3.4. The results of the calibration of real medium-cost magnetometers shown in this figure correspond to the effects on the norm of the emulated magnetic field measurements previously shown in Figure 3.18(a) and (b).

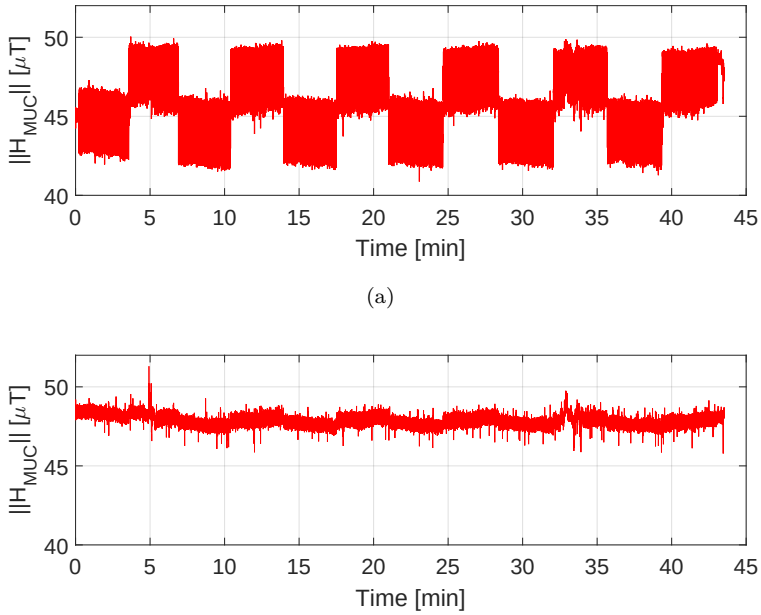

Figure 3.21: The red curve represents the norm of the magnetic field measurements recorded during the walk using the magnetometer embedded in the MTw sensor. (a) shows the raw uncalibrated magnetic measurements and (b) shows the same measurements after applying the calibration parameters summarized in Table 3.4.

The accurate value of the biases is unknown by directly using MEMS gyroscopes. Therefore, the MTw sensor has been placed on the floor between 1.5 min and 2 min at the beginning and at the end of the walk. The averaged value of the initial and final static turn rate measurements are assumed to correspond to the biases of the gyroscope, since no rotations were undergoing during these measurements. The Earth turn rate is disregarded due to its small value and the bias stability is much greater than 2 min. The observed biases value for each axis evolves over time, thus the initial and final value does not have to be the same. Table 3.5 shows the measured biases.

Figure 3.22(a) shows the biases estimation process without using magnetic field measurements, thus applying only the *Absolute Gravity Update*. It is clearly seen that the biases corresponding to the x- and y-axis are correctly estimated, since their values match the previously computed values summarized in Table 3.5. The z-axis bias is influenced

Table 3.5: Measured Biases, in $^\circ\,\mathrm{s}^{-1}$, for the Xsens Gyroscopes

	x-axis	y-axis	z-axis
Start	-0.12	0.12	-0.12
End	-0.13	0.05	-0.22

by the applied updates, however, it does not converge to the value shown in Table 3.5. Its associated uncertainty, represented with the dotted green lines, does not decrease over time, which is an indicator that the orientation filter is not able to observe this bias. These results fully correspond to the analysis and the results shown in Figure 3.14.

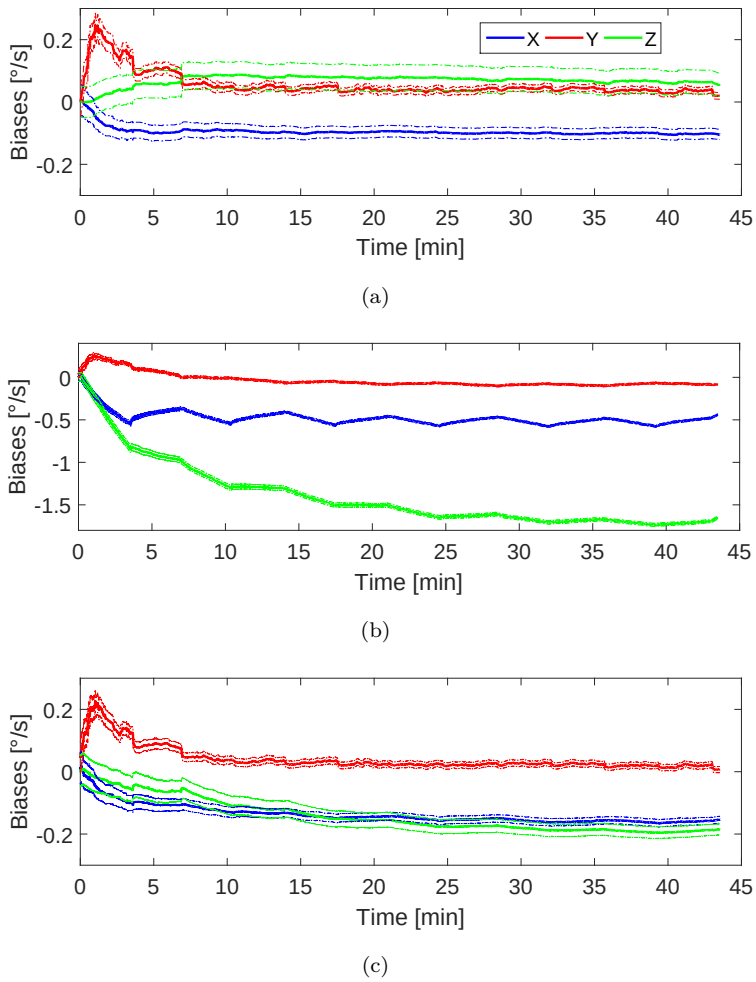

Figure 3.22: Biases estimation over time considering the real magnetic field $\boldsymbol{H}_{\mathrm{MUC}}$ of the city of Munich. The curves in (a) have been computed without using magnetic field measurements, only applying the *Absolute Gravity Update*. (b) shows the biases estimation applying the *Absolute Gravity Update* and the *Differential Magnetic Field Update* continuously by using the uncalibrated raw magnetic measurements whose norm is shown in Figure 3.21(a). Finally (c) shows the same curve as before, but using the calibrated magnetic measurements whose norm is shown in Figure 3.21(b).

Figure 3.22(b) shows the biases estimation process applying the *Absolute Gravity Update* and the *Differential Magnetic Field Update* continuously by using the uncalibrated raw magnetic measurements. The results match the previously analyzed walk shown in Figure 3.18(c). The estimated z-axis bias is over estimated by reaching a value of almost

$-1.7\,^\circ\,\mathrm{s}^{-1}$, being the theoretical value $-0.22\,^\circ\,\mathrm{s}^{-1}$ at the end of the walk. These values are so distant, that the x-axis bias is also negatively affected by the magnetic field measurements, causing an oscillation around $-0.5\,^\circ\,\mathrm{s}^{-1}$ where it should be almost constant at $-0.12\,^\circ\,\mathrm{s}^{-1}$. This experiment proves the importance of calibrating the magnetometer sensor before applying any magnetic correction even under homogeneous magnetic fields.

Figure 3.22(c) shows the biases estimation process applying the *Absolute Gravity Update* and the *Differential Magnetic Field Update* continuously. For this experiment, the magnetometer has been previously calibrated with the parameters summarized in Table 3.4. The figure shows how the bias corresponding to the z-axis is slowly estimated in the right direction without damaging the x- and y-axis biases. The results shown in this figure endorse the analysis shown in Figure 3.15 for the emulated homogeneous magnetic field measurements for different locations on the Earth. However, it is important to note that even under homogeneous magnetic fields, that means applying the *Differential Magnetic Field Update* continuously, the theoretical z-bias value in Figure 3.22(c) has not been reached after 44 min.

Therefore, successful z-bias estimation for the most common scenarios for pedestrian navigation, i.e. indoors and urban, is difficult to reach by only using the analyzed *Differential Magnetic Field Update*, due to the non-homogeneous nature of the magnetic field in these scenarios.

3.4.5 Effect of the z-Axis Gyroscope's Bias on the Yaw Angle

The previous analyses assess that the *Differential Magnetic Field Update* is capable of using magnetic field measurements to help estimating the z-axis bias of the gyroscope under different magnetic field distributions. The effect of the z-axis bias on the yaw angle is evaluated in the following, since the correct estimation of the z-bias should decrease the ever growing yaw angle error shown in Figure 3.10(c).

Figure 3.23(a) shows the yaw angle error under the homogeneous magnetic field of the Equator location. As clearly seen in Figure 3.15(b), the z-axis bias estimation is rapidly approaching the artificially introduced bias value $-0.1\,^\circ\,\mathrm{s}^{-1}$. Therefore, as expected, the yaw error does not grow without bounds and is stable over time after 10 min, as previously analyzed in the Figure 3.15(b). The error after 10 min does not decrease until 0°, because the z-bias estimation does not reach the reference bias value $-0.1\,^\circ\,\mathrm{s}^{-1}$ and additionally the biases of the FOG have not been considered.

Figure 3.23(b) shows the yaw angle error under the homogeneous magnetic field corresponding to the city of Munich. As Figure 3.15(c) shows, the z-axis bias estimation is not stable within the first 15 min, therefore the yaw angle error has the same behaviour. It is remarkable that the z-axis bias estimation is not smoothly approaching the reference value $-0.1\,^\circ\,\mathrm{s}^{-1}$, thus the yaw angle error is rapidly increasing and decreasing at the beginning.

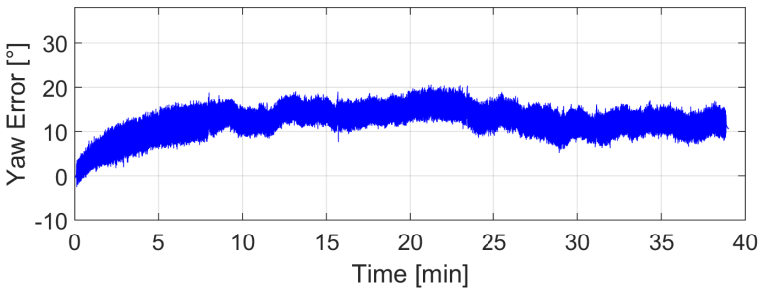

(a) $\boldsymbol{H_\infty}$ of the Equator

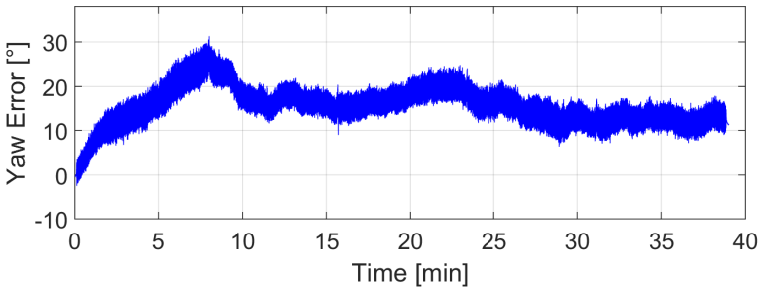

(b) $\boldsymbol{H_\infty}$ of the city of Munich

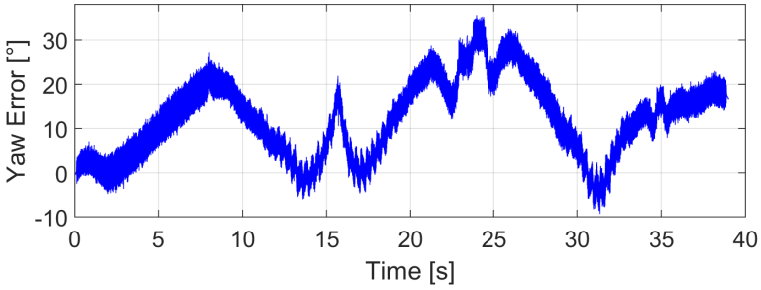

(c) $\boldsymbol{H_\pi}$ using the *magnetic disturbances detector*

Figure 3.23: The blue lines represent the error in the yaw angle for the magnetic scenarios, whose biases estimation have been previously shown in Figures 3.15(b), 3.15(c) and 3.17(c) respectively.

Finally, Figure 3.23(c) shows the yaw angle error for a perturbed magnetic field. The *Differential Magnetic Field Update* has been activated by the *magnetic disturbances detector*. This case is the most similar to a real scenario, because it is not common to find homogeneous magnetic fields, especially for indoors and urban scenarios. For this section, the orientation estimation filter settings are constant, therefore the *Differential Magnetic Field Update* has been applied with the same measurement noise values for homogeneous and perturbed magnetic fields for the measurements recorded with the IMU DSP-1750. Figure 3.17(c) shows that the effect of the perturbations caused by streetlights and cars are visible in the biases estimation and therefore also in the yaw angle, as Figure 3.23(c) shows. However, the *Differential Magnetic Field Update* is beneficial, since it causes the z-bias estimation to approach to the reference value $-0.1\,^\circ\,\mathrm{s}^{-1}$. Therefore, it is convenient to implement a more restrictive *magnetic disturbances detector* that activates less time the magnetic update. However, a more restrictive detector implies that the z-axis bias spends more time to approach the reference bias value. In this case, the z-bias needed

32 min to approach the correct value, then the *Differential Magnetic Field Update* effect would not be visible for short walks.

3.5 Discussion

This chapter presents a comprehensive analysis of the proposed orientation estimation filter for an inertial pedestrian navigation system. First, the Euler angles estimated with medium-cost MEMS inertial sensors have been compared to the angles estimated with quasi-error-free measurements. Roll and pitch angles present a limited error due to the fact that rotations around x- and y-axis are observable through the gravity field. However, the yaw angle describes rotations around the axis parallel to the gravity field, thus its changes cannot be observed and the error in the yaw angle grows rapidly over time.

An evaluation is driven that fills the gap in the literature on the analysis of the usability of the magnetic field for the estimation of the biases of MEMS gyroscopes. First, quasi-error-free turn rate measurements have been used to generate different magnetic field distributions and the analysis has been then endorsed with real medium-cost MEMS measurements. The results show that the biases estimation without using magnetic field measurements is possible for the x- and y-axis, however the z-bias remains unobservable only using the gravity field while walking or standing. Furthermore, different locations on the Earth, i.e. North Pole, Equator and Munich are evaluated with homogeneous magnetic fields. It is concluded that, thanks to the movement of the leg of the pedestrian while walking, it is possible to correctly estimate the z-bias even in the less favorable location, however the magnetic field distribution influences the time needed to reach the correct value. Additionally, it is possible to obtain correct estimations of the biases under magnetically perturbed environments. However, it is convenient to use a disturbances detector that selects constant or quasi-constant magnetic field periods rather than using perturbed magnetic measurements continuously.

The effects of using uncalibrated magnetic field measurements, even under homogeneous magnetic fields, are shown in this chapter. Measurements recorded by medium-cost MEMS sensors are analyzed yielding to the conclusion that magnetic measurements help estimating the biases of the gyroscope, however, due to the non-homogeneous nature of the magnetic field in indoor and urban scenarios, the estimation process is prohibitively slow. Finally, the effect of the z-axis bias estimation on the yaw angle is evaluated. The results show that successful estimations of the bias on the z-axis yield to limited errors on the yaw angle.

Chapter 4

Displacement Estimation

Nothing in life is to be feared, it is only to be understood.

Marie Curie

The displacement estimator is a group of algorithms that receive from the orientation estimator the pitch angle and delivers stepwise the horizontal and vertical displacement of the pedestrian. Therefore a step detector, a step length estimator and a vertical displacement estimator are needed. The step detector and step length estimator algorithms proposed in this thesis outperform the state of the art algorithms by offering a lower false step detection rate and more accuracy in the step length at different walking speeds. The presented vertical displacement estimator allows for the first time to solve 3D positioning using only inertial measurements with the step-and-heading approach.

4.1 Step Detection

This section details the proposed step detector based on the pitch angle, which is broaden out to 3D scenarios adding a great value to the state of the art. Stairs constitute a challenging scenario where the step detectors already proposed in the literature face difficulties.

4.1.1 Horizontal Surfaces

If the sensor is attached to the upper part of the leg of the pedestrian, e.g. placed in the pocket of the trousers, the estimated pitch angle describes the opening angle of the leg of the pedestrian. Figure 4.1(b) shows the estimation of the pitch angle during a walk for seven steps. The maximum elongation of the leg, when the foot is still on the air, is indicated as θ_{Hmax} and the second positive peak occurs as a consequence of the foot hitting the floor. The lowest negative angle is indicated as θ_{Hmin}. Figure 4.1(a) shows

that θ_{Hmax} is much larger than θ_{Hmin}. The reason for this difference is that the pedestrian bends the knee of the rear leg considerably when walking.

The vertical dashed line represents a pitch angle equal to zero. Therefore, if the pedestrian is standing, the legs are closed and the pitch angle is zero.

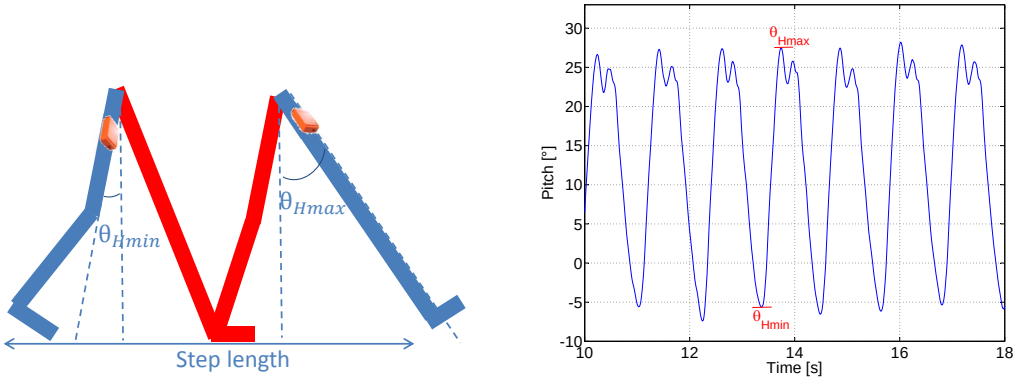

(a) Representation of the legs during a step. A step is completed every time the leg which has the sensor, in this case the blue one, hits the floor.

(b) The blue curve represents the pitch angle estimation during a walk. In this figure, seven steps are highlighted.

Figure 4.1: Diagram of the position of the legs while walking and estimated curve of the pitch angle.

The amplitude of the opening angle of the leg or pitch amplitude is defined as

$$\Delta\theta_{\text{H}} = \theta_{\text{Hmax}} - \theta_{\text{Hmin}}. \tag{4.1}$$

The step detector proposed in this thesis consists of the identification of the maximum pitch angle, indicated in the Figure 4.1 for one step as θ_{Hmax}. Each repetition of the shape of the pitch angle estimation corresponds to one step. As the figure shows, the pitch angle is optimal for detecting steps due to its cyclic nature, because the maximum or the minimum are given only once per step. Unlike the literature algorithms using acceleration measurements, no varying thresholds depending on the walking speed or post-processing is needed.

4.1.2 Stairs

The detection of steps is extended from walking on horizontal surfaces towards walking on stairs. The step detection when walking on stairs is explained by studying of the position and movement of the legs when walking up- and downstairs.

Figure 4.2(a) represents a diagram of the position of the legs while walking upstairs. Figure 4.2(b) shows the pitch angle estimation corresponding to eight steps, the first two occurred walking on the landing zone of the staircase and the following five going upstairs.

It is noticeable that θ_{Umax} is almost doubled compared to θ_{Hmax}. This is caused by the pedestrian raising the leg in order to reach the following step up of the stairs. In addition, $|\theta_{\text{Umin}}|$ is slightly smaller than θ_{Hmin}. It is convenient to use the absolute value because,

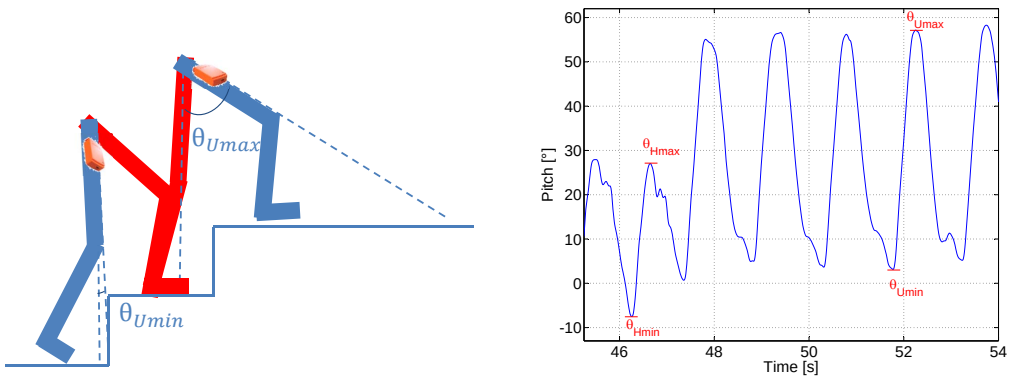

(a) Position of the legs while walking upstairs.

(b) Pitch angle estimation walking upstairs.

Figure 4.2: Figure 4.2(a) represents the diagram of the position of the legs while walking upstairs. Figure 4.2(b) shows the pitch angle estimation corresponding to eight steps, the first two the pedestrian walks on the landing zone of the staircase and the last five the pedestrian walks upstairs.

depending on the height of the step of the stairs, way of walking of each pedestrian, tiredness, hurry, etc. θ_{Umin} oscillates around 0°, i.e. it can be slightly positive or slightly negative. Additionally, it is observable that the pitch amplitude by walking upstairs $\Delta\theta_{\mathrm{U}}$ is notably larger than $\Delta\theta_{\mathrm{H}}$. The double maximum peak does not occur, but in contrast a double minimum peak appears.

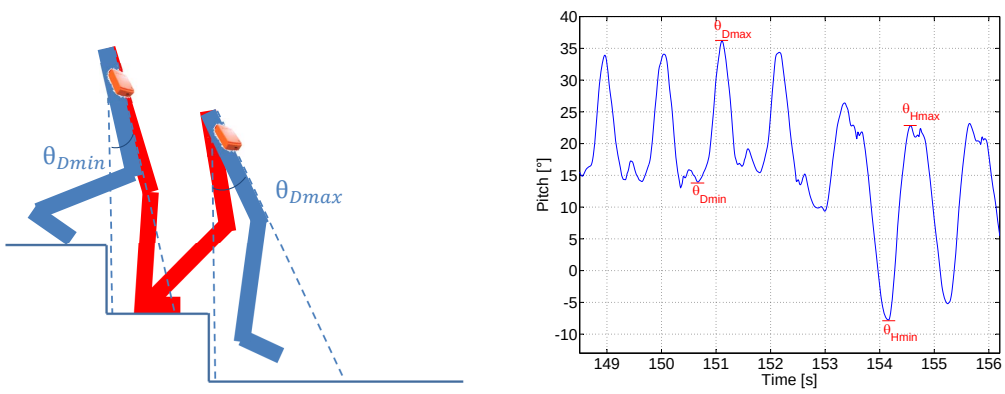

(a) Position of the legs walking downstairs.

(b) Pitch angle estimation walking downstairs.

Figure 4.3: Figure 4.3(a) represents the diagram of the position of the legs while walking downstairs. Figure 4.3(b) shows the pitch angle estimation corresponding to seven steps, the first four the pedestrian walks downstairs and the last three the pedestrian walks on the landing zone of the staircase.

Figure 4.3(a) represents a diagram of the position of the legs while walking downstairs. Figure 4.3(b) shows the pitch angle estimation corresponding to seven steps, the first four occurred going downstairs and the following three walking on the landing zone of the staircase.

It is noticeable that θ_{Dmin} has a positive value in contrast to θ_{Hmin}. This is caused by the pedestrian moving the leg in order to reach the following step down of the stairs. In addition, θ_{Dmax} is slightly larger than θ_{Hmax}. Additionally, it is observable that the pitch amplitude by walking downstairs $\Delta\theta_{\mathrm{D}}$ is notably smaller than $\Delta\theta_{\mathrm{H}}$. The double

maximum peak does not occur, but in contrast a double minimum peak appears.

The step detector proposed, as previously explained, consists of the identification of the maximum of the pitch angle because each maximum indicated as θ_{Umax} or θ_{Dmax} corresponds to a single step. Therefore, the pitch angle is adequate as well for detecting steps up and down in stairs.

4.1.3 Physical Activities Identification

In the following, the identification of different physical activities, particularly standing, walking, walking upstairs, walking downstairs and sitting by means of the pitch angle estimation is presented.

Figure 4.4 shows the pitch angle estimation during a 3D walk. In this walk, four physical activities can be clearly identifiable. Periods of standing are highlighted under the cyan line, walking is indicated by the red line, walking upstairs is indicated by the green line and lastly walking downstairs is indicated by the blue line. In this walk, the pedestrian started standing and then walked through the corridor to the stairs. The pedestrian walked up until the second floor of the building and then walked until the end of the corridor and came back to the staircase. Lastly, the pedestrian descended again to the ground floor and walked back to the starting point.

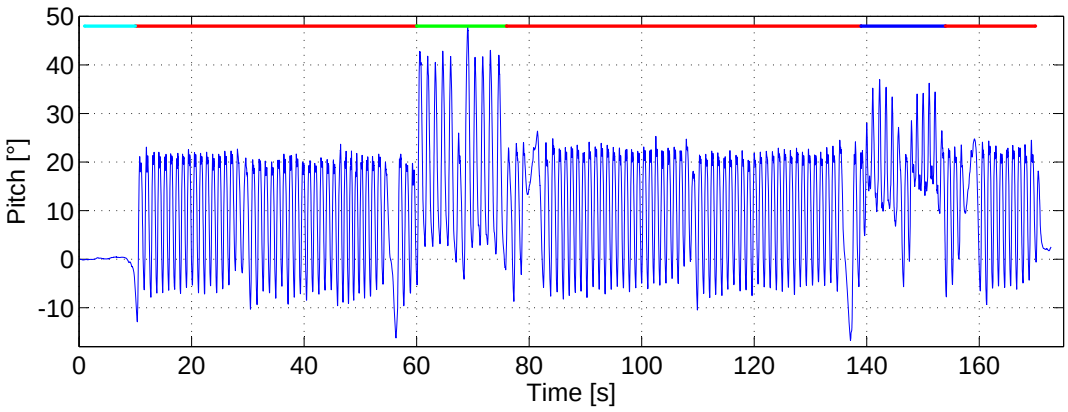

Figure 4.4: The blue curve represents the estimation of the pitch angle over time, measured in degrees, during a multi-storey walk with the sensor in the pocket.

It is clear in Figure 4.4, that the detection of different physical activities can be performed by simply tracking changes on the pitch angle estimation. The algorithm for distinguishing walking on a horizontal surface, walking upstairs and walking downstairs proposed in this thesis is based on three parameters of the pitch angle estimation: θ_{min}, θ_{max} and $\Delta\theta$.

The parameters θ_{Hmin}, θ_{Hmax} and $\Delta\theta_{\mathrm{H}}$ are learned during the walk under the assumption that the pedestrian starts walking on an horizontal surface. Therefore, these values are personalized for an optimal performance and continuously adapted to the pedestrian's

mood, hurry, tiredness, etc. In order to determine if the pedestrian is walking upstairs, downstairs or horizontally, the parameters θ_{min}, θ_{max} and $\Delta\theta$ are stepwise extracted and compared to the reference parameters $\overline{\theta_{\text{Hmin}}}$, $\overline{\theta_{\text{Hmax}}}$ and $\overline{\Delta\theta_{\text{H}}}$, which are the result of averaging the last horizontal steps:

if $\Delta\theta \gg \overline{\Delta\theta_H}$ && $\theta_{max} \gg \overline{\theta_{Hmax}}$ **then**
  $\theta_{\text{Umax}} = \theta_{\text{max}}$; $\theta_{\text{Umin}} = \theta_{\text{min}}$; $\Delta\theta_{\text{U}} = \Delta\theta$;
end
else if $\Delta\theta \ll \overline{\Delta\theta_H}$ && $\theta_{min} \gg \overline{\theta_{Hmin}}$ **then**
  $\theta_{\text{Dmax}} = \theta_{\text{max}}$; $\theta_{\text{Dmin}} = \theta_{\text{min}}$; $\Delta\theta_{\text{D}} = \Delta\theta$;
end
else
  $\theta_{\text{Hmax}} = \theta_{\text{max}}$; $\theta_{\text{Hmin}} = \theta_{\text{min}}$; $\Delta\theta_{\text{H}} = \Delta\theta$;
end

The thresholds needed in order to determine if the pedestrian is walking upstairs or downstairs can be universal or personalized. The more accurate option is to calibrate the system to correctly select them adapted to each pedestrian.

Regarding the standing and sitting activities, their main characteristic is the value of the pitch, which is almost constant. The pitch value lies around 0° when the pedestrian is standing and around 45° and 90° if the pedestrian is sitting. Figure 4.5 shows the pitch estimation of a pedestrian doing the following activities: standing, walking, sitting, walking and standing. Standing is highlighted under the cyan line, walking is indicated by the red line and sitting is indicated by the green line.

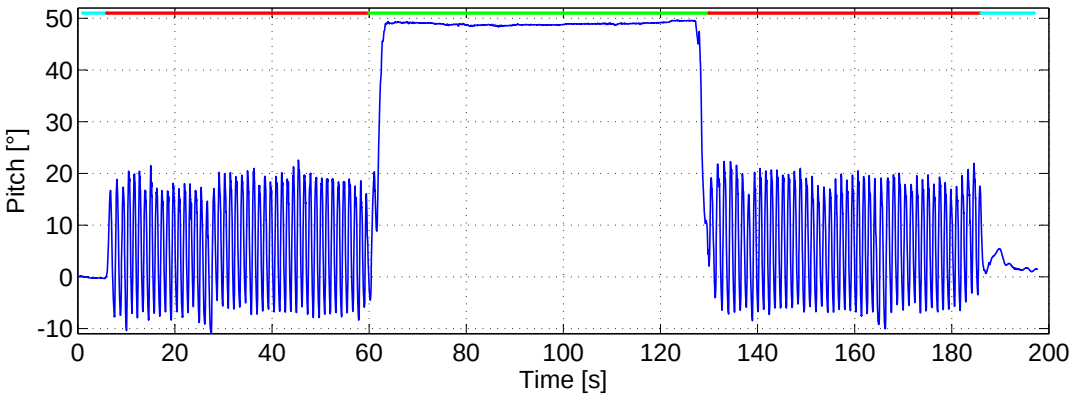

Figure 4.5: Pitch angle estimation of a walk including standing, walking and sitting.

The activities standing and sitting are only checked when no steps are detected. Then the distinction between them only depends on the value of the pitch angle. The identification of the physical activity distinguishes if the step taken was on an horizontal surface, was a step up or a step down. This distinction is of high interest for aiding the navigation being the basis of the proposed vertical displacement estimator. Furthermore, some ap-

plications such as monitoring patients in hospitals or elderly care usually need the fusion of navigation and identification of physical activities.

4.1.4 Experimental Results

The proposed step detector algorithm has been tested on horizontal surfaces and on staircases, since the displacement estimator delivers both, horizontal and vertical displacement. To assess its performance, four different scenarios have been chosen. The scenario H1 describes a rectangle of 100×80 meters walking at a constant comfortable speed of $3.5\,\mathrm{km\,h^{-1}}$. For the scenario H2, the pedestrian walks the long rectangle side at a slow speed and the short side at a speed of $4.8\,\mathrm{km\,h^{-1}}$. The goal of scenarios UP and DW is to test the detection of steps up and down in stairs, walking at a constant and comfortable speed. After walking 40 m on a horizontal surface, the pedestrian enters the staircase and walks four floors up and then down. Finally, after leaving the staircase zone, the pedestrian walks back through the horizontal surface to the starting point.

The step detection algorithms under study are based on the norm of the three-axis acceleration and its low-pass filtered version. The complete acceleration instead of the vertical acceleration is used to be robust to different sensor orientations. A low-pass filter of 15 samples has been applied to the norm of the acceleration measurements to detect steps with the second proposed algorithm. Regarding the pitch angle estimation both algorithms are studied, the zero-crossing detection and the maximum detection. The detection thresholds are adapted to a comfortable walking speed and remain constant during the experiments, thus not adapted to different scenarios. The results are shown in Table 4.1 where both, the undetected steps (US) and the false detections (FD) are detailed.

Table 4.1: Performance Comparison of Different Step Detection Algorithms

	H1		H2		UP		DW	
	US [%]	FD [%]	US [%]	FD [%]	US [%]	FD [%]	US [%]	FD [%]
$\|\boldsymbol{\alpha}\|$	0.4	5	63	12	33	2.3	33	12
LPF $\|\boldsymbol{\alpha}\|$	0	0	65	3.6	36	0	23	0
Pitch z-c	0	0	0	0	0	0	38	1
Pitch m	0	0	0	0	0	0	0	0

The comparison between the aforementioned step detection algorithms is limited to the detection of steps, because it is not possible with the state of the art algorithms to distinguish between horizontal steps and steps up or down. The statistics summarized in Table 4.1 assess that it is possible to successfully detect steps at a constant and comfortable speed, as shown in scenario H1, through the different compared step detection algorithms. The low-pass filter smooths the signal, thus it contains less peaks that could yield false step detections. Therefore, it is recommendable to filter the norm of the acceleration to

avoid false detections. The smoothing is in all scenarios beneficial.

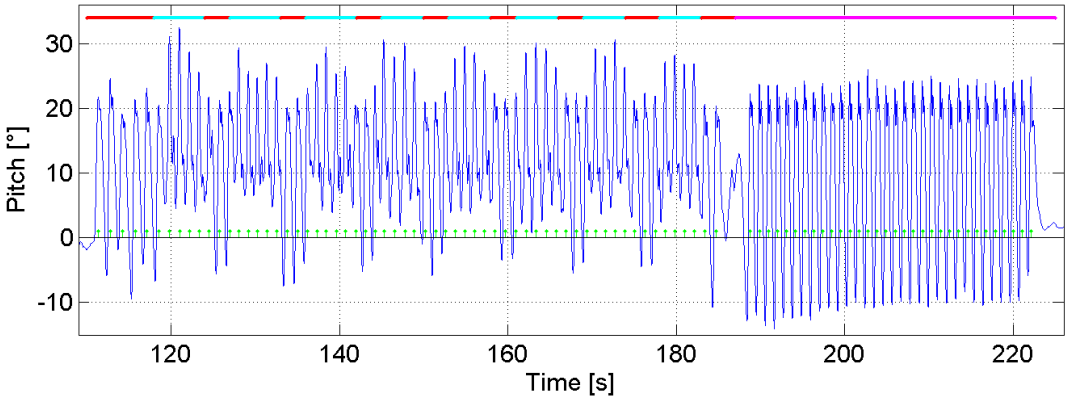

Figure 4.6: Pitch angle estimation of the scenario DW. The green dots represent the truth taken steps. The upper colored line maps different zones of the walk: red for the landing zone of the staircase, cyan for the stairs and magenta for the corridor, which is a horizontal surface.

Figure 4.6 shows the pitch angle estimation for the scenario DW. The green dots represent the true taken steps. The pedestrian starts walking on the landing zone of the stairs of the fourth floor. Then, the pedestrian walks downstairs to reach the ground floor. In the figure, the landing zones of the stairs are highlighted with a red line and the stairs are highlighted with a cyan line. Finally, the pedestrian walks approximately 40 m on an horizontal surface through the corridor, which is marked in the figure with a magenta line.

The zero-crossing-based pitch detector performance is similar to the proposed step detector, however it is not able to detect all steps in stairs because the zero-crossing does not occur, as shown in Figure 4.6 for the scenario DW. The zero-crossing for walking upstairs, however, depends on the pedestrian's mood, tiredness, etc. Therefore, the minimum of the pitch signal by walking upstairs can be slightly positive or slightly negative. For the scenario UP, the minimum pitch particularly for this pedestrian has a slightly negative value, thus the zero-crossing-based algorithm detects every step up.

As Figure 4.6 shows, the walking speed of the pedestrian is lower in the landing zones than in the corridor, therefore the pitch amplitude is smaller and the step duration lasts longer. The vast majority of steps taken in landing zones are not detectable with the acceleration-based algorithms. The same non-detection appears in scenario H2, where the pedestrian was asked to walk long rectangle side at a slow speed and the short side at a higher speed.

Pedestrians naturally adapt their walking speed and step length to the scenario or to their circumstances. Therefore, changes of speed during the same walk represent a realistic scenario. In order to avoid losing steps in such situations, a possible solution consists of using an adaptable threshold. Such an adaptable threshold, however, is not necessary for detections based on the pitch angle, which is one of the greatest advantages of the pitch-based step detection. The proposed step detector successfully detects every

step of the presented scenarios and does not incur on false detections that are likely to happen, for example when the pedestrian opens or closes doors, as Figure 4.6 shows at second 185.

4.1.5 Discussion

This section aims at offering an evaluation of the proposed step detector algorithm based on the pitch angle. Challenging scenarios have been analyzed, such as different walking speeds and 3D walks. The most common algorithms proposed in the state of the art have been implemented and tested under the same conditions in order to have a fair comparison. The results of the experiments let conclude that the proposed step detection algorithm based on the detection of the maximum of the pitch angle overcomes the state of the art algorithms under challenging scenarios in terms of undetected and false detected steps.

4.2 Step Length Estimation

The great part of the algorithms proposed in the state of the art for the estimation of the step length exploits the relationship between step length and step frequency or between step length and acceleration. In this thesis, the estimation based on the pitch angle is for the first time introduced.

The hypothesis investigated in this thesis is that, for the same pedestrian, every pitch angle, i.e. opening angle of the legs, corresponds to a different step length. Thus, an extensive set of experiments has been carried out in order to assess this hypothesis. These experiments will prove that the opening angle of the legs has a relationship with the step length. It has also been tested whether this relationship can be applied in general for all pedestrians or not and if different pedestrians provide similar results. Furthermore, the impact on the step length of other variables such as the height, weight, length of the leg and gender of the pedestrian among others are studied.

4.2.1 Experimental Set Up

The approach proposed in this thesis obtains the pitch angle from the orientation estimator. For this section, in order to have a quasi-error-free reference system, it has been decided to use a measurement system consisting of 16 infrared cameras located on the ceiling of a $18\,\mathrm{m}^2$ room. These cameras capture the position and the orientation of an object with sub-millimeter accuracy.

The infrared-based measurement system offers several advantages. On the one hand, the data for deriving the model will not contain any biases from medium-cost MEMS sensors or any error due to the processing with the presented orientation estimator. On

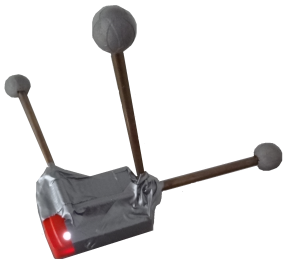

(a) Reflectors on the sensor to form a 3D object

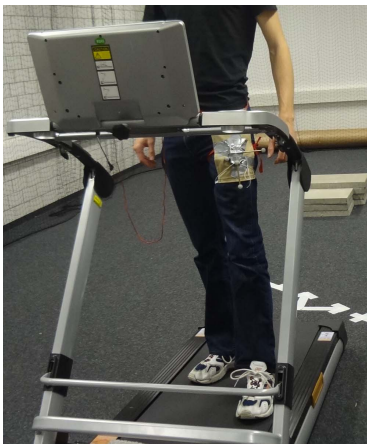

(b) External fabric pocket to hold the sensor

Figure 4.7: The 16 infrared cameras on the ceiling capture the movement of the three orthogonal reflectors while the pedestrian walks on the running machine. The sensor attached to the external fabric pocket reproduces the movement of the MEMS sensor inside the pocket of the pedestrian.

the other hand, due to the sub-millimeter accuracy of the measurement system both, step length and pitch angle will be considered for these experiments quasi-error-free.

A virtual 3D object has been created by sticking three reflectors to the sensor (see Figure 4.7(a)). Then, an external fabric pocket allocates the sensor at the normal pocket place without introducing it in the real pocket of the trousers, since this is not possible with the reflectors, as Figure 4.7 shows. The infrared-based measurement system tracks the movement of the 3D object created with the reflectors at 100 Hz rate and measures its position and orientation.

Since the room where the infrared-based measurement system has been installed is small for the purpose of this experiment, it has been decided to use a running machine, as Figure 4.7(b) shows. The running machine allows the pedestrian to go over long distances within the room. Additionally, the running machine offers the possibility of selecting a constant speed between a set of seven different speeds. In order to accurately know the walking speed, reflectors were put on the running machine to compute the quasi-error-free speed with the infrared-based measurement system. This experiment was done for all speeds with a volunteer on the running machine for taking into account the possible modification of the speed with the weight of a person. Table 4.2 shows the different running machine speeds and the processed speeds with the infrared-based measurement system.

The experiment has been conducted with 18 volunteers, eight women and ten men with ages between 22 and 57. First, they were asked to provide personal information such as gender, age and weight. Their height and pocket's height were measured taking into account the height of the sole of the shoes. They were asked to walk on the running machine and increase the speed every 3 min until 7 $\mathrm{km\,h^{-1}}$. For 1 $\mathrm{km\,h^{-1}}$ and 2 $\mathrm{km\,h^{-1}}$,

Table 4.2: Running Machine Nominal and Measured Speeds

Running machine speed [$\mathrm{km\,h^{-1}}$]	Nominal speed [$\mathrm{m\,s^{-1}}$]	Measured speed [$\mathrm{m\,s^{-1}}$]
1	0.2778	0.3025
2	0.5556	0.607
3	0.8333	0.9131
4	1.111	1.2132
5	1.3889	1.5002
6	1.6667	1.8122
7	1.9444	2.1244

volunteers did not feel comfortable on the running machine because of the extremely low speed. Therefore, these measurements have been discarded for the study. Likewise, the $7\,\mathrm{km\,h^{-1}}$ measurements have been also discarded for the analysis, because some volunteers started running and some kept walking.

In order to verify that the running machine does not introduce any anomaly in the way of walking, a subgroup of volunteers was selected to repeat the same experiment directly on the floor. For this second experiment, there was a real displacement of the pedestrian and the step length could be directly computed without the need of a predefined speed. For the step detection in both cases, with and without running machine, the step detector based on the maximum pitch angle proposed in this thesis has been used to identify steps.

4.2.2 Model Derivation

Position and orientation measurements corresponding to more than 15000 steps were recorded during the experiment. The data has been analyzed per volunteer yielding to the confirmation of the proposed hypothesis: there is a relationship between the opening angle of the legs and the step length. Figure 4.8 shows the results for one volunteer, where pitch amplitude is defined in Equation (4.1).

Each cloud of points represents a different speed and each point represents a step. This figure shows the clear trend of the data obtained. It indicates that the larger the pitch angle is the larger the step length will be. The figure also shows that the higher the walking speed is, the larger the step length is and, consequently, the larger the pitch angle will be. This can be noticed because the steps recorded at each speed are sorted increasingly.

Moreover, it has been confirmed that this relationship exists for all volunteers participating in the experiments. In Figure 4.9(a) the data for nine different volunteers has been depicted. Each color represents a different volunteer, within the color each cloud of points represents a speed and each point represents a step.

Figure 4.9(b) shows in dark blue the points of nine volunteers recorded with the running

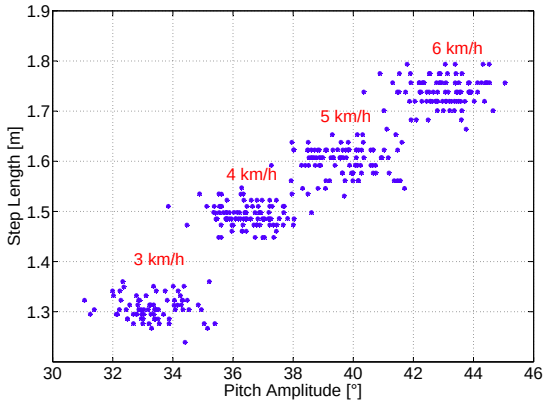

Figure 4.8: Every blue point represents the steps from the measurements gathered for one volunteer and each cloud of points represents a different speed. For every step, the pitch amplitude is plotted against the step length.

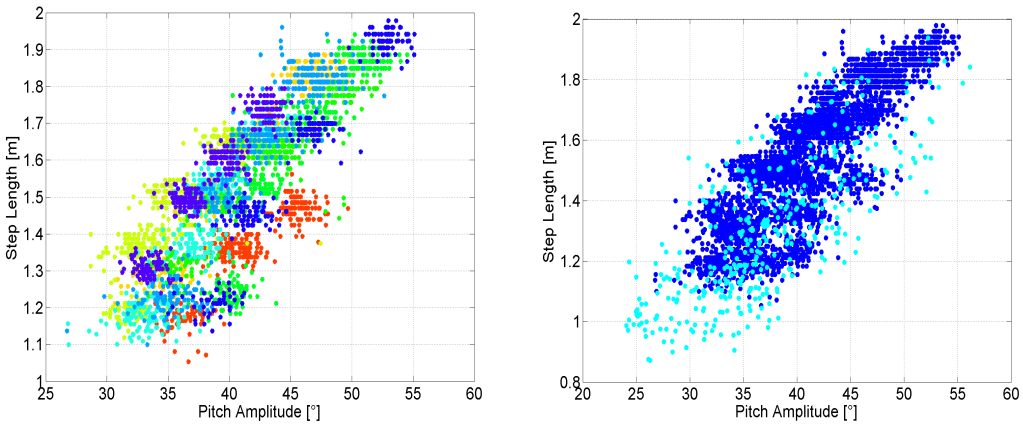

(a) (b)

Figure 4.9: Every blue point in Figure 4.9(a) represents one step from the measurements gathered for nine different volunteers and each color represents a volunteer. For every step, the pitch amplitude is plotted against the step length. The dark blue points represent the data recorded with the running machine and the light blue points were recorded walking directly on the floor.

machine (shown in Figure 4.9(a)) and in light blue the points of five selected volunteers walking directly on the floor. The results shown in this figure demonstrate that the data of pedestrians walking directly on the floor follows the same trend as the data of pedestrians walking on the running machine. Consequently, the running machine provides realistic results. More points can be observed in the lower part that correspond to lower speeds discarded for the running machine because the volunteers did not feel comfortable.

After the evaluation of the recorded measurements, it is rather hard to find a clear relationship between the personal parameters of the volunteers and their step length. The regression lines corresponding to each volunteer are not sorted by height, pocket's height or weight and they are not grouped by gender either. Even though from the logical point of view the height should have an impact on the step length, the way of walking of each pedestrian masks the personal parameters in a way that, makes it not possible to find any relationship.

Therefore, it has been decided to model the points obtained by each volunteer with a regression line. The linear regression is calculated with least-squares. The best fit in the least-squares sense minimizes the sum of squared residuals, being a residual the difference between the measured step length and the fitted value provided by the model, the estimated step length. Thus, the proposed model for the step length is as follows:

$$s = a_{\mathrm{H}} \cdot \Delta\theta_{\mathrm{H}} + b_{\mathrm{H}}, \tag{4.2}$$

where s is the estimated step length measured in meters taking into account the pitch amplitude in horizontal surfaces, $\Delta\theta_{\mathrm{H}}$, in degrees. The constants a_{H} and b_{H} correspond to the parameters fitting the regression line of each pedestrian.

As already assessed, a relationship between the pitch amplitude, $\Delta\theta$, and the step length, s, exists. Figure 4.8 shows the pitch amplitude against the step length for one volunteer. Figure 4.10 shows the recorded measurements of the pedestrian running from $8\,\mathrm{km\,h^{-1}}$ until $12\,\mathrm{km\,h^{-1}}$.

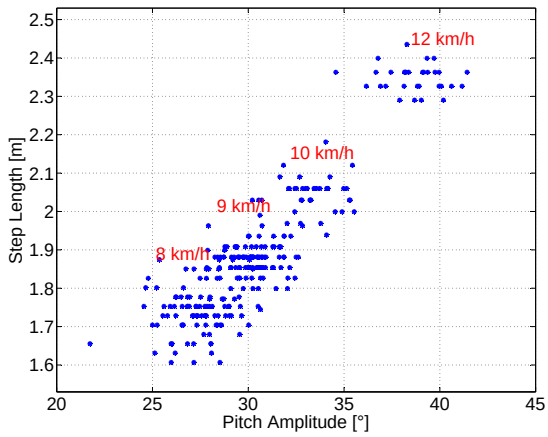

Figure 4.10: Every blue point represents the steps from the measurements gathered for one volunteer running and each cloud of points represents a different speed. For every step, the pitch amplitude is plotted against the step length.

The shape of the pitch angle estimation is the same walking and running as long as the surface is horizontal for both activities. Therefore, it was expected that by increasing the speed both, step length and pitch amplitude, also increase. However, the steps of Figure 4.8 and 4.10 together do not lie on a line. This is due to the running cycle, which has a stage when none of the feet touch the floor. The different gait cycle modifies the opening angle of the legs, thus, the pitch amplitude. In any case, Figure 4.8 and 4.10 show the same trend, thus the step length for running and walking can be modeled analogously. However, the running activity is out of the scope of this thesis, therefore from here on it will not be considered.

4.2.3 Model Calibration

Having the correct parameters a_{H} and b_{H} for each pedestrian is of crucial importance in terms of accuracy. Therefore, a calibration method is proposed. The regression lines of different volunteers show that the slope a_{H} is very similar among them. Figure 4.11 shows the regression lines in different colours of five volunteers who repeated the experiment without the running machine, walking directly on a horizontal floor.

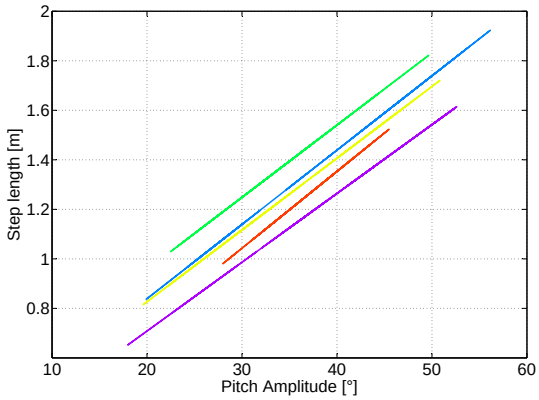

Figure 4.11: Regression lines corresponding to five volunteers walking at different speeds between $2.5\,\mathrm{km\,h^{-1}}$ and $6.5\,\mathrm{km\,h^{-1}}$.

The universal parameters are computed taking into account the complete set of steps of all volunteers. The universal regression line overlaps the yellow line of Figure 4.11. This figure gives an idea of the error in the estimated step length for each volunteer if the universal parameters are used. The error has a range from almost 0 cm per step for the volunteers whose regression line is represented in yellow and blue to almost 14 cm per step for the volunteers whose regression lines are represented in green and violet.

From the experiments, it could not be concluded which pedestrian characteristics influence a_{H} and b_{H}. Biomechanical studies show that at any given walking speed, it is possible to select different combinations of step frequency and step length. However, individuals tend to constantly choose a specific step length for each walking speed [68]. Optimizing energy costs primary determines the selection of a certain gait pattern. A possible explanation of the similar slopes $\mathrm{a_H}$ of the regression lines is that all volunteers choose their step length at each speed basically regulated by the minimization of energy costs, being this pattern is the same for all pedestrians. There are, however, other characteristics such as height, length of the legs, weight, gender, etc. that cause differences between pedestrians. This is a possible explanation of the different offsets b_{H}.

Based on the exposed results, a calibration method using the universal parameter $\mathrm{a_H}$ is suggested, that the pedestrian only has to walk a known distance at a comfortable speed to find the personalized parameter b_{H}. This simple and quick calibration which does not require additional infrastructure or additional pedestrian information such as height or length of the leg.

4.2.4 Experimental Results

The proposed step length estimator based on the pitch angle and its comparison to the well-known step length estimator based on the step frequency is analyzed. The evaluation takes into account different walking speeds. For evaluating the step length estimator, the volunteer whose data is shown in Figure 4.8 walked along a straight path of length 69 m, forth and back and repeated this path ten times. The volunteer changed the walking speed for the different realizations of the straight path between $3\,\mathrm{km\,h^{-1}}$ and $6\,\mathrm{km\,h^{-1}}$. Every time the volunteer turns 180° the walking speed decreases. The results are summarized in Table 4.3.

Table 4.3: Step Length Estimator Assessment

Estimated Distance [m]		Error [%]
Mean	Std. Dev.	Mean
69.1	1.09	0.15

For obtaining these results the model described in Equation 4.2 has been used. The parameters a_{H} and b_{H} are personalized parameters extracted from the measurements shown in Figure 4.8. No pre-calibration before this experiment has been carried out. These results show an excellent performance of the model of the step length based on the pitch angle with an estimated distance of mean 69.1 m, and a mean error of 0.15%. Ten realizations of the straight line of 69 m at different speeds have a standard deviation of 1 m, therefore the proposed model offers good results even when the user does not walk at a constant speed.

It is worth to mention that this experiment does not reflect the error in the individual step length estimation, but the error for the complete trajectory of 69 m. Small over- and underestimations of the individual step length estimations are compensated. However, this result is interesting because the sum of all steps is of major importance.

To fairly compare the step length model based on the step frequency with the step length model based on the pitch angle, its regression line has been extracted from the experiments recorded with the running machine previously described. Figure 4.12 shows the measurements for the volunteer whose data is shown in Figure 4.8 represented against the step frequency. The shape of the clouds of points of each walking speed results from the restriction of the constant speed imposed by the running machine.

The model based on the step frequency follows the equation:

$$s = c_{\mathrm{H}} \cdot f + d_{\mathrm{H}}, \tag{4.3}$$

where s is the estimated step length measured in meters taking into account the step frequency f measured in Hertz. The parameters c_{H} and d_{H} are personalized.

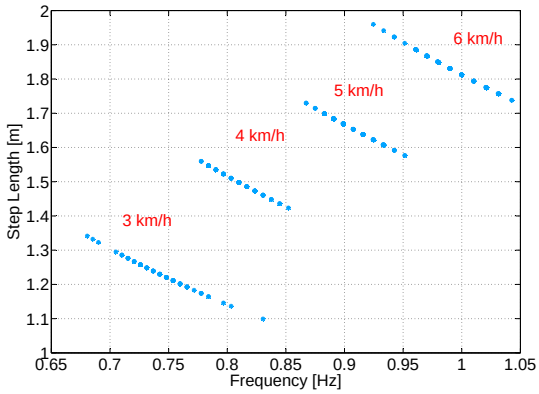

Figure 4.12: The points represent the steps from data gathered for one volunteer and each cloud of points represents a different speed.

The horizontal scenario previously described has been chosen because the step length estimator based on the frequency does not cope with the vertical displacement of the pedestrian. The scenarios H1 and H2 have been evaluated in this section. The scenario H3 simulates the walk in a museum where the pedestrian walks slowly, at approximately $2\,\mathrm{km\,h^{-1}}$. The step detector used for both step length estimators is the proposed in this thesis, thus the steps detected in both cases are identical.

Table 4.4 summarizes the errors of each step length estimator for the proposed scenarios. The parameters for both algorithms are personalized for the volunteer and constant for all scenarios, thus not adapted to different waking speeds.

Table 4.4: Performance Comparison of Different Step Length Estimators

	H1 [%]	H2 [%]	H3 [%]
Frequency	0.19	6.25	9.63
Pitch	0.18	3.24	1.15

The results summarized in Table 4.4 for the scenario H1 show that both step length estimators perform similarly at a constant comfortable speed, $3.5\,\mathrm{km\,h^{-1}}$. Such an accurate estimation of the length of the trajectory, with errors below 1%, is possible because the sensor is attached to the body of the pedestrian. This is a clear advantage of the pocket location: the movements of the sensor are tightly coupled with the movements of the pedestrian.

The results corresponding to scenario H2 provides less accurate results, which are caused by different walking speeds. Speed changes clearly hurt both step length estimators, because these algorithms are usually adapted to work optimally at a comfortable and quasi-constant walking speed.

The scenario H3 represents an extreme situation for both step length estimators because the walking speed is $2\,\mathrm{km\,h^{-1}}$ and the walk includes some stops. This speed is far from the optimal working zone of the regression line for both step length estimator models. The results show, however, higher error for the step length estimator based on

the step frequency. The frequency for this model was computed as the inverse of the time between steps. A more sophisticated approach uses the Fourier transform to find the walking frequency. However, this method requires periodicity, which is not fulfilled due to speed changes by turning or stopping.

The analyzed experiments show the benefits of using the proposed step length estimator when the sensor is attached to the upper part of the leg. The optimal working zone of the regression line of the pitch based model is larger than the one based on the step frequency. Thus, the proposed model can cope with a wider range of walking speeds.

4.2.5 Discussion

This section aims at evaluating the proposed step length estimator based on the pitch angle and comparing its performance with the literature algorithms. The results of the experiments carried out under challenging scenarios let conclude that the proposed algorithm provides accurate results for a large range of walking speeds, whilst the state of the art algorithm based on the step frequency only provides accurate results for a predetermined walking speed.

4.3 Vertical Displacement Estimation

The proposed vertical displacement estimator algorithm, which is based on the pitch angle, is detailed in this section. First, the experiments carried out in order to find a model will be shown and then the model derivation will be explained. In order to estimate the vertical displacement with the pitch angle, a set of experiments has been carried out with the objective of finding a relationship between the pitch angle and the height of the steps of the stairs.

4.3.1 Experimental Set Up

The experiment consists of analyzing the pitch angle estimation of steps taken walking up- and downstairs. Measurements corresponding to almost 400 steps up and down have been recorded by one volunteer in order to study the relationship between pitch amplitude and height of the steps of the stairs. To record these measurements, the IMU DSP-1750 has been mounted externally in the pocket with the help of a solid wood base, as indicated in Figure 3.8. The pitch angle estimation, which is considered error-free, has been computed integrating the FOG turn rate measurements without subtracting the biases estimation or applying updates.

A wooden staircase of adjustable steps which vary in height between 15 cm and 25 cm has been built to carry out this experiment. The height of the steps has been chosen based on the document “Visual Interpretation of the International Residential Code” [69]. This

document specifies that the maximum height for the step of the stairs should be 19.7 cm. For spiral stairs a maximum height of 24.1 cm is recommended. The minimum depth of a step of the stairs is 25.4 cm.

The results shown in Figure 4.13 prove that a relationship between the pitch amplitude and the height of the steps of the stairs exists, indicating that the higher the step of the stairs is, the larger the pitch amplitude will be. The same behaviour is observed when the pedestrian walks up- and downstairs.

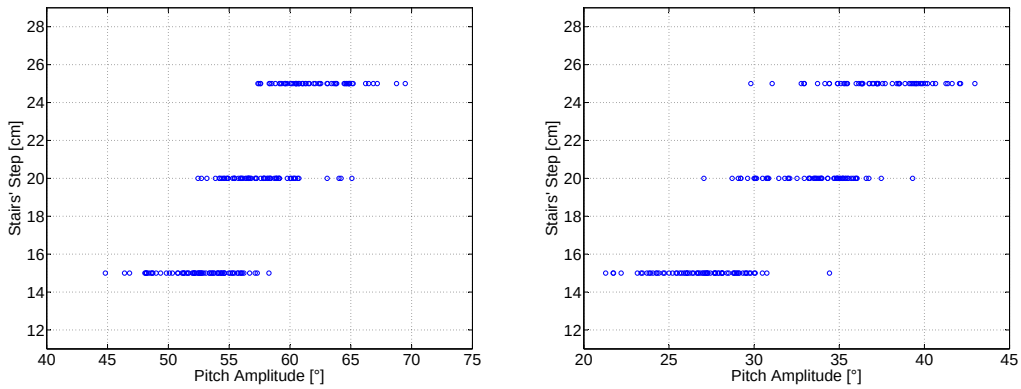

(a) Measurements of steps recorded walking upstairs.

(b) Measurements of steps recorded walking downstairs.

Figure 4.13: The points represent the steps recorded when the volunteer was walking up- and downstairs on the adjustable wooden staircase. The pitch amplitude is represented against the height of the steps of the stairs.

For assessing the results of the experiment of the wooden adjustable staircase, the same experiment has been done using the stairs of the DLR building office. The height of the steps of the stairs is 17 cm. Measurements corresponding of around 180 steps up and down have been recorded. The value of the estimated pitch amplitude for this particular height of steps is 53.07° and 26.62° for up- and downstairs respectively. These values match the experiments carried out with the wooden staircase whose results are shown in Figure 4.13.

4.3.2 Model Derivation

The chosen model for the measurements shown in Figure 4.13 is a linear regression:

$$v_{\mathrm{U}} = a_{\mathrm{U}} \cdot \Delta\theta_{\mathrm{U}} + b_{\mathrm{U}}, \tag{4.4}$$

$$v_{\mathrm{D}} = a_{\mathrm{D}} \cdot \Delta\theta_{\mathrm{D}} + b_{\mathrm{D}}, \tag{4.5}$$

where v_{U} and v_{D} are the estimated vertical displacement measured in centimeters for up- and downstairs, respectively. $\Delta\theta_{\mathrm{U}}$ and $\Delta\theta_{\mathrm{D}}$ correspond to the pitch amplitude measured in degrees for steps up- and down, respectively, and a_{U}, b_{U}, a_{D} and b_{D} are parameters, either personalized for each pedestrian or universal.

It is important to note that the pitch amplitude walking up- and downstairs is caused by the vertical and horizontal displacement of the pedestrian. If the depth of the stairs is largest than the standard, the model parameters should be re-calibrated, even for the same pedestrian. The presented model is valid to estimate the height of the steps of the vast majority of the stairs that can be found in every building, because it assumes a standard depth and focuses on the height of the step. Thus, the horizontal displacement is assumed. This is a reasonable assumption because, as shown in [69], the stairs of any building are standardized and adapted to the length of the human foot. Additionally, the most important characteristic of the stairs is their height, that allows estimating the height between floors.

The amplitude of the pitch angle is buffered when the pedestrian walks up- and downstairs. There are small differences in the pitch amplitude, however, the vertical displacement is the same because the height of the steps is the same for the whole staircase. The height of the steps of the stairs is estimated as the average of the pitch amplitude of all steps using the models presented in Equations (4.4) and (4.5) respectively.

4.3.3 Experimental Results

A comparison with the state of the art is not possible because the inertial step-and-heading algorithms are defined in 2D. Their extension towards 3D is only possible with extra sensors like barometers, or extra information like maps. The displacement estimator has been tested with a multi-storey walk in a real world scenario: a well-attended museum. In order to evaluate only the horizontal and vertical displacement, the estimated yaw has been compensated. Figure 4.14 shows the 3D view of the estimated trajectory of a 10 min walk recorded at the Deutsches Museum, which is located in Munich, Germany.

The trajectory shown in the figure has been computed using only a three-axis accelerometer and a three-axis gyroscope. The magnetometer has not been used in order to have unaided inertial positioning. No aid from other sensors such as barometer, WLAN/UWB ranges, satellite pseudoranges, maps, etc. was used. The step detector and the step length estimator used are those which have been proposed in this thesis with the universal parameter a_H and the personalized parameter b_H for the volunteer. The drift in the yaw has been compensated in order to evaluate only the influence on the trajectory of the errors in the pitch angle that may cause errors in the step detector, step length estimator and vertical displacement estimator, and the errors of the proposed algorithms themselves. One step is counted between consecutive hits on the floor of the same foot. Therefore, the depth of each step of the stairs shown in Figure 4.14 has a predefined length of 0.52 m, twice the standard depth of 0.26 m [69].

The main part of the trajectory is on the ground floor and is depicted in blue, dark blue for the initial part starting at (0,0,0) and light blue for the final part for walking back to the starting point. This area of the museum shows real ships and aircrafts. The

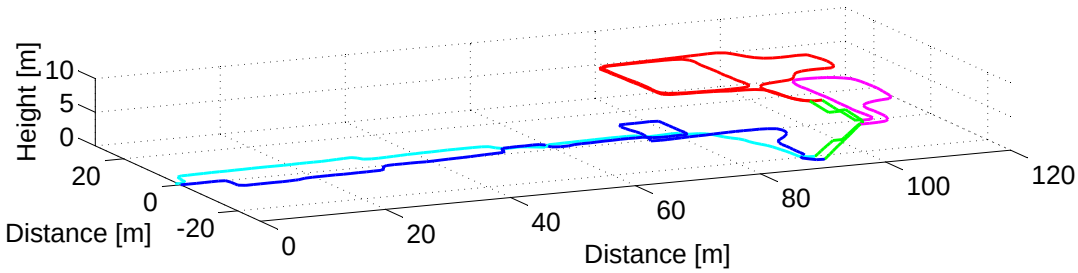

Figure 4.14: 3D view of the trajectory estimation of a 10 min walk recorded with medium-cost MEMS sensors at the Deutsches Museum, Munich (Germany). The drift error has been compensated. Colors represent different floors whilst stairs are represented in green.

stairs are depicted in green. First, the pedestrian visited the mezzanine, which is a narrow area depicted in magenta. The pedestrian walked around it and took the stairs again to go up to the first floor, which is depicted in red. The pedestrian walked around for a few minutes, repeating part of the trajectory, taking again the stairs to go back to the ground floor again. The way back to the main entrance is depicted in light blue. On the way back the pedestrian walked on a slightly different path compared to the way forward, surrounding two big ships which are located between 10 m and 50 m in the main exhibition hall.

Figure 4.15 shows the vertical displacement estimation of the pedestrian over time for the aforementioned walk. For clarity, the colour code is the same as Figure 4.14.

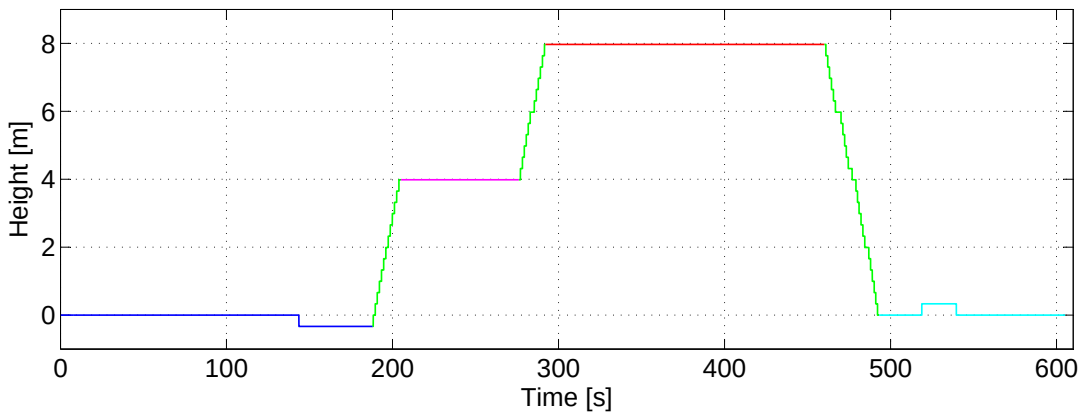

Figure 4.15: Vertical displacement estimation over time of the walk shown in Figure 4.14 recorded at the Deutsches Museum, Munich (Germany).

The results of this figure assess that the vast majority of steps up and down are detected. However, the fact that the steps of the stairs are detected in pairs causes that, if a single step up or down is taken with the leg which does not have the sensor in the pocket, it may not be detected. This happens with the platform situated in the ground floor. The detector only detected the step down at the second 150, but not the step up. This platform was however correctly detected on the way back, as the light blue line

represents. One extra step up is false detected in the first part of the stairs caused by the same reason. The correct detection of steps up and down depends on the number of steps of the stairs (odd or even) and on the foot the pedestrian starts walking on the stairs.

The estimation of the height of the steps of the stairs based on the amplitude of the pitch angle for up- and downstairs is summarized in Table 4.5.

Table 4.5: Deutsches Museum Step Height Estimation

	Estimated Height [cm]	Real Height [cm]	Error [%]
v_{U}	33.1	33.2	0.3
v_{D}	32.9		0.9

The errors on v_{U} and v_{D} corresponding to the vertical displacement upstairs and downstairs, respectively, are below 1%. This result implies an error of 1 m every 100 m of vertical displacement of the pedestrian. It is reasonable to consider that an error is not acceptable if a confusion between consecutive floors is possible. Assuming a separation of floors of 3 m, an error of 1% in the vertical displacement implies that the pedestrian has to walk 300 m up or down in order to mistake one floor, and this is highly unlikely to happen. Therefore, it is recommended to use the pitch angle, not only for detecting steps and estimating the step length, but also for estimating the height of the steps of the stairs and, consequently, the height between floors.

4.3.4 Discussion

This section has presented the vertical displacement algorithm derived from the research carried out in this thesis that makes for the first time possible to solve 3D positioning for unaided inertial systems using the step-and-heading approach. This algorithm has been tested in a real multi-storey scenario. Since the height of the steps of the stairs is the same for all steps and the same walking up- and downstairs, the estimated height is averaged to avoid outliers. The estimated separation between floors is accurate for pedestrian navigation purposes in order not to mistake floors. Although the proposed vertical displacement algorithm in this section is derived with one volunteer, it is used throughout this thesis with volunteers of different height, age and gender.

Chapter 5

Drift Estimation

Tal vez sea la simplicidad del asunto
lo que nos conduce al error.

Edgar Allan Poe

Drift is defined in pedestrian navigation as the remaining yaw angle error that the orientation estimation algorithm is not able to correct. The yaw angle is less observable than the roll and pitch angles, which can be estimated through the gravity field. Therefore, the yaw angle accumulates a higher error that mainly arises from a poor estimation of the bias of the z-axis gyroscope. However, the drift is not only composed by this bias, which has a slow changing behaviour, but also includes other slow changing errors like temperature sensibility.

The main motivation to research a drift estimation algorithm is the fact that the yaw angle is of key importance for pedestrian navigation. In fact, this angle accumulates a large error, whose main consequence is to gradually twist the trajectory making it unrecognizable. In this thesis, a novel automatic drift compensation algorithm that only makes use of inertial measurements is proposed. The presented algorithm works seamlessly, thus it does not require the pedestrian to interact with the navigation system, e.g. press a button.

The algorithm gradually extracts information of the building layout as the pedestrian walks. This information is stored in a data base and used when the pedestrian re-visits the identified places. The presented algorithm adds a great value to the state of the art, since it estimates the drift value and feeds it to the orientation estimation filter. As a consequence, the yaw angle error is limited, avoiding the ever increasing yaw angle uncertainty.

The building layout can be described using landmarks, thus a great amount of memory is saved by not storing every wall of the building. A landmark should be easily observable and re-observable, distinguishable from each other, stationary and the environment should be plenty of landmarks. Taking into account these requirements, it has been decided to

use stairs and corners of buildings or urban scenarios. These landmarks are seamlessly detected while the pedestrian walks.

In order to properly describe the landmark detection and association algorithms, the position of the landmarks is necessary. As shown in Figure 1.1, the position and position uncertainty of the pedestrian is provided by the position estimation algorithm, that will be described in Chapter 6. Since landmarks are detected during the walk, its position is coincident with the position of the pedestrian at the moment of the detection. Therefore, its position is calculated with the equations corresponding to the proposed 3D step-and-heading approach:

$$\begin{aligned} x^j &= x^{j-1} + s^j \cdot \cos(\psi^k), \\ y^j &= y^{j-1} + s^j \cdot \sin(\psi^k), \\ z^j &= z^{j-1} + v^j, \end{aligned} \tag{5.1}$$

where x^j, y^j and z^j represent the position in the x-, y- and z-axis at the time j, respectively, s^j stands for the step length at the time j, v^j for the vertical displacement at the time j and ψ^k is the yaw angle at the time k. The orientation estimation filter runs at $f_s = 100\,\text{Hz}$, while a new step length, vertical displacement and position are computed once per step. Therefore, the index j accounts for the number of steps taken.

5.1 Landmark Detection

The first step to compute the drift is to detect the landmarks that describe the building layout, in this case corners and stairs. The proposed drift compensation algorithm provides a seamless detection using only the orientation estimation, particularly the pitch and the yaw angle.

5.1.1 Corner Detection

The movement of a pedestrian is to some extent unconstrained, unlike for example the movement of a train that is only able to drive on rails. However, typical manmade scenarios introduce some restrictions to the free movement of the pedestrian. Due to the layout of buildings and cities, the most common corner in rooms and between building blocks describes a 90° turn.

The shape of the corners is naturally described by the trajectory of the pedestrian by entering and leaving rooms in a building or walking between building blocks to reach the destination. The proposed basic detector identifies the corners using the yaw angle estimation provided by the orientation estimator.

Figure 5.1(a) shows in blue the yaw angle estimation provided by the orientation estimator for a sensor placed in the front pocket of the trousers. Initially, the pedestrian was

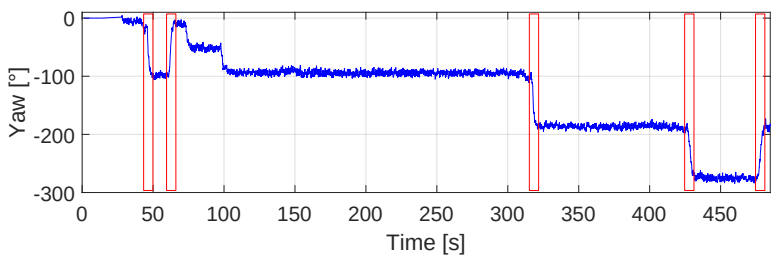

(a)

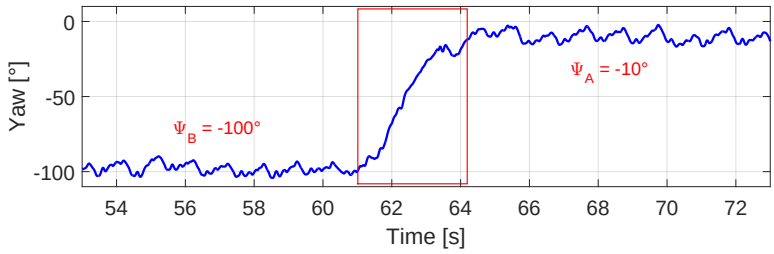

(b)

Figure 5.1: The blue curve represents the yaw angle estimation during a walk for a sensor placed in the front pocket of the trousers. The yaw angle during the corners detected in the trajectory is highlighted in red. The lower subfigure depicts a zoom of the second detected corner of the upper subfigure.

standing for almost 25 s. The wavy shape of the curve shown in Figure 5.1(b) corresponds to the movement of the hip of the pedestrian while walking. The red rectangles highlight the yaw angle estimation during the detected corners corresponding to 90° turns, which are identified by the corner detector. Between second 75 and 100, two consecutive 45° turns are made, but these are not considered by the corner detector algorithm. Apart from the clearly visible turns, the rest of the time the pedestrian walks on a straight path.

Two buffers whose window length is q are used to detect corners using the yaw angle estimation:

$$\begin{aligned} \overline{\psi}_B &= \frac{1}{q} \cdot \sum_{k=1}^{q} \psi^k, \\ \overline{\psi}_A &= \frac{1}{q} \cdot \sum_{k=q+m}^{2q+m} \psi^k, \end{aligned} \tag{5.2}$$

where ψ^k is the yaw angle estimation at the time k, $\overline{\psi}_B$ and $\overline{\psi}_A$ represent the averaged yaw angle before and after the corner, respectively, and m stands for the separation between buffers.

The movement of the hip makes the use of a buffer necessary to compute the averaged yaw angle value over a significant period, instead of taking a single value before and after the corner. Given that a typical walking speed is one step per second, the window length is chosen to be 1 s. Therefore, $q = 1 \cdot f_s$, being f_s the sampling frequency of the sensor. The separation between the averaged yaw angle before and after the corner, $\overline{\psi}_B$ and $\overline{\psi}_A$ respectively, is set to 5 s. Therefore, $m = 5 \cdot f_s$. The values of q and m will be initially

set as indicated, however, there is a strong dependency on the walking speed. Thus, the parameters q and m will be adapted taking it into account. The walking speed of the pedestrian is computed based on the step length and the time between detected steps, data provided by the displacement estimator.

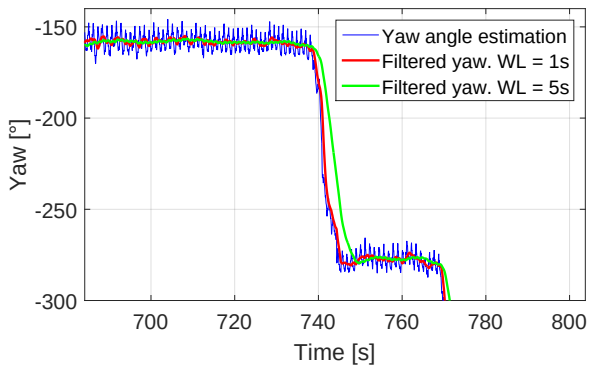

Figure 5.2: The blue curve represents the yaw angle estimation, the red curve is the filtered yaw angle estimation with a window length of 1 s and the green curve is the result of filtering the yaw angle with a window length of 5 s.

As Figure 5.2 shows, the yaw angle estimation contains peaks of approximately 20° amplitude for a typical walking speed. These peaks do not affect the corner detection, but the yaw angle values assigned before and after the corner, and consequently the drift computation. The window length of the buffer q has been set to 1 s in order not to delay the corner detection. However, as seen in the figure, a window length of 5 s offers a more stable filtered yaw angle.

Medium-cost MEMS gyroscopes have a short-term stability and turns around corners are usually made within a very short period of time. Thus, the estimated yaw angle during corresponding to the corner is considered error-free. However, the natural walking style does not always describe exact 90° turns. Thus, a corner is detected when the absolute value of the difference of the averaged yaw angles $\overline{\psi}_B$ and $\overline{\psi}_A$ lies between r_1 and r_2 according to:

$$r_1 < \left|\overline{\psi}_B - \overline{\psi}_A\right| < r_2, \tag{5.3}$$

where $r_1 = 80°$ and $r_2 = 100°$. The difference between the averaged yaw angle before and after the corner has to be evaluated regardless its sign. The sign of the yaw angle estimation responds to the direction of the turn, thus a turn to the right will increase the yaw angle value and a turn to the left will decrease it. The corner detector should identify corners in both directions. If a corner is detected, the landmark association process starts.

An improved corner detector able to cope with large aperture radius or corners performed at very low walking speed is in the following presented.

The improved corner detector is based on the fact that the yaw angle only changes substantially its value at the corners. Otherwise the yaw angle estimation is quasi-flat. Therefore, the derivative signal of the yaw angle shows peaks when the corners are de-

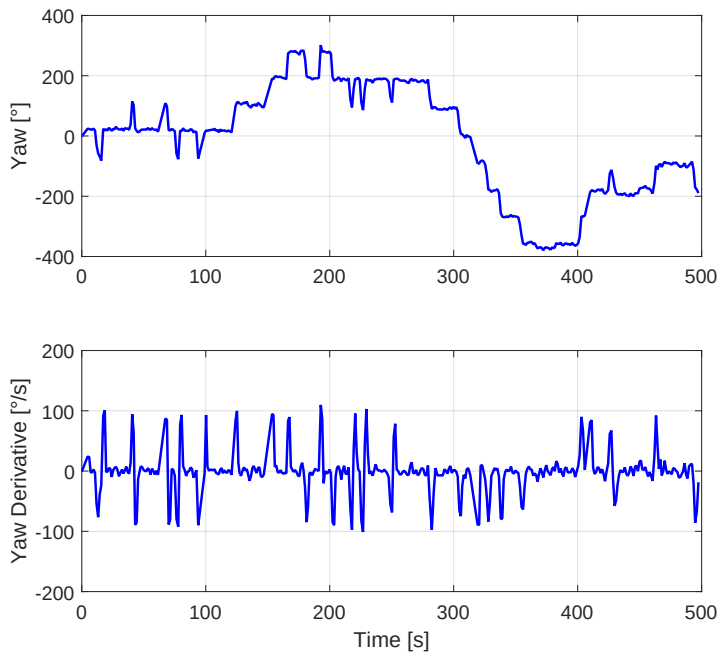

Figure 5.3: The upper subfigure shows the yaw angle estimation and the lower subfigure shows the derivative signal of the upper subfigure.

scribed. Figure 5.3 shows both, the yaw angle estimation in the upper subfigure and the derivative signal of the yaw angle in the lower subfigure.

The start and ending time stamps of the peaks on the derivative signal (lower subfigure) are used to identify on the yaw estimation (upper subfigure) the values of the jump in the yaw angle that determine the corner described, i.e. 90° or 180°.

5.1.2 Stair Detection

Stairs represent an unambiguous landmark that connects different floors. The stair detector algorithm identifies them using the pitch angle estimation provided by the orientation estimator. The physical concept and the algorithm of the stairs detector have already been introduced in Sections 4.1.2 and 4.1.3, respectively, since the detection of the activities walking up- and downstairs correspond to the detection of the stairs.

5.2 Landmark Association

The presented drift estimation algorithm requires re-visiting the already detected landmarks. For example, it is likely that the turn described around a corner to enter a room is again described when leaving the room. Likewise, the stairs that have been climbed up are at some point climbed down again.

The data base of the landmarks, whose structure is shown in Table 6.2 with two examples, comprises all parameters of the detected landmarks. The *Type* flag is 0 for

corners and 1 for stairs. This flag is designed to reduce the searching time, since it allows comparing only landmarks of the same type. The *Time* is the time stamp where the landmark has been detected, counting from the beginning of the walk. The *Position* (x,y,z) is the 3D position of the landmark in the navigation frame, which is stored in the data base together with the *Uncertainty*, which is the variance-covariance matrix representing the position uncertainty. Last, the *Yaw* angle value is taken from the orientation estimator and has two formats: for corners it defines the yaw angle before and after turning the corner, and for stairs it defines the direction in which the stairs are gone through.

Landmarks are defined as short trajectories, however, their corresponding position stored in the data base is a single 3D point. The stored position corresponds to the central point of the short trajectory describing the landmark. The stored uncertainty is the corresponding to this 3D point.

Table 5.1: Example of the Data Base of the Landmarks

	Type	Time [s]	Position [m]	Uncertainty [m^2]	Yaw [°]
L1	0	17.3	(5.12, 2.06, 3.5)	$\begin{pmatrix} 0.45 & -0.31 & 0 \\ -0.31 & 0.41 & 0 \\ 0 & 0 & 0.02 \end{pmatrix}$	(24.5, -80.4)
L2	1	59.6	(7.11, -1.03, 2)	$\begin{pmatrix} 0.62 & -0.42 & 0 \\ -0.42 & 0.89 & 0 \\ 0 & 0 & 0.28 \end{pmatrix}$	90.3

If the landmark is new, it is included in the data base. If the landmark is already stored in the data base, an association is possible. The decision whether a landmark is new or not will be taken based on the position of the current landmark and the position of all stored landmarks of the same *Type* detected on the same floor. The position, however, will not be coincident even for the same landmarks due to the accumulated drift over time and also due to other possible errors in the step length computation or false step detections, among others.

The associator does not differentiate the direction in which the stairs are gone through. Therefore, a staircase will be associated if the first time the stairs were climbed up and the second time were climbed down, as well as if it is both times climbed up or climbed down. The same applies to corners, that are associated regardless of the direction of the trajectory, which causes different *Yaw* combinations. Figure 5.4 shows the different combinations that the associator matches: trajectory completely overlapped, trajectory partially overlapped and no overlap.

There are different metrics to evaluate the distance between landmarks. The Euclidean distance has been discarded because it does not account for the uncertainty, which is an ellipsoid shaped volume around the mean position value. The Mahalanobis distance [70]

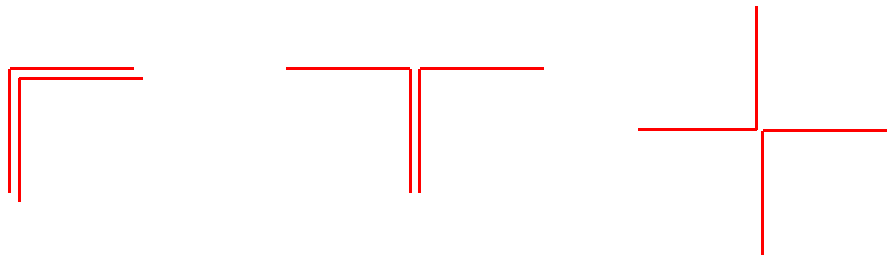

Figure 5.4: Different combinations that are associated by the corner associator regardless of the direction of the trajectory.

is more adequate to evaluate the distance between landmarks:

$$\Delta_{1,2}^2 = \Delta_{2,1}^2 = [(x_1, y_1, z_1) - (x_2, y_2, z_2)] \cdot [\boldsymbol{P_1} + \boldsymbol{P_2}]^{-1} \cdot [(x_1, y_1, z_1) - (x_2, y_2, z_2)]^T, \quad (5.4)$$

where $\Delta_{1,2}$ accounts for the distance between the stored and the current landmark, (x_i, y_i, z_i) for $i = \{1,2\}$ represents the position of each landmark and $\boldsymbol{P_i}$ for $i = \{1,2\}$ represents the variance-covariance matrix of each position.

For multivariate normally distributed data, the squared Mahalanobis distances Δ^2 are approximately χ-square distributed with n degrees of freedom. For the algorithm proposed in this thesis, $n = 6$, being the 6 degrees of freedom of the 3D position of the pedestrian: (x, y, z), the yaw angle ψ, the step length s and the vertical displacement v. These 6 parameters conform the augmented state of the position estimation filter that will be explained in Chapter 6. The threshold κ to decide if the current landmark is possibly the same as one of the stored ones is fixed and also depends on the confidence level. For a confidence level of 99.7 % and $n = 6$ the threshold $\kappa = 4.48$ [71].

Wrong associations using the Mahalanobis distance are possible are likely with large landmark uncertainties. A suitable method to discard wrong associations consists of a multi-hypothesis filter that creates a different hypotheses for each possible possible association. The hypothesis whose associations derive the correct drift value will continue associating, so that hypotheses with wrong drift values can therefore be discarded. However, the multi-hypothesis filter has not been included in this thesis.

Associations are therefore decided taking into account the uncertainty of the position, which includes the uncertainty of both, yaw angle and displacement. Thus, if the uncertainty is large due to the accumulated drift error, more than one hypothesis might be possible. The maximum elapsed time to associate landmarks strongly depends on the yaw uncertainty and on the distribution of the detected landmarks. A bias value of $0.1\,^\circ\,\mathrm{s}^{-1}$ causes 360° error in the yaw estimation after 1 h. This rapid growth of the yaw error due to the bias, makes it important to have drift observations in early phases and ideally apply these corrections online.

5.3 Drift Computation

The bias of a gyroscope is the averaged value of the turn rate measurements during a static phase. The integration of a constant bias causes an error growing linearly with time. The bias stability, β, describes how the bias of the gyroscopes may change over a specified period of time under stable conditions, usually at a constant temperature. Temperature fluctuations due to changes in the environment and sensor self-heating modify the biases value [72]. The change in temperature causes an orientation error which grows linearly with time.

The drift is composed mainly by the bias of the z-axis gyroscope, but it also includes other slow changing errors, i.e. temperature errors. As presented in Section 3.1, the lower the β and the larger the t_β values are, the more stable is the bias of the gyroscopes. The drift computation algorithm aims at estimating the error, which linearly grows with time. However, the estimation of the drift is not constant over the complete trajectory, it changes gradually to be adapted to the slow drift fluctuations. When the first landmark is associated, the first drift value is computed. The following associations refine the first computed drift value, by adding or subtracting small drift contributions which correspond to the slow drift changes. It is not necessary for the correct tracking of the drift to re-visit every landmark stored in the data base, but to have regular associations to track slow drift changes.

The drift computation algorithm for corners and stairs is based on the principle that having zero drift, the yaw angle values of associated landmarks are equal. Figure 5.5 (left) shows a schematic drifted trajectory represented with the dashed blue line. The pedestrian left the room, walked to the main entrance and went back to the same room. A corner, highlighted in red, is detected when leaving and entering the room. These corners are identified as the same landmark. Figure 5.5 (right) shows a schematic 3D drifted trajectory represented with the dashed blue line. In the represented walk, the pedestrian left the first room, climbed up the stairs to the second floor and then climbed down the stairs and entered the small room on the other side of the building. The stairs, highlighted in red, are detected when going up and down. Both parts of the trajectory described on the stairs will be associated as the same landmark.

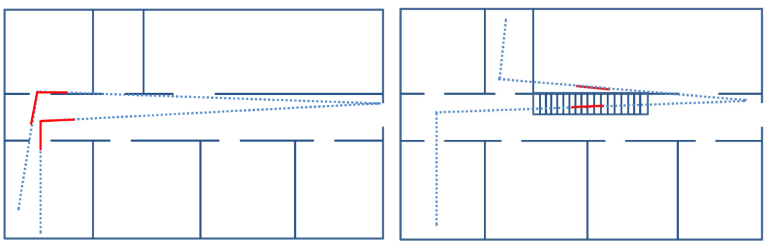

Figure 5.5: Schematic drifted trajectory including corners (left) and stairs (right).

The red arrows in Figure 5.6 represent the landmarks identified in Figure 5.5. For

the case of the corner represented in Figure 5.6 (left), the first time the landmark is detected is labeled with the sub-index 1 and when it is re-visited the sub-index is 2. As already explained, the corners are composed of two yaw angles: before and after turning the corner. For the case of the stairs represented in Figure 5.6 (right), the yaw angle measured the first time the landmark is detected is labeled with the sub-index 1 and when the landmark is re-visited the sub-index used is 2.

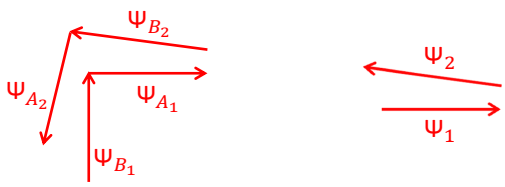

Figure 5.6: Yaw angle labels for the landmarks corner and stairs represented respectively in Figure 5.5.

The deviation angle δ represents the mismatch of trajectories, measured in degrees, due to the drift error. The angle δ is computed by subtracting the yaw angle stored in the data base when the landmark was for the first time visited and the currently detected yaw angle. For Figure 5.6 (left) the deviation angle is computed as follows:

$$\begin{aligned} \delta_1 &= \psi_{B_1} - \psi_{A_2}, \\ \delta_2 &= \psi_{A_1} - \psi_{B_2}, \\ \delta &= \frac{\delta_1 + \delta_2}{2}. \end{aligned} \tag{5.5}$$

In the case of the stairs, as represented in Figure 5.6 (right), the deviation angle is computed as follows:

$$\delta = \psi_1 - \psi_2. \tag{5.6}$$

The deviation angle should be, in the absence of drift, 0° or 180° if the landmark has been visited in the same or in opposite direction, respectively.

In a general case valid for corners and stairs, the observations, which are the yaw angles detected the first visit and the re-visit, ψ_1 and ψ_2, are related to the drift value ϵ as indicated:

$$\psi_2 = \psi_1 + \int_{t_1}^{t_2} \epsilon \, \mathrm{d}t. \tag{5.7}$$

In the case of constant drift:

$$\epsilon = \frac{\delta}{\Delta t} \tag{5.8}$$

being ϵ the drift, δ the deviation of the trajectory and $\Delta t = t_2 - t_1$ the elapsed time between the first visit and the re-visit. Landmarks are not re-visited with exactly the same yaw angle, therefore we account for an error of 4° standard deviation in ψ_1 and ψ_2, respectively. This error implies that the elapsed time between landmarks Δt should be larger than 2 min in order for the standard deviation of the resulting drift ϵ to be smaller

than $0.05\,^{\circ}\,\mathrm{s}^{-1}$. Associations whose elapsed time is shorter than 2 min are discarded.

The proposed algorithm assumes a slowly changing drift affecting the trajectory. The data base is cleared after each association to guarantee that the section of the trajectory comprised between associated landmarks has been affected by a slowly changing error. Clearing the data base also acts as garbage collector avoiding the data base to grow without limits.

5.4 Relationship between Drift and z-Axis Gyroscope's Bias

In order to evaluate how the bias of the z-axis gyroscope influences the drift value computed as a result of an association, an experiment has been carried out. The IMU DSP-1750 has been mounted externally on the upper part of the leg of the pedestrian with the help of a solid wood base, as indicated in Figure 3.8. The 22 min walk represented in Figure 5.7 with a red line, took place at the Theresienhöhe in Munich and consists of a path duration of 22 min, approximately 1.1 km long and with a covered area of approximately $46\,000\,\mathrm{m}^2$. The red pin represents the start and the end point of the trajectory and the rest of the pins highlight the described corners. Among these corners, the green pins represent the potential associations.

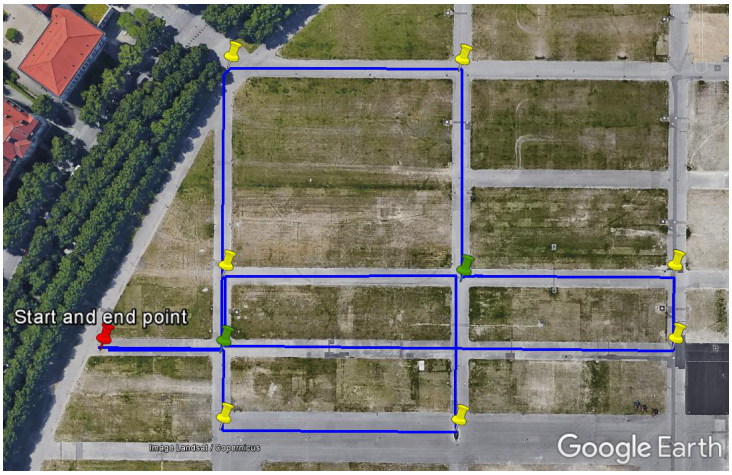

Figure 5.7: The walk recorded with the IMU DSP-1750 is represented with a blue line. The yellow pins highlight the corners described during the walk and the green pins represent the corners which can be associated.

The yaw angles shown in Figure 5.8(a) have been computed integrating the FOG turn rate measurements without subtracting the biases estimation or applying updates. The orientation angles computed with FOG turn rate measurements are considered quasi-error-free. To obtain the odometries of Figure 5.8(b), the displacement estimation algorithms for the step detection and step length estimation have been used. Therefore, the length of the trajectory may contain errors which do not influence the following analysis.

The blue curves of Figure 5.8 correspond to the computation of the yaw angle and trajectory, respectively, using the quasi-error-free turn rate measurements. The green

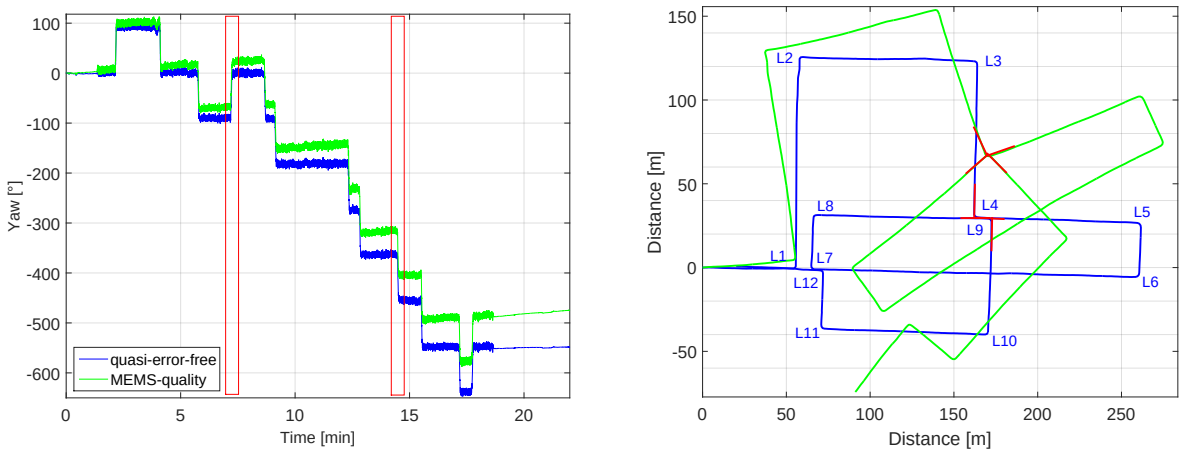

(a) (b)

Figure 5.8: Walk recorded with the IMU DSP-1750. (a) represents the yaw angle estimation and (b) the trajectory. The blue curves have been computed directly using the recorded data and the green curves have been computed introducing a z-axis bias of $0.05\,^{\circ}\,\mathrm{s}^{-1}$. The corners are labeled and two of them are highlighted in red.

curves represent the computation of the yaw angle and trajectory respectively adding an artificial bias of $0.05\,^{\circ}\,\mathrm{s}^{-1}$ to the z-axis gyroscope. The red rectangles of Figure 5.8(a) correspond to the corners L4 and L9 highlighted in red in Figure 5.8(b).

The corners highlighted in red in Figure 5.8(b), L4 and L9, yield to the data base entries summarized in Table 5.2. The *Time* and *Yaw* angle values have been chosen manually from Figure 5.8(a). The position values have not been filled for shortness.

Table 5.2: Landmark Information Stored in the Data Base

	Type	Time [s]	Position [m]	Uncertainty [m^2]	Yaw [°]
L4	0	432.3	-	-	(-66.7, 23.1)
L9	0	870.1	-	-	(-314.9, -403.7)

The deviation angles, δ, derived from the unwrapped *Yaw* angle values exposed in Table 5.2 are 22.7° and 22.1° for both, before and after turning the corner. Thus, a mean deviation angle of 22.4° has been accumulated over 437.8 s, which yields a drift value of $0.051\,^{\circ}\,\mathrm{s}^{-1}$. It can be concluded that the drift value computed as a result of the association matches the z-bias value artificially introduced.

The following analysis is carried out in order to discard the possibility that biases on the x- and y-axes also affect the yaw angle estimation, and as a consequence, also the computed drift value after an association. Figure 5.9 shows the error of the yaw angle estimation caused by a x- and y-bias, respectively. Figure 5.9(a) has been obtained after artificially adding to the FOG turn rate measurements a x-bias value of $0.05\,^{\circ}\,\mathrm{s}^{-1}$. Figure 5.9(b) has been obtained after artificially adding to the FOG turn rate measurements a y-bias value of $0.05\,^{\circ}\,\mathrm{s}^{-1}$. The error has been computed by subtracting the resulting yaw angle estimation to the quasi-error-free yaw angle.

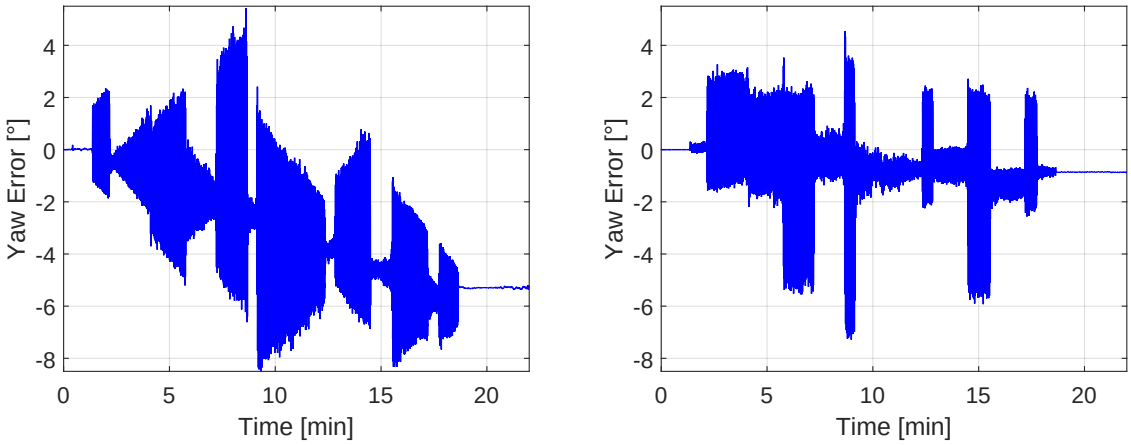

(a) artificial x-bias

(b) artificial y-bias

Figure 5.9: (a) shows the yaw error caused by an artificial x-bias of $0.05\,^{\circ}\,\mathrm{s}^{-1}$. (b) shows the error on the yaw angle caused by an artificial y-bias of $0.05\,^{\circ}\,\mathrm{s}^{-1}$.

As Figure 5.9 shows, the error caused by the x- and y-bias on the yaw angle estimation is oscillating, but in trend is growing with time. The yaw error reaches 5.5° after 22 min for the x-axis bias and less than 1° after 22 min for the y- axis bias. Although the x- and y-biases do not affect much the yaw angle estimation, they cause severe errors on the roll and pitch angle estimations, respectively. The direct consequence of having errors on the pitch angle is inaccurate displacement estimations. These errors are, however, not evaluated, since the roll and pitch angles are out of the scope of this analysis. Nevertheless, the x- and y-bias are correctly estimated in the orientation filter thanks to the *Absolute Gravity Update*, as Figure 3.14 shows. Thus, the remaining error transferred to the yaw angle is negligible. To sum up, the drift is mainly composed by the remaining z-bias of the gyroscope that can not be estimated in the orientation estimator.

5.5 Experimental Results

The algorithms proposed in this chapter, i.e. the landmark detector, the landmark associator and the drift computation algorithm, will be evaluated in this section. In order to create an artificial known drift value, the IMU DSP-1750 is used as a reference. The 2D experiment of Figure 5.8 will be used in the following sections for testing the landmark detector, the landmark associator and the drift computation algorithm. This walk has been recorded by a 1.52 m height woman at the Theresienhöhe in Munich. A 3D walk recorded by a 1.82 m height man at the Earth Observation Center building of DLR will be used to test the stair detection and the basic corner detection for large curvature radius.

5.5.1 Landmark Detector

The corner detector will be first tested using the drifted green trajectory depicted in Figure 5.8(b). All 12 corners should be detected even in the presence of drift. Table 5.3 summarizes the automatically generated data base, where the uncertainty values have been omitted for shortness.

Table 5.3: Data Base Generated for the Green Trajectory of Figure 5.8(b)

	Type	Time [s]	Position [m]	Uncertainty [m^2]	Yaw [°]
L1	0	131.6	(55.63, 5.84, 0)	-	(7.62, 86.76)
L2	0	248.0	(38.69, 127.17, 0)	-	(102.38, 22.30)
L3	0	348.2	(137.02, 148.71, 0)	-	(14.94, -63.14)
L4	0	436.9	(167.98, 67.35, 0)	-	(-69.27, 20.72)
L5	0	525.1	(253.98, 96.92, 0)	-	(23.03, -64.40)
L6	0	552.6	(260.91, 71.81, 0)	-	(-63.93, -149.98)
L7	0	744.2	(106.66, -15.65, 0)	-	(-140.73, -237.35)
L8	0	774.2	(95.31, 7.58, 0)	-	(-233.36, -322.20)
L9	0	873.7	(168.52, 63.90, 0)	-	(-318.15, -403.04)
L10	0	936.0	(205.98, 18.92, 0)	-	(-401.74, -495.63)
L11	0	1035.4	(144.98, -40.57, 0)	-	(-490.09, -579.07)
L12	0	1068.9	(122.27, -26.70, 0)	-	(-574.61, -487.75)

For this experiment the walking speed was in average $3\,\mathrm{km\,h^{-1}}$ and all corners are successfully detected. For higher walking speeds, the initially set values for the parameters q and m are also appropriate, because the yaw angle transition before and after the corner is steeper. Nevertheless, both parameters can be adapted based on the known walking speed. Additionally, the curvature radius of the corner plays an important role in the detection. For a large curvature radius, the detection might not be successful due to the smooth yaw angle transition before and after the corner. For these cases, the parameter m should be greater. However, there is no information available to adapt this parameter in the case of large curvature radii, since the trajectory is not previously known. Therefore, these corners are not identified with the proposed basic corner detector and, consequently, not used for the drift computation.

The trajectory depicted in Figure 5.10 includes corners of small and large curvature radii and also stairs out- and inside the Earth Observation Center building of DLR. The start and end point of the walk is located outdoors as the red colored pin of Figure 5.10(a) indicates. Table 5.4 shows the first 9 landmarks automatically detected during the walk described in the following: The pedestrian starts walking leaving the front garden of the building at his left hand. The first described corner is not detected with the basic corner detector due to its large curvature radius. Therefore, it is not taken into account for the drift computation, as well as the two following curves, since they do not describe a 90° turn. The first detected corner lies on the back garden and is highlighted with

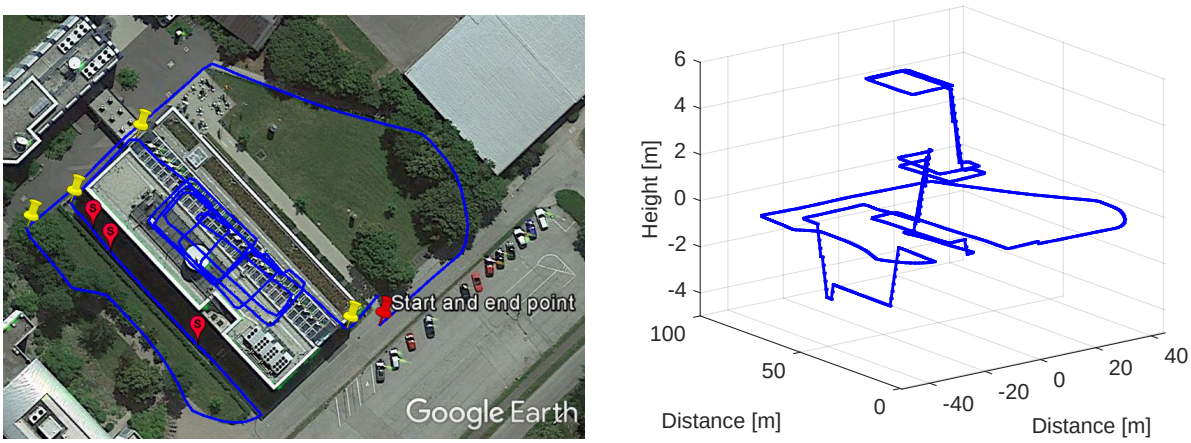

(a) (b)

Figure 5.10: (a) shows the trajectory computed with the quasi-error-free measurements. The red pin highlights the start and end point, the yellow pins the detected outdoor corners and the pink placemarks the detected outdoor stairs. (b) shows the three dimensional view of the computed trajectory.

a yellow pin in Figure 5.10(a). Then three outdoor stairs to access the basement are detected with a very similar yaw angle (see Table 5.4), because they are aligned. Their location has been represented with pink placemarks on the back garden. Then, two more corners are detected outdoors until the pedestrian walks into the building. All described indoor corners are detected and also the indoor stairs. In total, 36 landmarks have been detected for the trajectory shown in Figure 5.10. The first landmark described indoors corresponds to the stairs, which is twice detected due to the landing zone, unlike the case of the outdoors upstairs which also have a landing zone as shown in Figure 5.11.

Table 5.4: Part of the Data Base Generated for the Trajectory of Figure 5.10

	Type	Time [s]	Position [m]	Uncertainty [m^2]	Yaw [°]
L1	0	169.3	(-46.07, 73.55, 0)	-	(178.74, 268.70)
L2	1	264.4	(-34.35, 24.10, -0.99)	-	453.74
L3	1	306.0	(-33.78, 59.52, -2.99)	-	450.62
L4	1	314.8	(-33.41, 63.55, -0.99)	-	449.61
L5	0	327.4	(-30.41, 72.50, -0.33)	-	(454.41, 364.42)
L6	0	347.99	(-10.27, 70.31, -0.33)	-	(368.37, 272.85)
L7	1	372.1	(-8.55, 47.43, 0.33)	-	272.19
L8	1	380.2	(-8.95, 43.66, 1.99)	-	269.47
L9	0	388.0	(-11.56, 40.65, 2.99)	-	(268.49, 185.40)

The double detection may happen depending on the length of the landing zone of the stairs, being harmless to the drift computation. As Table 5.4 shows, the yaw angle detected for both sections of the indoor stairs, L7 and L8, is very similar and approximately 180° shifted to the detected direction in which the outdoor stairs, L2, L3 and L4, were described, as expected.

(a) (b)

Figure 5.11: (a) shows the three outdoor stairs of the building and (b) shows the two indoor stairs.

5.5.2 Landmark Associator

After the landmark detection, the association process starts. The first step is to identify whether the current landmark has been previously detected or it is new to the data base. The association decision is based on the Mahalanobis distance between potential associated landmarks Δ and the threshold κ.

For the drifted trajectory represented in Figure 5.12, three associations are correct: (L7, L1), (L9, L4) and (L12, L1) or (L12, L7). The information of the detected landmarks is summarized in the data base (see Table 5.3). The threshold κ is 4.48.

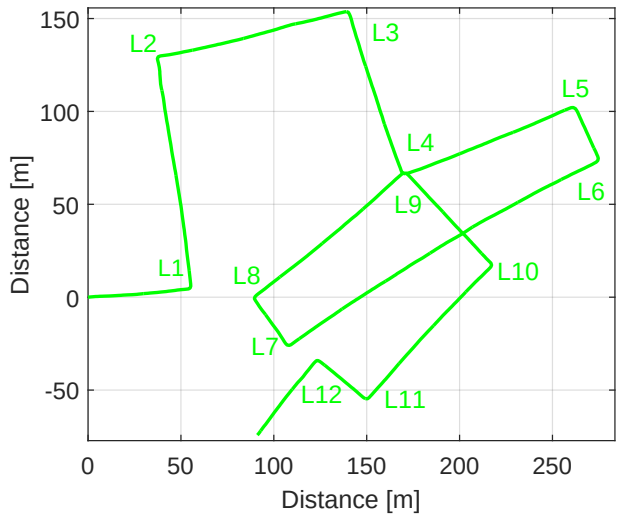

Figure 5.12: Trajectory corresponding to the walk recorded with the quasi-error-free measurements introducing a z-axis bias of $0.05\,^{\circ}\,\mathrm{s}^{-1}$. The detected corners are labeled.

The Mahalanobis distances computed by the associator for the landmark L7 are summarized in Table 5.5. As the table shows, the landmarks (L7, L1) are correctly associated.

The Mahalanobis distances computed by the associator for the landmark L9 are sum-

Table 5.5: Mahalanobis Distances Computed for the Association of Corner L7 of Figure 5.12

	L1	L2	L3	L4	L5	L6
Δ	**4.33**	10.26	11.05	6.70	12.21	11.28

marized in Table 5.6. As the table shows, the association (L9, L4) is selected as it provides a very small Mahalanobis distance. Indeed, the association is correct.

Table 5.6: Mahalanobis Distances Computed for the Association of Corner L9 of Figure 5.12

	L1	L2	L3	L4	L5	L6	L7	L8
Δ	9.75	8.66	5.03	**0.38**	5.70	5.37	5.02	4.55

The Mahalanobis distances computed by the associator for the landmark L12 are summarized in Table 5.7.

Table 5.7: Mahalanobis Distances Computed for the Association of Corner L12 of Figure 5.12

	L1	L2	L3	L4	L5	L6	L7	L8	L9	L10	L11
Δ	**4.16**	8.15	8.18	4.74	8.55	7.92	**0.79**	1.55	3.82	3.50	0.76

The uncertainty of the position and the uncertainty of the yaw angle are only growing with time, because the corrections are not activated in order to evaluate the associator. The lack of corrections leads to multiple association hypotheses. In this case, L12 can also be associated with L8, L9 and L10. The landmark L11 lies under the threshold κ, but the time between detections is not significant for computing the drift, thus it is not taken into account. The correct associations are (L12, L7) or (L12, L1). The drift has been computed using the landmark L7, because it has the smallest Mahalanobis distance.

Apart from the correct associations detailed in Tables 5.5, 5.6 and 5.7, the landmarks L8, L10 and L11 generate associations which are not correct. If the position uncertainty of the pedestrian covers a significant part of the trajectory until the first association is generated, many hypotheses should be taken into account. The position uncertainty is formed by the yaw uncertainty and the displacement uncertainty, being the first one the main source of positioning error. Therefore, it is of key importance to avoid an ever increasing yaw error by correctly modelling the bias of the z-axis in an early stage.

The conclusion from the landmark associations of the 3D walk recorded in the Earth Observation Center of DLR shown in Figure 5.10, can be summarized in two statements: first, only the corners corresponding to the same floor are eligible for the potential associations; second, if the stairs are detected in two sections due to the landing zone, both sections are correctly associated when the landmark is re-visited, because the Mahalanobis distance is smaller between both upper parts and both lower parts.

5.5.3 Drift Computation

The drift is computed between the time instants corresponding to the current landmark and the data base landmark yielding to the smallest Mahalanobis distance following Equation (5.8). Since no corrections are applied, the drift value computed in all associations must be similar, because the artificial bias value of the z-axis gyroscope is constant and equal to $0.05\,^{\circ}\,\mathrm{s}^{-1}$. Table 5.8 shows the automatically computed drift values, measured in $^{\circ}\,\mathrm{s}^{-1}$, for all detected associations of the 2D walk recorded at the Theresienhöhe described with the green line in Figure 5.12.

Table 5.8: Drift Values Measured in $^{\circ}\,\mathrm{s}^{-1}$, of the Walk of Figure 5.12

(L7, L1)	(L8, L1)	**(L9, L4)**	(L10, L4)	(L11, L7)	**(L12, L7)**
0.055	0.054	0.054	0.051	0.049	0.055

The main difficulty of computing the drift is to detect an accurate yaw angle for the landmarks. Since the sensor is located on the pedestrian upper part of the leg, the resulting yaw angle reflects oscillations due to the movement of the hip while walking. These oscillations, which have an amplitude of up to 20°, require the use of averaging buffers, q, to determine the yaw angle of the landmark. Even taking into account the average, the resulting yaw angle will contain errors because the averaging time of the buffer is limited. Additionally, the natural walk does not describe exactly the same angle when re-visiting an area, even if the walkable areas are restricted in manmade scenarios.

As Table 5.8 shows, all detected associations yield to similar drift values. The fact that the correct associations, marked in bold, and the wrong associations yield to similar drift values is due to the architecture of the manmade area visited for the walk (see Figure 5.7), because the allowed walkable directions are restricted to North-South and East-West. Although the drift value obtained with a wrong association might be correct, the landmarks should not be used for position corrections. Therefore, any wrong association complicates future associations, because the current position of the pedestrian is corrected to an erroneous area.

5.6 Discussion

The novelty of the proposed algorithm lies on computing the underlying drift value, since the current algorithms of the literature are limited to position corrections when certain areas are re-visited. Drift is accumulated on the yaw angle over time producing an increasing error that the orientation estimation filter is not able to correct. The poor observability of yaw angle and bias of the z-axis gyroscope makes this error ever growing, therefore it is imperative to develop an algorithm to limit the drift in order to guarantee the proper functioning of the orientation estimation filter.

The proposed algorithm makes only use of inertial information, therefore additional sensors are not needed. It is based on the assumption that the drift has a slowly varying nature, which corresponds to the reality. For the algorithm to compute the drift value, at least one landmark association should occur. It has been demonstrated in this chapter that the proposed landmarks, i.e. stairs and corners, can be successfully detected. The detection, however, presents challenges due to the wavy shape of the yaw angle estimation. The irregular yaw angle shape might introduce an error that will be propagated to the drift value. Additionally, the yaw angle is not repeated exactly with the same aperture during the re-visit. Therefore, it has been deduced that associations whose elapsed time is shorter than 2 min are discarded.

Associations are made based on the Mahalanobis distance, which has been chosen in order to take into account the uncertainty of the position of the landmarks. The Mahalanobis distance will face problems if the association should be closed when the position uncertainty of the detected landmarks causes multiple hypotheses. Due to the slowly varying nature of the drift, it is not necessary to detect all possible landmarks, nor to close all possible associations. In order to avoid an ever increasing yaw error, which causes a large positioning error, which in turn causes wrong associations, it is of crucial importance to bound the error of the z-bias of the gyroscope in an early stage. Little drift corrections necessary due to the slowly varying nature of the drift are automatically done during the rest of the walk.

Chapter 6

Position Estimation

El movimiento se demuestra andando.

Diogenes

The last step of any navigation system is the computation of the position. Figure 6.1(a) shows the structure of the basic inertial navigation system. This structure describes the approach mainly used in the literature, which is based on the well-known step-and-heading equations to compute the pedestrian 2D position stepwise. The two parameters needed for the position computation are the yaw angle ψ and the step length s. This approach uses directly the yaw angle generated by the orientation estimator to feed the step-and-heading equations. Therefore, the resulting position accumulates an error that grows with time. The position estimation is deterministic in the sense that only its mean is considered. The position uncertainty is disregarded because the lack of further position information sources causes an ever increasing position uncertainty.

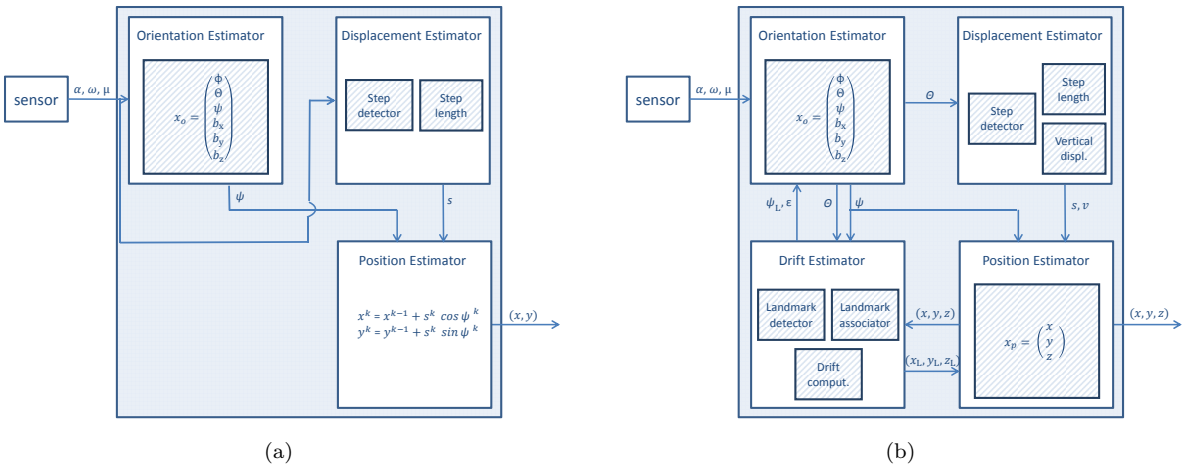

Figure 6.1: (a) system overview of the basic inertial navigation system. (b) system overview of the enhanced inertial navigation system for online drift corrections.

Figure 6.1(b) shows the structure of the enhanced inertial pocket navigation system proposed as result of the research carried out in this thesis. The proposed algorithms

provide 3D position estimations through the step-and-heading approach without the need of additional sensors. There are different sources of error in the position such as false step detections, step length or vertical displacement errors or drifted yaw angle estimations. However, as demonstrated in previous chapters, the yaw angle is the main source of positioning errors in PDR systems. In order to provide an accurate position estimation, the drift estimation algorithm will be used.

Corrections derived from the drift estimation algorithm might be applied, depending on the use case of the navigation system, online or offline. On the one hand, real-time applications usually demand a position estimation as accurate as possible for the current moment, whilst the past trajectory does not necessarily play an important role. On the other hand, some applications allow recording inertial measurements and applying the algorithms to compute the position offline. For this use case the complete trajectory is usually the key parameter, therefore no discontinuities in the trajectory due to corrections are desired.

Figure 6.1(b) shows the system overview using online corrections, where the corrections derived from the drift estimation algorithm are applied whenever two landmarks are associated, the so-called online corrections. Three particular corrections are applied when two landmarks are associated: yaw angle ψ_{L}, drift ϵ and position $(x_{\mathrm{L}}, y_{\mathrm{L}}, z_{\mathrm{L}})$. The yaw angle correction uses the yaw angle stored in the data base corresponding with the first time the landmark was visited, taken into account the direction of the re-visited landmark. The drift correction uses the computed drift value accumulated between the two associated landmarks. The position correction takes the detected position of the landmark when it was visited for the first time. These three updates feed the orientation estimation filter, for yaw angle and drift, and the position estimation filter, as shown in Figure 6.1(b).

Figure 6.2 shows the system overview using offline corrections, where a post-processing stage is necessary. First, the offline drift ϵ_{o} resulting from all associations made during the walk is generated as the output of the first stage as shown in Figure 6.2(a). In the post-processing stage, ϵ_{o} is used by the orientation estimation filter to generate a drift-reduced yaw angle that yields to a drift compensated trajectory (Figure 6.2(b)).

Indeed, the proposed offline drift error correction assumes that the drift value is constant during the walk and this assumption does not hold for long periods. If this algorithm is applied for long periods, the computed offline drift ϵ_{o} will offer an average of the drift accumulated during the complete trajectory. The online drift correction pocket navigation system is valid for slow changing drift values, which is a realistic assumption.

The position estimation filter consists of an unscented Kalman filter, whose state vector $\boldsymbol{x}_{\mathrm{p}}$ is composed of the 3D position of the pedestrian:

$$\boldsymbol{x}_{\mathrm{p}}{}^{j} = [x^j, y^j, z^j]. \tag{6.1}$$

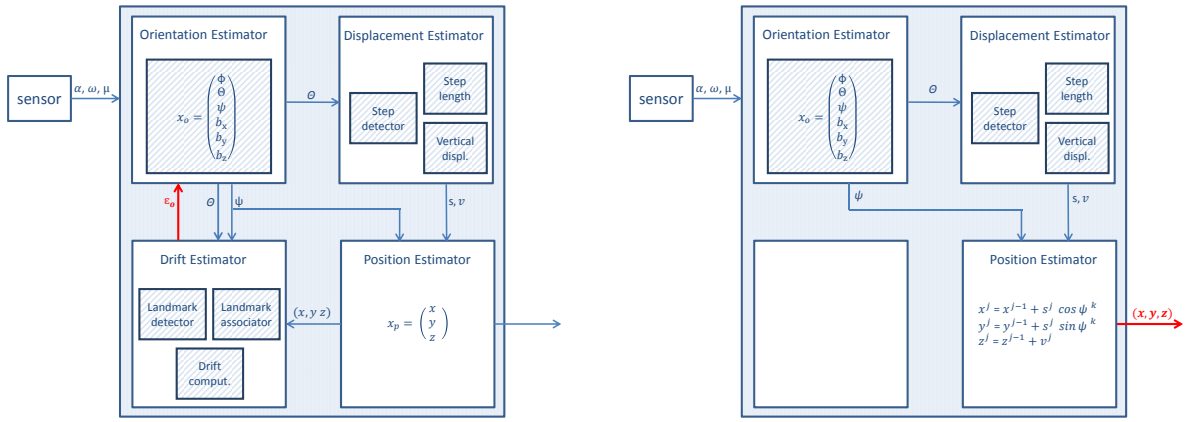

(a) (b)

Figure 6.2: Proposed enhanced inertial pocket navigation system by including the landmark-based drift compensation algorithms in two steps: (a) first the offline drift value ϵ_o is computed and (b) second this value is used by the orientation estimator to generate a drift compensated trajectory.

In the prediction stage, the pitch angle θ is used for the displacement estimator in order to estimate the step length s and the vertical displacement v stepwise. Finally, the 3D position (x, y, z) is calculated with the step length, the vertical displacement and the yaw angle estimation as follows:

$$
\begin{aligned}
x^j &= x^{j-1} + s^j \cdot \cos(\psi^k), \\
y^j &= y^{j-1} + s^j \cdot \sin(\psi^k), \\
z^j &= z^{j-1} + v^j.
\end{aligned}
$$

The position estimation filter outputs a new 3D position (x, y, z) every time the pedestrian performs a step. The update stage is activated by the landmark associator. If no landmarks are detected or no associations are made, the position estimation filter is only based on the prediction stage. The lack of corrections leads to an ever increasing uncertainty of the pedestrian position, thus the enhanced inertial navigation system becomes the 3D basic navigation system. A successful association of two landmarks yields to several corrections, as explained in the following. Apart from the correction of the position, the computed drift ϵ and the yaw angle ψ_{L} , which are fed back to the orientation estimation filter, will limit the yaw angle estimation error. In order to track slow drift changes it is beneficial to have several associations during the walk.

6.1 Online Corrections

As previously mentioned, the online corrections are feeding the orientation, with yaw angle and drift updates, and the position estimator, with position updates. Corrections are performed every time two landmarks are associated.

6.1.1 Yaw Angle and Drift Corrections

The estimated current yaw angle $\hat{\psi}^k$ can be corrected after an association using the detected yaw angle of the landmark ψ_L. The yaw angle stored in the data base ψ_1 has less uncertainty than the current yaw estimation $\hat{\psi}^k = \psi_2$, because it was computed at a previous time instant. The correction ψ_L is not in all cases directly equal to the yaw angle ψ_1 stored in the data base. It is necessary to take into account the direction in which the landmark has been described during the re-visit, e.g. it can be 180° shifted if the landmark is re-visited in the opposite direction. Additionally, if the landmark is a corner, two yaw angles ψ_1 are stored in the data base, i.e. $\overline{\psi}_B$ and $\overline{\psi}_A$.

The drift value ϵ computed as a result of the association will also act as pseudo-measurement to correct the estimation of the bias of the z-axis gyroscope b_z. Therefore, the pseudo-measurement $\boldsymbol{z}_\mathrm{p}^{\boldsymbol{j}}$ of the Kalman filter at the time j can be written as:

$$\boldsymbol{z}_\mathrm{p}^{\boldsymbol{j}} = [\psi_\mathrm{L}, \epsilon]^T. \tag{6.2}$$

6.1.2 Position Correction

In the case of an association, the position of the landmark stored in the data base, which contains less uncertainty than the current position because it was computed at a previous time, will act as pseudo-measurement. Therefore, $(x_\mathrm{L}, y_\mathrm{L}, z_\mathrm{L}) = (x_1, y_1, z_1)$, being the vector $\boldsymbol{z}_\mathrm{p}^{\boldsymbol{j}}$ of the Kalman filter at the time j:

$$\boldsymbol{z}_\mathrm{p}^{\boldsymbol{j}} = [x_\mathrm{L}, y_\mathrm{L}, z_\mathrm{L}]^T. \tag{6.3}$$

6.2 Offline Correction

Online position corrections lead to discontinuities in the trajectory which might not be desired depending on the use case of the navigation system. If a corrected and smoothed trajectory is required, an offline drift correction is a suitable solution. The offline correction implies computing the trajectory once without performing any corrections in order to compute the averaged drift value ϵ_o. Afterwards, in a post-processing stage the trajectory is again computed, but assuming a value of the bias of the z-axis gyroscope b_z equal to ϵ_o.

Therefore, the offline processing configuration counts with the following initial gyroscope biases set:

$$\begin{aligned} b_\mathrm{x} &= 0, \\ b_\mathrm{y} &= 0, \\ b_\mathrm{z} &= \epsilon_\mathrm{o}. \end{aligned} \tag{6.4}$$

The offline drift value ϵ_{o} is computed taken into account the drift values resulting from all associations during the walk, but rejecting possible outliers. The decision whether the drift value is an outlier or not is based on the expected drift values given the sensor characteristics and the cohesion of all obtained values. The value ϵ_{o} is computed weighting the total number of associations η with the elapsed time between landmarks Δt.

$$\epsilon_{\mathrm{o}} = \frac{1}{\sum_{l=1}^{\eta} \Delta t_l} \cdot \sum_{u=1}^{\eta} \Delta t_u \cdot \epsilon_u. \tag{6.5}$$

The drift computation algorithm is more robust to errors on the detected yaw angle for each landmark if the elapsed time between associated landmarks is larger, therefore associations with larger elapsed time between landmarks are more reliable.

During the offline processing, no assumptions regarding b_{x} and b_{y} are used. These biases will be estimated, as well as during the online processing, making use of the gravity field. However, during the offline processing, there is a prior knowledge of b_{z}. Therefore, its initial uncertainty is reduced. The effect of different initial uncertainties for b_{z} during the offline processing is analyzed and discussed in the experiments.

6.3 Experimental Results

The position estimation filter is evaluated in this section for both types of configurations: online and offline corrections.

The evaluation of the online corrections is performed first with the already presented 2D walk recorded at the Theresienhöhe in Munich. A known drift value will be added to the FOG turn rate quasi-error-free measurements to have a controlled drift evaluation analysis. Last, a 2D walk performed at the Deutsches Museum using the medium-cost MEMS MTw will be presented in order to provide the prove that the online drift estimation algorithm is valid for real MEMS inertial sensors and the assumption of slow changing drift holds.

The evaluation of the offline correction will be presented with a 3D walk recorded at the Deutsches Museum of the city of Munich. This walk has been recorded with the medium-cost MEMS MTw sensor and it includes corners and stairs.

6.3.1 Online Correction

First, the drift estimation algorithm will be tested with known drift using quasi-error-free turn rate measurements and then the algorithm will be evaluated with unknown drift using medium-cost MEMS gyroscopes.

6.3.1.1 Evaluation with Quasi-Error-Free Measurements

The 2D walk recorded at the Theresienhöhe in Munich, whose trajectory is shown in Figure 6.3, has been computed using the IMU DSP-1750 measurements. Therefore, the orientation estimation is considered quasi-error-free, as demonstrated in previous chapters.

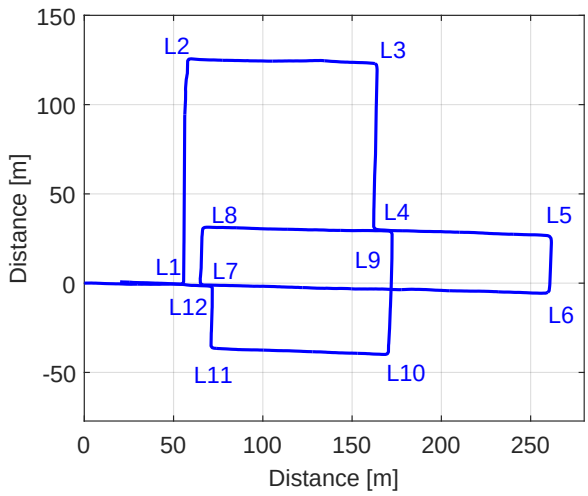

Figure 6.3: Trajectory corresponding to the walk recorded at the Theresienhöhe with the IMU DSP-1750. The detected corners are labeled.

To obtain the trajectory, the algorithms proposed in this thesis have been used for the step detection and step length estimation. Note that the length estimation of the path may contain errors. For instance, the computed distance between L6 and L7 is shorter than the real distance (see Figure 6.3): this difference might be due to errors in the step length, or due to several non-detected steps. Errors on the estimated length of the trajectory caused by non-detected or over-detected steps are expected to be automatically corrected via position corrections. Position corrections can also be used to modify the parameters a_{H} and b_{H} of the proposed step length model assuming that all steps were correctly detected:

$$s = a_{\mathrm{H}} \cdot \Delta\theta_{\mathrm{H}} + b_{\mathrm{H}},$$

where s is the estimated step length as a function of the estimated pitch amplitude in horizontal surfaces $\Delta\theta_{\mathrm{H}}$ and a_{H} and b_{H} are parameters fitting the regression line of each pedestrian. The adjustment of the parameters of this equation based on position corrections is, however, not implemented in this thesis.

In order to emulate MEMS gyroscope measurements $\boldsymbol{\omega}$, white noise $\boldsymbol{v}$ and biases $\boldsymbol{b}$, whose values are summarized in Table 6.1, are added to the FOG quasi-error-free turn rate measurements $\tilde{\boldsymbol{\omega}}$ as follows:

$$\boldsymbol{\omega} = \tilde{\boldsymbol{\omega}} + \boldsymbol{v} + \boldsymbol{b}.$$

Table 6.1: Values of Noise and Biases

	$\boldsymbol{v}$ [° s^{-1}]	$\boldsymbol{b}$ [° s^{-1}]
x-axis		-0.1
y-axis	0.1	0.1
z-axis		0.05

The blue curve of Figure 6.4(a) represents the yaw angle that has been computed integrating the quasi-error-free turn rate measurements without subtracting the biases estimation or applying corrections. The green and orange curves of Figure 6.4 are computed with the emulated MEMS-quality turn rate measurements.

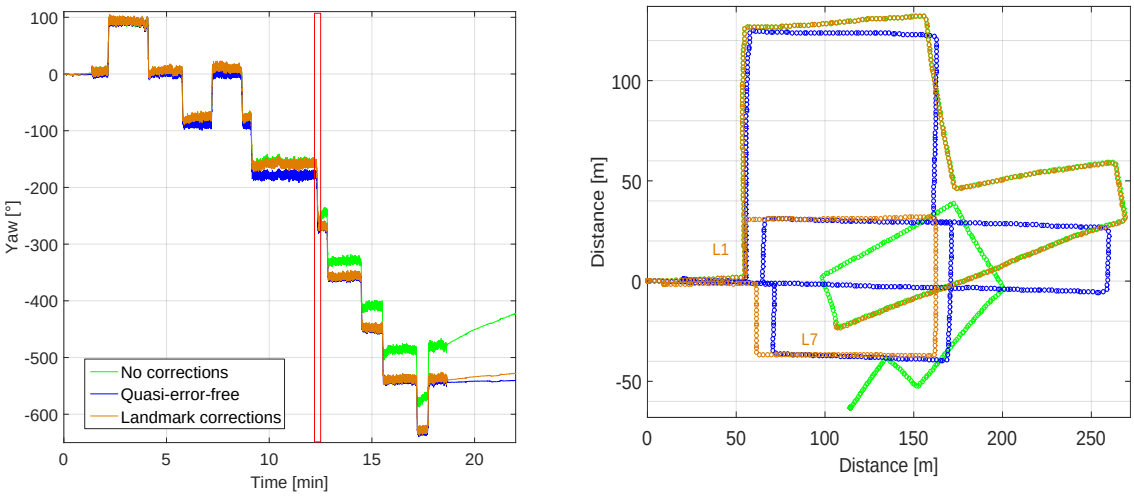

(a) (b)

Figure 6.4: Curves corresponding to the 2D walk recorded at the Theresienhöhe. (a) shows in blue the yaw angle resulting from the quasi-error-free turn rate measurements and in green and orange the emulated MEMS-quality turn rate measurements. The orange curve is corrected by the association (L7, L1) at the time indicated with the red rectangle. (b) shows the trajectories whose colors correspond to the cases shown in (a). The orange curve shows a discontinuity caused by the position correction.

The orange curve includes, however, one correction derived from the association of landmarks (L7, L1), while the green curve has been obtained without applying any correction derived from landmark associations. As Figure 6.4(a) shows, the association (L7, L1) has a strong effect on the yaw angle being effective from the time instant when the association takes place, indicated with a red rectangle. Until the association instant, the green and the orange curves overlap; the accumulated errors evolve over time compared to the quasi-error-free blue curve. When the association occurs, the current yaw angle ψ_{L} is corrected as well as the bias of the z-axis gyroscope using the value ϵ, that prevents the yaw angle from drifting from this point on.

This can be seen in Figure 6.4(a) since the orange curve approximates to the quasi-error-free blue curve and the green curve keeps on drifting. The orange curve, however, does not completely overlap the quasi-error-free blue curve, having residual errors. Note

that the yaw angle used by the correction slightly differs from the quasi-error-free value, since it has been extracted from the landmark data base and already contains an accumulated error. After the association (L7, L1), the data base is cleared and the next landmark, L8, is written into the data base. No further associations are detected after that time instant.

Figure 6.4(b) shows the computed trajectories corresponding to the cases aforementioned and represented with the same color code. The green and orange curves overlap until the time instant of the association (L7, L1). After this point, the green curve keeps drifting as before and the orange curve has a discontinuity caused by the correction, bringing L7 close to the position of L1, which is $(x_{\mathrm{L}}, y_{\mathrm{L}}, z_{\mathrm{L}})$. It is also noticeable, that the length error accumulated from L6 to L7 is automatically corrected, as the orange curve shows. The length correction and the fact that the yaw angle does not completely match the reference one, cause that the orange and blue curves of the trajectories do not perfectly overlap after the position correction derived from the association.

Figure 6.5(a) shows the biases estimation without applying corrections and Figure 6.5(b) shows the biases estimation including the corrections derived from the association (L7, L1). These two cases are visualized by the green and orange curves of Figure 6.4, respectively. Both subfigures show how the *Absolute Gravity Update* favours a reduction of the uncertainty on the x- and y-axes since the beginning bringing the estimation to the right value, as indicated in Table 6.1.

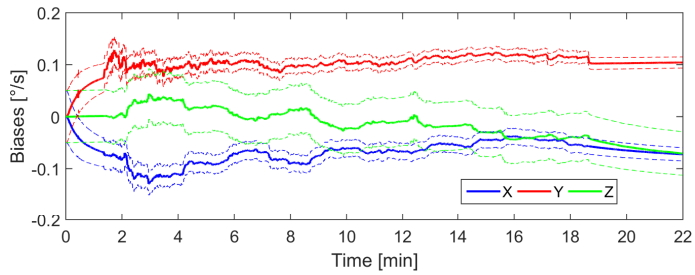

(a)

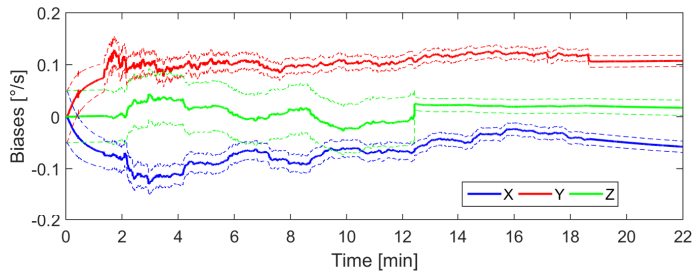

(b)

Figure 6.5: (a) shows the biases estimation of the green curves of Figure 6.4 without applying corrections. The blue curves correspond to the x-axis bias, the red curves to the y-axis bias and the green curves to the z-axis bias estimation. The dotted lines represent their estimated uncertainty. (b) shows the biases estimation including the corrections derived from the association (L7, L1) that takes place between the minute 12 and 13.

The z-bias estimation, however, does not count with any source of information to be correctly estimated, since the *Differential Magnetic Field Update* is not being applied in order to isolate and analyze the effect of the corrections derived from landmark associations. Figure 6.5(a) shows the z-bias estimation without applying landmark corrections, which remains around 0° and tends to a negative value after 14 min. The bias of the z-axis gyroscope is, therefore, influenced by the x- and y-axis biases and not being correctly estimated.

If an erroneous z-bias estimation is used, an additional error will be introduced to the turn rate of the z-axis gyroscope, that leads to spoiled yaw angle estimations. On the one hand, one suitable solution consists on removing the z-bias as a state from the orientation estimation filter, since it does not count with any source of information to be correctly estimated. On the other hand, the bias of the z-axis gyroscope is of interest as a state of the orientation filter if the *Differential Magnetic Field Update* is able to guarantee a successful estimation providing regular corrections.

Figure 6.5(b) shows the z-bias estimation applying the corrections derived from the association of (L7, L1), which takes place between the minutes 12 and 13. After the correction, the uncertainty of the z-bias estimation is clearly reduced and its mean tends to a positive value close to $0.05\,^{\circ}\,\mathrm{s}^{-1}$.

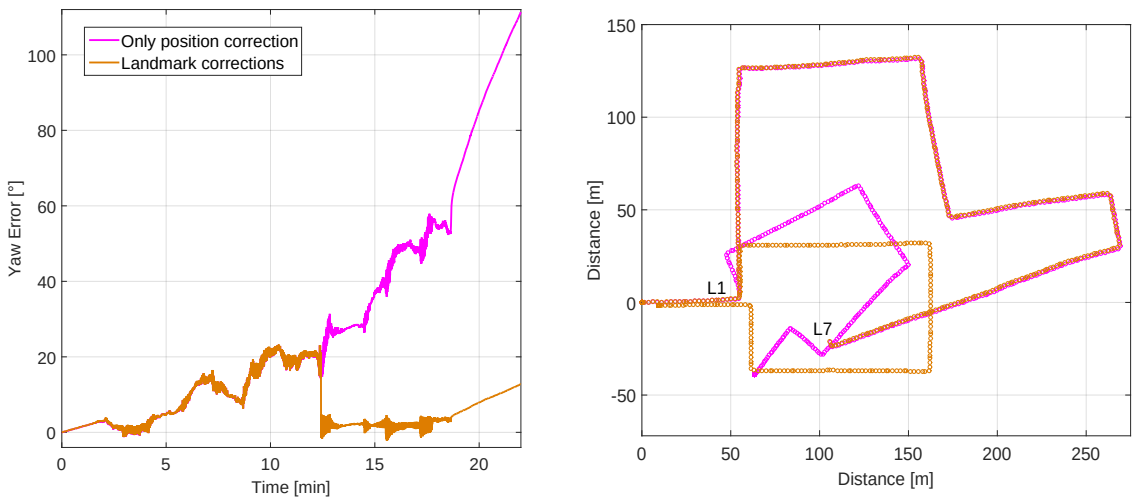

(a) (b)

Figure 6.6: (a) shows in magenta the result of applying only the position correction when the landmarks are associated and the orange curve represents the error on the yaw angle estimation by feeding back the corrections also to the orientation estimation filter. (b) shows the effect of the different types of corrections on the trajectory with the same color code.

Figure 6.6(a) illustrates how the error in the yaw angle estimation is drastically reduced after the corrections derived from the association. The magenta curve has been computed by only correcting the position after the association (L7, L1). Applying only position corrections is the well-known approach in the literature and it does not prevent the yaw angle error to grow. The orange curve has been computed applying the proposed online

corrections, i.e. position and orientation. Figure 6.6(b) illustrates the improvement of the trajectory derived from the proposed online corrections derived from the association (L7, L1). The benefit of the proposed online drift estimation is demonstrated.

6.3.1.2 Evaluation with Medium-Cost MEMS Measurements

For this evaluation the medium-cost MEMS MTw introduced in the front pocket of the trousers has been used. The 2D walk recorded at the Deutsches Museum in Munich is shown in Figure 6.7. The recorded walk has a duration of 8 min and has been performed covering an area of approximately 4200 m^2. The blue curve shows the drift compensated trajectory. The yellow dot indicates the initial and final point.

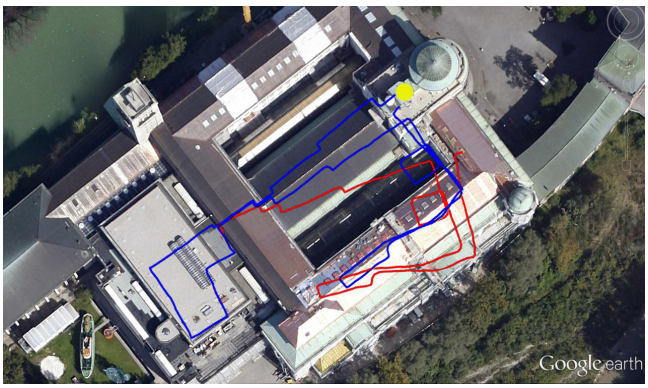

Figure 6.7: Raw (red) and drift compensated trajectory (blue) recorded at the Deutsches Museum in Munich. Initial an end point (yellow) are the same.

Unlike the evaluation driven in the previous section, the bias values are not known, therefore also the drift error is unknown. It will be considered that the drift value found by the proposed algorithm is correct if the ending part of the walk overlaps the initial zone of the walk, marked in yellow in Figure 6.7.

Figure 6.8 shows the estimated trajectory of the aforementioned walk without compensating the drift error. The blue markers represent the steps taken by the pedestrian, while the red ellipses represent the uncertainty in the position of the time when landmarks are detected. As shown in the figure, the uncertainty only grows with time if no corrections are performed. The steps highlighted in red correspond to the position where the landmarks, i.e. the corners, are detected. The improved landmark detector is tested with this walk and, as shown in Figure 6.8, all corners of the walk are correctly detected. The corner located at (40, 50) is detected as a single turn of 180°.

The information of the detected landmarks is stored in the data base. For the online drift estimation algorithm, the data base is emptied after each association. The data base generated until the first association (L8, L15) is summarized in Table 6.2. The data base shows entries of relevant landmarks. The *Position* is the 2D position of the landmarks in navigation frame (x, y) and the *Yaw* angle includes the value before and after turning

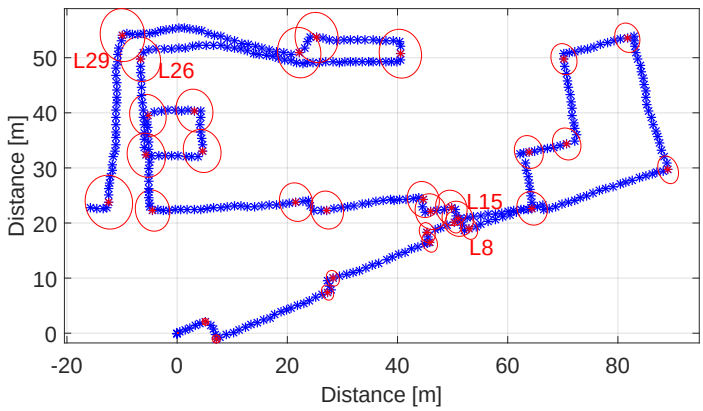

Figure 6.8: Estimated trajectory of the walk at the Deutsches Museum. The red ellipses represent the uncertainty in the position of the detected corners and the red markers highlight its position. Associated landmarks are labeled.

the corner, $\overline{\psi}_B$ and $\overline{\psi}_A$. Note that the uncertainty grows with time, as also denoted with the red ellipses in Figure 6.8.

Table 6.2: Data Base Generated until the Association (L8, L15)

	Type	Time [s]	Position [m]	Uncertainty [m^2]	Yaw [°]
L1	1	17.3	(5.12, 2.06)	$\begin{pmatrix} 0.05 & -0.08 \\ -0.08 & 0.062 \end{pmatrix}$	(25.3, -80.9)
...	...	...	...	...	...
L8	1	215.2	(52.65, 19.27)	$\begin{pmatrix} 0.21 & -0.003 \\ -0.003 & 0.22 \end{pmatrix}$	(199.5, 136.8)
...	...	...	...	...	...
L14	1	225.9	(64.42, 22.65)	$\begin{pmatrix} 1.27 & -0.015 \\ -0.015 & 1.54 \end{pmatrix}$	(294.1, 200.3)

After the association (L8, L15) takes place, the computed drift value $\epsilon_1 = -0.052\,^\circ\,\mathrm{s}^{-1}$. The derived corrections, i.e. position, drift and yaw angle, are applied at this time. Figure 6.9 shows highlighted in cyan the resulting position where the first association occurs. As shown in Figure 6.9, the trajectory estimated has been partially corrected in comparison with the trajectory shown in Figure 6.8.

As a result of the online corrections, the uncertainty in the position decreases, as shown in Figure 6.9. The uncertainty of yaw and the bias of the z-axis gyroscope also decreases. Then, the data base is emptied and the next association detected corresponds to (L26, L29). The computed drift value is $\epsilon_2 = -0.014\,^\circ\,\mathrm{s}^{-1}$. This value corresponds to the slow drift fluctuation accumulated from L15 on. As shown in the figure, the ending part of the walk overlaps with the initial zone of the walk, thus the drift has been successfully online compensated. Following this procedure, further associations allow the presented algorithm to adapt to slow drift changes. Therefore, the proposed online algorithm is suited for long duration walks.

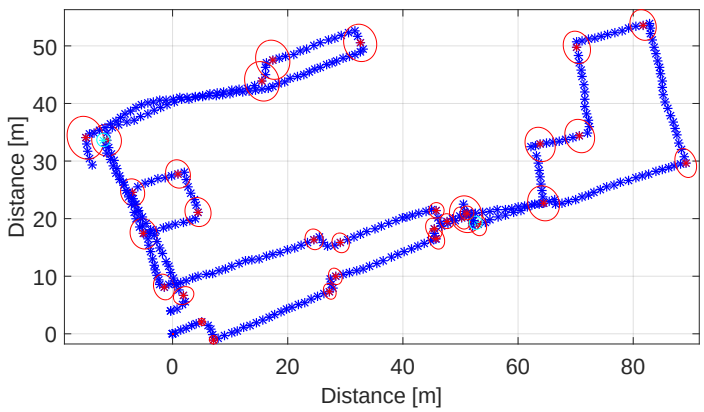

Figure 6.9: Estimated trajectory when the proposed online drift compensation algorithm is used. The red ellipses represent the uncertainty of the detected corners. Associations are marked in cyan.

6.3.2 Offline Correction

This section aims at testing the offline drift correction with unknown biases and drift error. The 3D walk recorded at the Deutsches Museum of the city of Munich, whose trajectory is shown in Figure 6.10, has been computed using measurements provided by the medium-cost MEMS MTw inertial sensors.

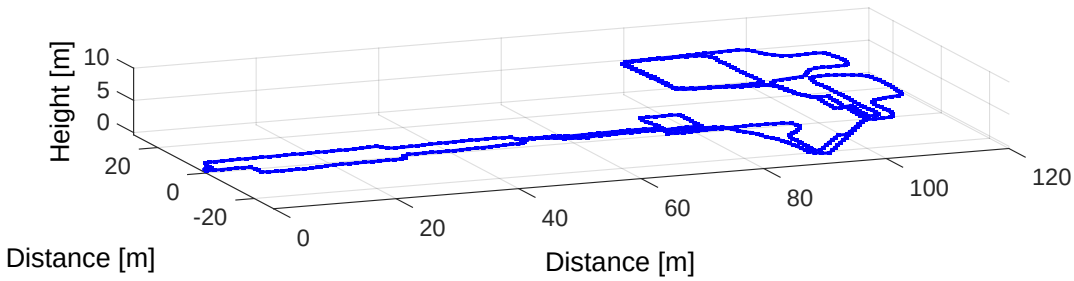

Figure 6.10: 3D view of the trajectory estimated of a 10 min walk at the Deutsches Museum, Munich.

The orientation and the horizontal and vertical displacement estimation have been computed using the algorithms proposed in this thesis. The drift value, $-0.065\,^{\circ}\,\mathrm{s}^{-1}$, has been manually computed and compensated during an offline processing. The walk, which lasts 10 min, starts at (0,0,0) and follows the dark blue curve. The ending point coincides with the initial point.

The Deutsches Museum scenario presents a highly perturbed magnetic field, since the visitor walks between metallic pieces of the exhibited ships and airplanes. In such a scenario, successful z-bias estimation based on the *Differential Magnetic Field Update* needs longer than the duration of the walk, in this case 10 min. For this reason, it is imperative to find alternative methods to compensate the accumulated drift over time, such as the proposed approach based on landmarks. It has been decided to dismiss magnetic measurements and only use acceleration and turn rate measurements for the 3D trajectory estimation in order to isolate the effect of the offline correction derived from

the landmarks.

(a)

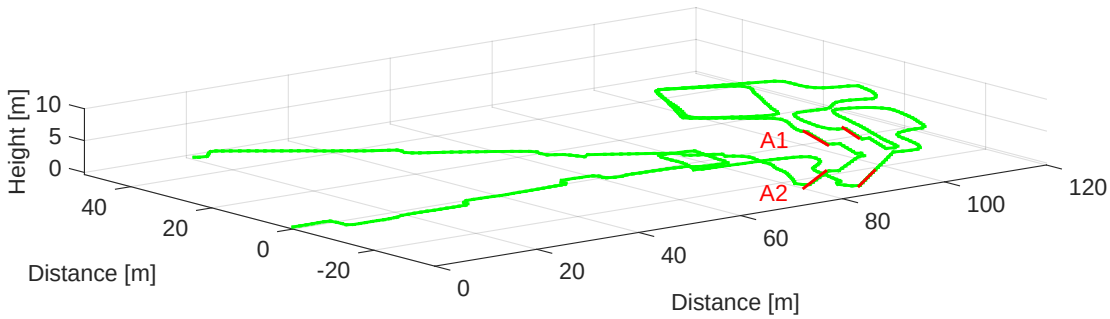

(b)

Figure 6.11: 2D and 3D view of the walk recorded at the Deutsches Museum without compensating the drift. The landmark associations automatically selected by the algorithm proposed in this thesis are highlighted in the figure: (a) includes in red the corner situated on the ground floor and (b) includes in red the associations of the staircase.

Figure 6.11 shows the 2D and 3D view of the walk computed without compensating the drift by only using inertial measurements. The effect of the drift is clearly visible, gradually twisting the trajectory in a way that the initial and ending points are almost 54 m away. The associations made automatically by the algorithm designed in this thesis have been marked in the figure as A1, A2 and A3. The stairs connecting the first floor and the second floor, A1, and the stairs connecting the ground floor and the first floor, A2, highlighted in red in Figure 6.11(b) have been successfully associated, even though the stairs are in some cases detected in two sections due to the landing zone. Last, one corner on the ground floor at the beginning of the stairs, A3, highlighted in red in Figure 6.11(a) has also been associated. The loops described on the third floor lead to two possible corner associations, however, these are automatically discarded because the time between landmarks is not significant enough to accumulate drift. Table 6.3 summarizes the deviation angles δ, the time between associated landmarks Δt and the drift ϵ_i values automatically computed resulting from the three associations aforementioned.

In this case, all possible drift values ϵ_i for $i = \{1, 2, 3\}$ are coherent with the sensor

Table 6.3: Associations of the Walk Shown in Figure 6.11

	δ [°]	Δt [s]	ϵ [° s^{-1}]
A1	-17	186.1	**-0.091**
A2	-18.3	295.1	**-0.062**
A3	-19.1	307.6	**-0.062**

characteristics, therefore all of them are taken into account for the computation of ϵ_o. The offline drift value automatically computed for this walk based on Equation (6.5) is $-0.068\,^\circ\,\mathrm{s}^{-1}$, which is very similar to the manually computed drift value $-0.065\,^\circ\,\mathrm{s}^{-1}$.

Figure 6.12 shows the resulting trajectories in 2D if ϵ_o is used by the orientation estimator during the post-processing. In both cases the initial bias b_z has been set to the drift value ϵ_o equal to $-0.065\,^\circ\,\mathrm{s}^{-1}$. Figure 6.12(a) illustrates the effect of setting the initial uncertainty equal for the biases of all axes of the gyroscope. Figure 6.12(b) shows the trajectory by reducing the initial uncertainty of b_z taken into account the previous knowledge of ϵ_o. Additionally, it is recommendable for longer walks to apply magnetic corrections during the post-processing stage to track slow variations on the drift.

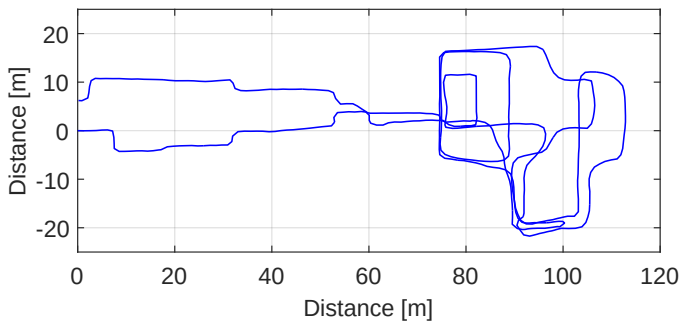

(a)

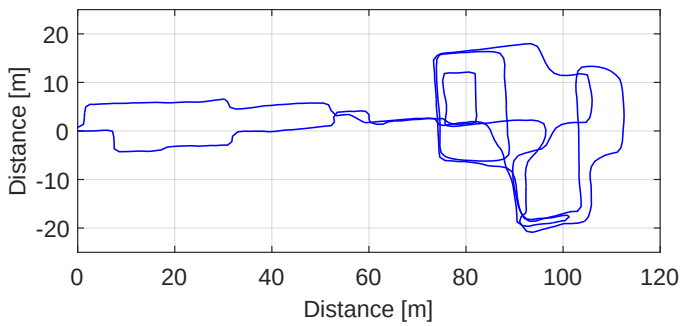

(b)

Figure 6.12: Trajectories computed during the post-processing stage using ϵ_o. (a) has been computed by setting the initial uncertainty of the bias b_z equal for all axes and (b) has been computed by reducing the initial uncertainty of b_z.

Using Equation (6.5) the value ϵ_o is computed being the result equal to $-0.068\,^\circ\,\mathrm{s}^{-1}$, which is very similar to the correct drift value $-0.065\,^\circ\,\mathrm{s}^{-1}$. Figure 6.13 shows the resulting trajectory in 3D if the drift error is compensated using the value of $-0.068\,^\circ\,\mathrm{s}^{-1}$

computed by the offline drift estimator algorithm. It is, therefore, proved that the underlying drift error accumulated over a determined trajectory can be automatically computed and successfully compensated in a post-processing stage if a constant drift error during the whole trajectory is assumed.

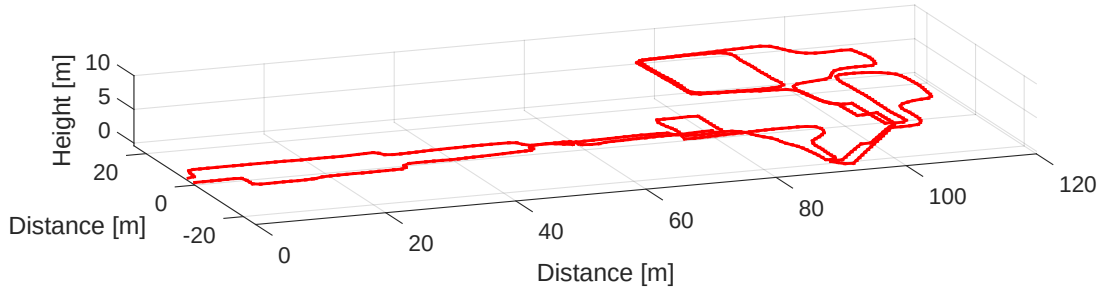

Figure 6.13: 3D trajectory drift compensated with ϵ_o equals to $-0.068\,^\circ\,\mathrm{s}^{-1}$.

6.4 Discussion

This chapter has shown the position estimation filter, which estimates the position of the pedestrian stepwise. If no landmarks are detected or no associations are done, the uncertainty of the position grows with time. The great majority of the state of the art algorithms perform only corrections of the pedestrian position based on SLAM or based on the information of additional sensors. The novelty of the algorithms proposed in this thesis is the drift estimation, that prevents the yaw angle error to ever grow, as assessed in this chapter.

Corrections derived from landmark associations can be applied online or offline, depending on the use case of the navigation system. If the variable of interest is the current pedestrian position, all corrections should be applied online. These corrections will introduce a discontinuity on the trajectory estimation, however, the current position has a reduced error and the yaw angle error will be limited for a longer period of time. If a corrected trajectory without discontinuities is desired, the derived drift value can be applied during a post-processing stage. During this stage, magnetic updates can also be applied to track slow drift variation if the duration of the walk is large enough for the drift value to present changes.

This thesis has proved for the first time that it is possible to provide 3D positioning through the step-and-heading approach using solely inertial measurements for a non-shoe-mounted sensor. Additionally, the effectiveness of the proposed drift estimation algorithm under given conditions, i.e. re-visiting the landmarks, to provide an improved trajectory without using additional sensors has been demonstrated.

Chapter 7

Conclusions and Outlook

Every new beginning comes from
some other beginning's end.

Seneca

This thesis presents the algorithms derived from the research carried out on the field of pedestrian inertial navigation. Particularly for indoor and urban scenarios, and assuming that the sensor is located on the upper part of the leg of the pedestrian, e.g. in the front pocket of the trousers.

On the one hand, state of the art algorithms for non-shoe-mounted pedestrian navigation systems show poor accuracy in the horizontal displacement, and the vertical displacement is unsolved without using additional sensors. Thus, algorithms are presented in this thesis that improve the accuracy of the horizontal displacement estimation, and a novel algorithm able to deliver the vertical displacement of the pedestrian is proposed. This thesis demonstrates for the first time that, thanks to the proposed algorithms, it is possible to deliver 3D positioning through the step-and-heading approach using only inertial measurements for a non-shoe-mounted sensor.

On the other hand, the heading angle rapidly accumulates an error mainly caused by systematic errors of the gyroscope. Therefore, a comprehensive analysis of the effect of different magnetic field distributions on the estimation of the errors of MEMS gyroscopes has been carried out. This thesis demonstrates that, although magnetic field measurements are beneficial to reduce these errors, the estimation process might require long time. In order to avoid that a large error is accumulated on the heading angle during this time, this thesis presents a drift estimation algorithm based on the seamless detection of landmarks during the walk.

7.1 Conclusions

The algorithms proposed in this thesis perform the estimation of the following variables: orientation, displacement, drift error and position. Their performance has been analyzed with experiments using reference and medium-cost sensors and compared to the state of the art algorithms. One chapter is dedicated to each variable and the conclusions of each chapter are summarized in the following.

The proposed orientation estimation algorithm estimates sequentially the orientation of the sensor as well as the bias of the gyroscopes. Due to the fact that the roll and pitch angles are observable through the gravity field, their estimation presents a limited error. However, changes in the yaw angle cannot be observed because the yaw angle describes rotations around the axis parallel to the gravity field. Therefore, in this thesis an evaluation of the usability of the magnetic field to estimate the bias of the z-axis of MEMS gyroscopes is presented. The results show that it is possible to correctly estimate the bias of the x- and y-axes gyroscopes, however, the bias of the z-axis gyroscope remains unobservable. Different locations on the Earth, i.e. North Pole, Equator and Munich are evaluated in order to analyze the influence of the magnetic field distribution on the estimation process of the biases. The North Pole magnetic field distribution does not allow observing rotations around the z-axis. However, thanks to the movement of the leg of the pedestrian while walking, it is possible to correctly estimate the bias of the z-axis gyroscope. The magnetic field distribution influences the time needed to estimate the z-bias. The estimation of the biases under magnetically perturbed fields is also evaluated. It has been demonstrated that it is possible to estimate the bias of the z-axis gyroscope in the presence of perturbations. However, it is convenient to use only measurements that belong to constant or quasi-constant magnetic field periods for the estimation, avoiding the highly perturbed field. The effect of using uncalibrated magnetic field measurements is also analyzed. Additionally, measurements recorded by medium-cost MEMS sensors are evaluated yielding to the conclusion that magnetic measurements help estimating the bias of the gyroscopes, however, due to the non-homogeneous nature of the magnetic field in indoor and urban scenarios, the estimation process is prohibitively slow. Last, the analysis is completed by studying the effect of the estimation of the bias of the z-axis gyroscope on the yaw angle. The results show that successful estimations of the bias of the z-axis gyroscope reduce significantly the error on the yaw angle.

The proposed displacement estimator is composed of three algorithms, i.e. step detector, step length estimator and vertical displacement estimator. These algorithms are fed with the pitch angle estimation provided by the orientation estimator. For the step detector, challenging scenarios have been analyzed, such as different walking speeds and 3D walks. The well-known state of the art algorithms have been implemented and tested under the same conditions in order to have a fair comparison. The results of the experiments let conclude that the proposed step detector based on the maximum of the pitch

angle outperforms the state of the art step detectors in terms of undetected and false detected steps. The proposed step length estimator makes use of the relationship between the amplitude of the pitch angle estimation and the step length. The performance of the presented algorithm is compared with the step length estimator of the state of the art, which is based on the relationship between step frequency and step length. The experiments carried out under challenging scenarios let conclude that the proposed step length estimator offers accurate results within a larger range of walking speeds, whilst the state of the art estimator based on the step frequency only offers optimal results for a predetermined walking speed. The novel vertical displacement algorithm investigated in this thesis, which is also based on the amplitude of the pitch angle estimation, is tested in a multi-storey scenarios. The vertical displacement algorithm enhances the state of the art as it offers a 3D inertial positioning solution for the first time for inertial navigation systems based on the step-and-heading approach. It is also possible to use the pitch angle estimation to identify five physical activities, i.e. walking, standing, sitting, walking upstairs and walking downstairs. The physical activity identification based on the pitch angle adds a great value to the state of the art, because of its simplicity and effectiveness.

The novelty of the proposed drift estimation algorithm lies on computing the drift error value based on seamlessly detected landmarks. The drift is accumulated on the yaw angle over time causing an increasing error in the estimated trajectory. The poor observability of the yaw angle and the bias of the z-axis gyroscope causes that this error is ever growing. Therefore, in this thesis an algorithm is presented to compute the drift error. The proposed algorithm, which makes only use of inertial measurements, assumes that the drift has a slowly varying nature, which is a realistic assumption. The drift estimator consists of the landmark detection, landmark association and drift computation algorithms. It has been demonstrated in this thesis that the chosen landmarks, i.e. stairs and corners, can be seamlessly detected and associated and are appropriate for the targeted scenarios. The detection, however, presents challenges because the wavy shape of the yaw angle estimation might introduce an error that is propagated to the estimated drift value. Thus, only associations whose time between detected landmarks is large enough are considered reliable. If the association occurs when the uncertainty of the position of the detected landmarks is large, multiple hypotheses might be possible. Therefore, it is of crucial importance to correct the yaw angle error in an early stage in order not to accumulate a high error in the position estimation. Small drift corrections that are needed due to the slowly varying nature of the drift are continuously performed during the walk through further associations.

The position estimator provides the position of the pedestrian stepwise. If an association occurs, the position is corrected as well as the yaw angle and the bias of the z-axis gyroscope of the orientation estimator. The proposed algorithm enhances the state of the art, since the major part of the already proposed algorithms perform only corrections on the estimated position, which does not correct the error on the yaw angle. It has

been proved that the proposed corrections prevent the yaw angle error to rapidly grow. Therefore, further positioning errors are prevented. Corrections derived from landmark associations can be applied online or offline, depending on the use case of the inertial pedestrian navigation system. If the current pedestrian position is of interest, corrections should be applied every time two landmarks are associated. These corrections will introduce a discontinuity on the trajectory estimation, however, the current position has a reduced error and the yaw angle error will be corrected. If a smoothed trajectory is desired, the averaged drift value derived through all associations made during the walk is computed and applied offline, i.e. during a post-processing stage. During the post-processing, magnetic and gravity corrections are also performed. If the duration of the walk is large enough for the accumulated drift to present slow changes, these variations are considered and compensated over time during the post-processing. The effectiveness of the presented drift estimation algorithm under given conditions, i.e. re-visiting landmarks, to provide an improved trajectory without using additional sensors is demonstrated in this thesis.

7.2 Publications Derived from the Thesis

The following publications have been derived from this thesis:

1. Munoz Diaz, E. and Heirich, O. and Khider, M. and Robertson, P., "Optimal Sampling Frequency and Bias Error Modeling for Foot-Mounted IMUs", *IEEE International Conference on Indoor Positioning and Indoor Navigation (IPIN)*, 2013.

2. Munoz Diaz, E. and Mendiguchia Gonzalez, A.L. and de Ponte Müller, F., "Standalone Inertial Pocket Navigation System", *IEEE/ION Position Location and Navigation Symposium (PLANS)*, 2014.

3. Munoz Diaz, E., "Estimation of the Vertical Displacement of Leg-Based Moving Bodies Through the Opening Angle of the Leg" (patent acceptation pending). Filed July 2014.

4. Munoz Diaz, E. and Mendiguchia Gonzalez, A.L., "Step Detector and Step Length Estimator for an Inertial Pocket Navigation System", *IEEE International Conference on Indoor Positioning and Indoor Navigation (IPIN)*, 2014.

5. Munoz Diaz, E. and Jimenez, A. and de Ponte Müller, F. and Zampella, F., "Evaluation of AHRS Algorithms for Inertial Personal Localization in Industrial Environments", *IEEE International Conference on Industrial Technology*, 2015.

6. Munoz Diaz, E. and Gutiérrez-Rivas, R. and de García Domínguez, J.J., "Indoor Navigation Applied to the Detection of Allergic Reactions During Provocation Tests", *IEEE International Conference on Indoor Positioning and Indoor Navigation (IPIN)*, 2015.

7. Munoz Diaz, E., "Inertial Pocket Navigation System: Unaided 3D Positioning", *Sensors*, vol. 15, pp. 9156–9178, 2015.

8. Munoz Diaz, E. and de Ponte Müller, F. and García Domínguez, J.J., "Use of the Magnetic Field for Improving Gyroscopes' Biases Estimation", *Sensors*, vol. 17, pp. 832, 2017.

9. Munoz Diaz, E. and Caamano, M., "Landmark-Based Online Drift Compensation Algorithm for Inertial Pedestrian Navigation", *IEEE International Conference on Indoor Positioning and Indoor Navigation (IPIN)*, 2017.

10. Munoz Diaz, E. and Caamano, M. and Fuentes Sánchez, F.J., "Landmark-Based Drift Compensation Algorithm for Inertial Pedestrian Navigation", *Sensors*, vol. 17, pp. 1555, 2017.

7.3 Outlook

Future investigation lines derived from this thesis are identified in the following:

Due to the price reduction and miniaturization of MEMS inertial sensors, nowadays they are embedded in many personal belongings, such as smart phones, smart watches and smart glasses. It is, therefore, meaningful to use as many sensors as possible for pedestrian positioning purposes. Since several sensors are mounted at different locations on the pedestrian, i.e. pocket, wrist, foot, head... the fusion of all measurements will provide an enhanced trajectory with reduced drift. The fusion algorithm weights the different measurements taking into account their quality depending on the sensor location and the physical activity performed by the pedestrian.

By counting on several sensor locations, an auto-calibration of the displacement estimation parameters for the pocket navigation system is possible. The calibration is based on the fact that all sensors are mounted on the same pedestrian, therefore, the horizontal and vertical displacement should be the same for all of them.

The PDR strapdown approach used for shoe-mounted inertial sensors delivers 3D position estimations. The error accumulated on the height estimation is one of the largest

errors together with the heading error. The research carried out in this thesis regarding the pitch angle estimation can be also used to deduce the movement of the foot, which is different by walking on horizontal surfaces and walking on ramps or stairs. Therefore, the knowledge of the scenario allows applying corrections that reduce the height error for PDR strapdown algorithms for shoe-mounted inertial navigation systems.

Bibliography

[1] N. Bowditch (Originally by), *The American Practical Navigator*. National Imagery and Mapping Agency. U.S. Government Printing Office, 2002 Bicentennial Edition.

[2] A. Szalai, *The Use of Time: Daily Activities of Urban and Suburban Populations in Twelve Countries*. Mouton, 1972.

[3] R. Gutierrez-Rivas, J. J. García, and L. Marnane, "Use of the Heart Rate Variability as a Diagnostic Tool," *8th International Joint Conference on Biomedical Engineering and Technologies*, pp. 25–35, 2015.

[4] E. Munoz Diaz, R. Gutiérrez-Rivas, and J. J. de García Domínguez, "Indoor Navigation Applied to the Detection of Allergic Reactions During Provocation Tests," *IEEE International Conference on Indoor Positioning and Indoor Navigation (IPIN)*, 2015.

[5] R. Harle, "A Survey of Indoor Inertial Positioning Systems for Pedestrians," *IEEE Communications Surveys and Tutorials*, vol. 15, no. 3, pp. 1281–1293, 2013.

[6] S. Madgwick, "An Efficient Orientation Filter for Inertial and Inertial/Magnetic Sensor Arrays," *Report x-io and University of Bristol*, 2010.

[7] R. Mahony, T. Hamel, and J.-M. Pflimlin, "Nonlinear Complementary Filters on the Special Orthogonal Group," *IEEE Transactions on Automatic Control*, pp. 1203–1217, May 2008.

[8] E. Munoz Diaz, A. Jimenez, F. de Ponte Müller, and F. Zampella, "Evaluation of AHRS Algorithms for Inertial Personal Localization in Industrial Environments," *IEEE International Conference on Industrial Technology*, 2015.

[9] F. Zampella, M. Khider, P. Robertson, and A. Jimenez, "Unscented Kalman Filter and Magnetic Angular Rate Update (MARU) for an Improved Pedestrian Dead-Reckoning," *IEEE/ION Position Location and Navigation Symposium (PLANS)*, 2012.

[10] Z.-Q. Zhang, X.-L. Meng, and J.-K. Wu, "Quaternion-Based Kalman Filter With Vector Sesection for Accurate Orientation Tracking," *Instrumentation and Measurement, IEEE Transactions on*, vol. 61, no. 10, pp. 2817–2824, October 2012.

[11] M. H. Azfal, V. Renaudin, and G. Lachapelle, "Use of Earth's Magnetic Field for Mitigating Gyroscope Errors Regardless of Magnetic Perturbation," *Sensors*, pp. 11 390–11 414, 2011.

[12] J. Li, F. Jiancheng, and M. Du, "Errror Analysis and Gyro-Bias Calibration of Analytic Coarse Alignment for Airbone POS," *Instrumentation and Measurement, IEEE Transactions on*, vol. 61, no. 11, pp. 3058–3064, November 2012.

[13] Z.-Q. Zhang and G.-Z. Yang, "Calibration of Miniature Inertial and Magnetic Sensor Units for Robust Attitude Estimation," *Instrumentation and Measurement, IEEE Transactions on*, vol. 63, no. 3, pp. 711–718, March 2014.

[14] B. Gozick, K. Subbu, R. Dantu, and T. Maeshiro, "Magnetic Maps for Indoor Navigation," *IEEE Transactions on Instrumentations and Measurements*, vol. 60, no. 12, pp. 3883–3891, December 2011.

[15] J. B. Bancroft and G. Lachapelle, "Use of Magnetic Quasi Static Field (QSF) Updates for Pedestrian Navigation," *IEEE/ION Position Location and Navigation Symposium (PLANS)*, 2012.

[16] E. Munoz Diaz, F. de Ponte Müller, and J. García Domínguez, "Use of the magnetic field for improving gyroscopes' biases estimation," *Sensors*, vol. 17, p. 832, 2017.

[17] P. Goyal, V. J. Ribeiro, H. Saran, and A. Kumar, "Strap-Down Pedestrian Dead-Reckoning System," *IEEE International Conference on Indoor Positioning and Indoor Navigation (IPIN)*, pp. 1–7, 2011.

[18] U. Steinhoff and B. Schiele, "Dead Reckoning from the Pocket-An Experimental Study," *IEEE International Conference on Pervasive Computing and Communications (PerCom)*, pp. 162–170, 2010.

[19] Y. Jin, H.-S. Toh, W.-S. Soh, and W.-C. Wong, "A Robust Dead-Reckoning Pedestrian Tracking System with Low Cost Sensors," *IEEE International Conference on Pervasive Computing and Communications (PerCom)*, pp. 222–230, 2011.

[20] S. Shin, M. Lee, C. Park, and H. S. Hong, "Pedestrian Dead Reckoning System with Phone Location Awareness Algorithm," *IEEE/ION Position Location and Navigation Symposium (PLANS)*, pp. 97–101, 2010.

[21] D. Gusenbauer, C. Isert, and J. Krosche, "Self-Contained Indoor Positioning on Off-the-Shelf Mobile Devices," *IEEE International Conference on Indoor Positioning and Indoor Navigation (IPIN)*, pp. 1–9, 2010.

[22] M. Alzantot and M. Youssef, "UPTIME: Ubiquitous Pedestrian Tracking Using Mobile Phones," *IEEE International Wireless Communications and Networking Conference (WCNC)*, pp. 3204–3209, 2012.

[23] R. Jirawimut, P. Ptasiski, V. Garaj, F. Cecelja, and W. Balachandran, "A Method for Dead Reckoning Parameter Correction in Pedestrian Navigation System," *IEEE Transactions on Instrumentation and Measurement*, vol. 52, no. 1, 2003.

[24] Z. Xiao, H. Wen, A. Markham, and N. Trigoni, "Robust Pedestrian Dead Reckoning (R-PDR) for Arbitrary Mobile Device Placement," *IEEE International Conference on Indoor Positioning and Indoor Navigation (IPIN)*, 2014.

[25] C.-C. Lo, C.-P. Chiu, Y.-C. Tseng, S.-A. Chang, and L.-C. Kuo, "A Walking Velocity Update Technique for Pedestrian Dead-Reckoning Applications," *IEEE 22nd International Symposium on Personal Indoor and Mobile Radio Communications (PIMRC)*, pp. 1249–1253, 2011.

[26] E. Munoz Diaz and A. L. Mendiguchia Gonzalez, "Step Detector and Step Length Estimator for an Inertial Pocket Navigation System," *IEEE International Conference on Indoor Positioning and Indoor Navigation (IPIN)*, 2014.

[27] D. Alvarez, R. C. González, A. López, and J. C. Alvarez, "Comparison of step length estimators from weareable accelerometer devices," *IEEE 28th Annual International Conference of Engineering in Medicine and Biology Society (EMBS)*, pp. 5964–5967, 2006.

[28] J. Jahn, U. Batzer, J. Seitz, L. Patino-Studencka, and J. Gutiérrez Boronat, "Comparison and Evaluation of Acceleration Based Step Length Estimators for Handheld Devices," *IEEE International Conference on Indoor Positioning and Indoor Navigation (IPIN)*, pp. 1–6, 2010.

[29] W.-Y. Shih, L.-Y. Chen, and K.-C. Lan, "Estimating Walking Distance with a Smart Phone," *IEEE 5th International Symposium on Parallel Architectures, Algorithms and Programming (PAAP)*, pp. 166–171, 2012.

[30] H. Weinberg, "Using the ADXL202 in Pedometer and Personal Navigation Applications," *Application Notes, American Devices*, 2002.

[31] V. Renaudin, V. Demeule, and M. Ortiz, "Adaptative Pedestrian Displacement Estimation with a Smartphone," *IEEE International Conference on Indoor Positioning and Indoor Navigation (IPIN)*, vol. 12, pp. 916–924, 2013.

[32] S. Shin, C. Park, J. Kim, H. Hong, and J. Lee, "Adaptive Step Length Estimation Algorithm Using Low-Cost MEMS Inertial Sensors," *IEEE Sensors Applications Symposium (SAS)*, pp. 1–5, 2007.

[33] V. Renaudin, M. Susi, and G. Lachapelle, "Step Length Estimation Using Handheld Inertial Sensors," *Sensors*, vol. 12, no. 7, pp. 8507–8525, 2012.

[34] E. Munoz Diaz, "Inertial Pocket Navigation System: Unaided 3D Positioning," *Sensors*, vol. 15, pp. 9156–9178, 2015.

[35] J. Li, Q. Wang, X. Liu, and M. Zhang, "An Autonomous Waist-Mounted Pedestrian Dead Reckoning System by Coupling Low-Cost MEMS Inertial Sensors and FPG Receiver for 3D Urban Navigation," *Journal of Engineering Science and Technology.*, 2014.

[36] D. Titterton and J. Weston, *Strapdown Inertial Navigation Technology.* American Instutute of Aeronautics and Astronautics., 2004.

[37] E. Munoz Diaz, M. Caamano, and F. Fuentes Sanchez, "Landmark-Based Drift Compensation Algorithm for Inertial Pedestrian Navigation," *Sensors*, vol. 17, p. 1555, 2017.

[38] E. Munoz Diaz and M. Caamano, "Landmark-Based Online Drift Compensation Algorithm for Inertial Pedestrian Navigation," *IEEE International Conference on Indoor Positioning and Indoor Navigation (IPIN)*, 2017.

[39] J. Borenstein and L. Ojeda, "Heuristic Drift Elimination for Personnel Tracking Systems," *The Royal Institute of Navigation*, vol. 63, pp. 591–606, 2010.

[40] K. Abdulrahim, C. Hide, T. Moore, and C. Hill, "Aiding MEMS IMU with Building Heading for Indoor Pedestrian Navigation," *Ubiquitous Positioning Indoor Navigation and Location Based Service (UPINLBS)*, 2010.

[41] ——, "Using Constraints for Shoe Mounted Indoor Pedestrian Navigation," *The Royal Institute of Navigation*, vol. 65, pp. 15–28, 2012.

[42] A. R. Jimenez, F. Seco, F. Zampella, and J. C. Prieto, "Improved Heuristic Drift Elimination (iHDE) for Pedestrian Navigation in Complex Buildings," *IEEE International Conference on Indoor Positioning and Indoor Navigation (IPIN)*, pp. 1–8, 2011.

[43] A. R. Jimenez, F. Seco, J. C. Prieto, and J. Guevara, "Indoor Pedestrian Navigation Using an INS/EKF Framework for Yaw Drift Reduction and a Foot-Mounted IMU," *7th Workshop on Positioning Navigation and Communication (WPNC)*, pp. 135–143, 2010.

[44] A. R. Jimenez, F. Seco, F. Zampella, J. C. Prieto, and J. Guevara, "Improved Heuristic Drift Elimination with Magnteically-Aided Dominant Directions (MiHDE) for Pedestrian Navigation in Complex Buildings," *Journal of Location Based Services*, vol. 6, pp. 186–210, 2012.

[45] P. Aggarwal, D. Thomas, J. Borenstein, and L. Ojeda, "Map Matching and Heuristic Elimination of Gyro Drift for Personal Navigaton Systems in GPS-Denied Conditions," *Journal of Measurement Science and Technology*, vol. 22, 2011.

[46] J. Pinchin, C. Hide, and T. Moore, "A Particle Filter Approach to Indoor Navigation Using a Foot-Mounted Inertial Navigation System and Heuristic Heading Information," *IEEE International Conference on Indoor Positioning and Indoor Navigation (IPIN)*, pp. 1–10, 2012.

[47] A. Millonig and K. Schechtner, "Developing Landrmak-Based Pedestrian-Navigation Systems," *IEEE Transactions on Intelligent Transportation Systems*, vol. 8, no. 1, 2007.

[48] D. Griesbach, D. Baumbach, and S. Zuev, "Stereo-Vision-Aided Inertial Navigation for Unknown Indoor and Outdoor Environments," *IEEE International Conference on Indoor Positioning and Indoor Navigation (IPIN)*, pp. 709–716, 2014.

[49] A. Jimenez R., F. Seco, F. Zampella, J. C. Prieto, and J. Guevara, "PDR with a Foot-Mounted IMU and Ramp Detection," *Sensors*, vol. 11, pp. 9393–9410, 2011.

[50] P. Robertson, M. Angermann, and B. Krach, "Simultaneous Localization and Mapping for Pedestrians using only Foot-Mounted Inertial Sensors," *International Conference on Ubiquitous Computing*, pp. 93–96, 2009.

[51] M. Garcia Puyol, D. Bobkov, P. Robertson, and T. Jost, "Pedestrian Simultaneous Localization and Mapping in Multistory Bildings Using Inertial Sensors," *IEEE Transactions on Intelligent Transportation Systems*, vol. 15, pp. 1714–1727, 2014.

[52] P. Robertson, M. Frassl, M. Angermann, M. Doniec, B. J. Julian, M. Garcia Puyol, M. Khider, M. Lichtenstern, and L. Bruno, "Simultaneous Localization and Mapping for Pedestrians Using Distortions of the Local magnetic Field Intensity in Large Indoor Environments," *IEEE International Conference on Indoor Positioning and Indoor Navigation (IPIN)*, pp. 1–10, 2013.

[53] M. Hardegger, D. Roggen, S. Mazilu, and G. Troster, "ActionSLAM: Using location-related Actions as Landmarks in Pedestrian SLAM," *IEEE International Conference on Indoor Positioning and Indoor Navigation (IPIN)*, 2012.

[54] R. Kalman, "A New Approach to Linear Filtering and Prediction Problems," *Research Institute for Advanced Study, Baltimore Md.*, 1960.

[55] J. Wagner and T. Wieneke, "Integrating Satellite and Inertial Navigation - Conventional and New Fusion Approaches," *Control Engineering Practice*, vol. 11, no. 5, pp. 543–550, August 2003.

[56] "IEEE Standard Specification Format Guide and Test Procedure for Single-Axis Interferometric Fiber Optic Gyros," *IEEE Std 952-1997*, 1998.

[57] S. Kay, *Fundamentals of Statistical Signal Processing: Estimation Theory*, ser. Prentice Hall Signal Processing Series. Prentice Hall, 1993, no. Bd. 1.

[58] E. Munoz Diaz, A. L. Mendiguchia Gonzalez, and F. de Ponte Müller, "Standalone Inertial Pocket Navigation System," *IEEE/ION Position Location and Navigation Symposium (PLANS)*, 2014.

[59] B. Huyghe, P. Salvo, J. Doutreloigne, and J. Vanfleteren, "Feasibility Study and Performance Analysis of a Gyroless Orientation Tracker," *Instrumentation and Measurement, IEEE Transactions on*, vol. 61, no. 8, pp. 2274–2282, August 2012.

[60] X. Yun, E. R. Bachmann, and R. B. McGhee, "A Simplified Quaternion-Based Algorithm for Orientation Estimation from Earth Gravity and Magnetic Field Measurements," *Instrumentation and Measurement, IEEE Transactions on*, vol. 57, no. 3, pp. 638–650, March 2008.

[61] V. Renaudin and C. Combettes, " Magnetic, Acceleration Fields and Gyroscope Quaternion (MAGYQ)-Based Attitude Estimation with Smartphone Sensors for Indoor Pedestrian Navigation," *Sensors*, pp. 22 864–22 890, 2014.

[62] P. Groves, *Principles of GNSS, Inertial, and Multisensor Integrated Navigation Systems, Second Edition:* , ser. GNSS/GPS. Artech House, 2013.

[63] "IEEE Standard Specification Format Guide and Test Procedure for Single-Axis Interferometric Fiber Optic Gyros," *IEEE Std 952-1997*, pp. 1–84, 1998.

[64] E. Munoz Diaz, O. Heirich, M. Khider, and P. Robertson, "Optimal Sampling Frequency and Bias Error Modeling for Foot-Mounted IMUs," *IEEE International Conference on Indoor Positioning and Indoor Navigation (IPIN)*, 2013.

[65] "Munich Earth Observatory. Monthly Magnetograms." *http://www.geophysik.uni-muenchen.de/observatory/geomagnetism*, 2015.

[66] J. D. Jackson, *Classical Electrodynamics, 3rd ed.* John Wiley and Sons, New York, 1999.

[67] V. Renaudin, M. H. Afzal, and G. Lachapelle, "Complete Triaxis Magnetometer Calibration in the Magnetic Domain," *Journal of Sensors. Hindawi Publishing Corporations*, 2010.

[68] A. D. Kuo, "A Simple Model of Bipedal Walking Predicts the Preferred Speed-Step Length Relationship," *Journal of Biomechanical Engineering*, vol. 123, pp. 264–269, 2001.

[69] "Visual Interpretation of the International Residential Code," *Stairway Manufacters. Stair Building Code, EEUU*, 2006.

[70] P. Mahalanobis, "On the Generalized Distance in Statistics," *Proceedings of the National Institute of Sciences of India*, vol. 2, pp. 49–55, 1936.

[71] G. Gallego, C. Cuevas, R. Mohedano, and N. García, "On the Mahalanobis Distance Classification Criterion for Multidimensional Normal Distributions," *IEEE Transactions on Signal Processing*, vol. 61, pp. 4387–4396, 2013.

[72] O. J. Woodman, "An Introduction to Inertial Navigation," *Technical Report. Number 696. University of Cambridge*, 2007.